POLITECNICO

MILANO 1863

SCUOLA DI INGEGNERIA INDUSTRIALE
E DELL'INFORMAZIONE

Failure Analysis on the collapse of a power transmission line by use of FEA

TESI DI LAUREA MAGISTRALE IN
MECHANICAL ENGINEERING
INGEGNERIA MECCANICA

Author: **Giacomo Vettoretto**

Student ID: 10741888 - 944308
Advisor: Stefano Beretta
Co-advisors: Christian Affolter, Zongchen Li
Academic Year: 2020-21

Abstract

On October 29, 2018, one among the towers part of the high-voltage power transmission line in *Albula Pass, Switzerland* collapsed due to extreme storm event, causing a cascade sequence on other three elements of the latter.

The study hereby reported discusses about the effective and reliable modeling of both the lattice towers and the line as a whole, with the purpose of estimating the load-bearing capacity, identifying possible failure positions, and replicating the dynamics of the event.

To accomplish that, *Finite Element Analysis (FEA)* has been employed via the software *Abaqus CAE 2021*, and different analysis procedures and modeling strategies have been investigated with the purpose of better simulating structural instabilities both in simple and complex structures.

An imperfection sensitivity on the single tower model has been performed, under reasonable load assumptions and aiming to detect possible unfavorable failure modes and load-bearing capacity.

Ultimately, possible cascade dynamics of the entire line have been proposed and analyzed, and the shortcomings of the proposed approaches have been discussed.

Key-words: Failure Analysis, Lattice Structures, FEA, Structural Instabilities, Joint Modeling.

Abstract in italiano

Il 29 ottobre 2018, uno dei piloni della linea di trasmissione ad alta tensione al *Passo dell'Albula*, in Svizzera, è crollato a causa di un forte temporale, provocando una sequenza a cascata su altri tre elementi di quest'ultima.

Lo studio qui riportato si occupa della modellazione efficace ed affidabile sia dei tralicci che della linea nel suo complesso, al fine di stimare la capacità portante, identificare la posizione di rottura e replicare la dinamica dell'evento.

A tal fine, è stata utilizzata *l'analisi agli elementi finiti (FEA)* tramite il software *Abaqus CAE 2021* e sono state studiate diverse procedure di analisi e strategie di modellazione con l'intento di simulare correttamente le instabilità strutturali sia in strutture semplici che più complesse.

È stata eseguita una sensibilità all'imperfezione sul modello di torre singola, in base a ipotesi di carico ragionevoli e con l'obiettivo di rilevare possibili modalità di rottura sfavorevoli e capacità di carico.

Infine, sono state proposte e analizzate le possibili dinamiche del collasso in sequenza dell'intera linea e sono state discusse le carenze degli approcci proposti.

Parole chiave: Failure Analysis, Strutture reticolari, FEA, Instabilità Strutturale, Modellizzazione di Giunti.

Contents

Introduction

Overhead transmission lines are a vital component in the correct functioning of the electric power grid.

When a failure of even a single tower takes place, the damage can be extensive, involving adjacent towers along the line, and costly, in terms of repair, power disruption, and litigation. (Campbell et. al [1], Hoffmann et al. [2]).

The accurate prediction of service life, based on correct estimation of environmental conditions, is key when designing structures aiming at reliability and safety.

Lattice transmission towers are built with eccentrically connected members, which are usually joined with bolts or welds (S. Fang et al. [3]). During the design phase, stress calculations are obtained via simple linear elastic analysis, in which members are assumed as pinned in place and axially loaded, in the name of more conservativeness, despite full-scale tower testing often show member behavior far from this hypothesis, manifesting effects of bending stresses passing through the joints. The validation of the models through full-scale testing is expensive and not always possible, thus is kept only as a design check.

Nowadays a second-order analysis, accounting for the structure deformation under load in the computing of the forces and displacement (geometrical nonlinearities), is mandated for almost every structure (*Section 7.2, Eurocode 1993-3.1* [4]). The problem is, however complex, and a way to perform such analysis accurately and cost-effectively is to use *Finite Element (FE)* methods. Some software that employ the method, like *Abaqus CAE 2021* [5], can also include the yielding of the cross-section (material nonlinearities) and imperfection modes.

The following study aims to use nonlinear *FE* analysis to understand the possible causes of a collapse event, trying to spot where and why the catastrophic failure has occurred.

Failure case

Event and initial investigations on the site

The 29th of October 2018, four pylons of the overhead power line *"380kV Filisur –
La Punt"* located close to the *Albula pass*, collapsed during the *"Vaia"* storm.

Figure 0.1: Towers from n23 to n26 after the storm in 2018 (source *SwissGrid*).

The four pylons were found laying in a direction close to the perpendicular to the
line (Figure 0.4). The conductor cables were still intact and attached to the insulators
(Figure 0.1, Figure 0.3, Figure 0.4). The earth wire was detached in tower n23 (Figure
0.2a), an insulator was broken in tower n22 (Figure 0.2b), and several wires were
found partially ruptured (Figure 0.2c).
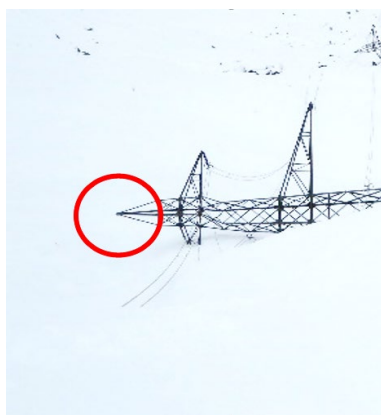
(a) Disconnected earth wire
in tower n23.

(b) Broken insulator in tower
n22.
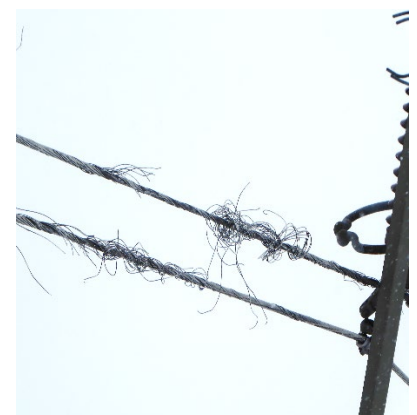
(c)Partially ruptured conductor
wires in tower n24.

Figure 0.2: Details of the collapse (source *SwissGrid*).
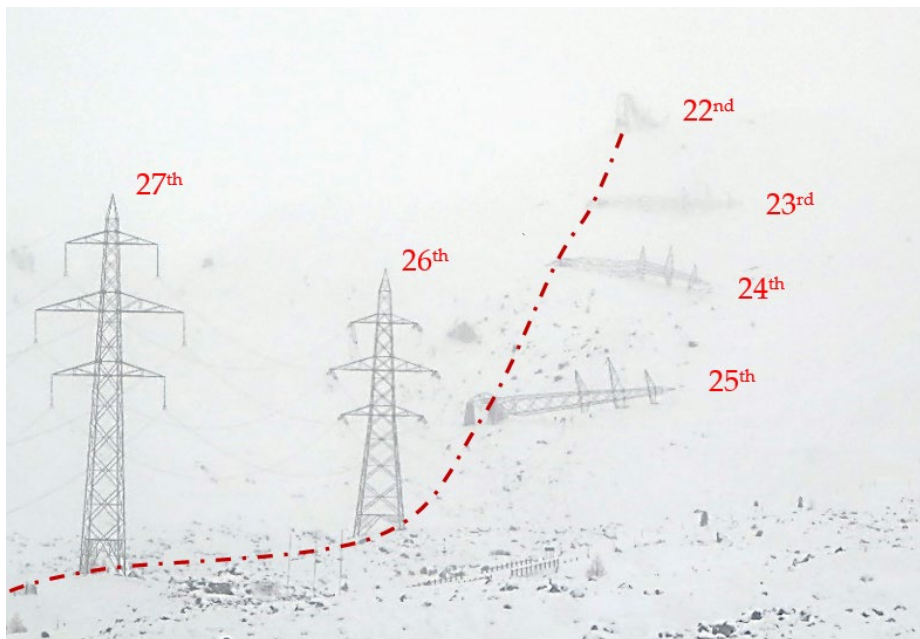
Figure 0.3: Towers from n22 to n27 after the storm in 2018 (source *SwissGrid*). Marked in red, the line path, towers n22 to n25 fallen in perpendicular direction.
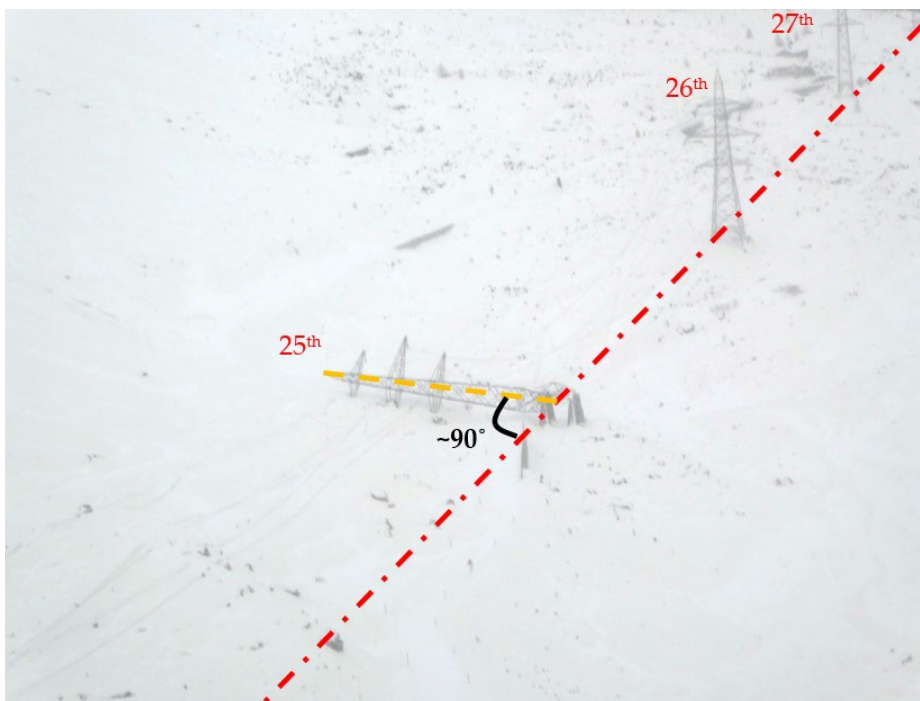
Figure 0.4: Arial view of tower n25 after the storm in 2018 (source *SwissGrid*). Marked in red, the line path, and, highlighted, the angle with the tower axis.

Tower n22 was the only one that failed at midheight, found intact up to the fourth level (Figure 0.5), while the others are found laying on the side, clearly ruptured at the base.
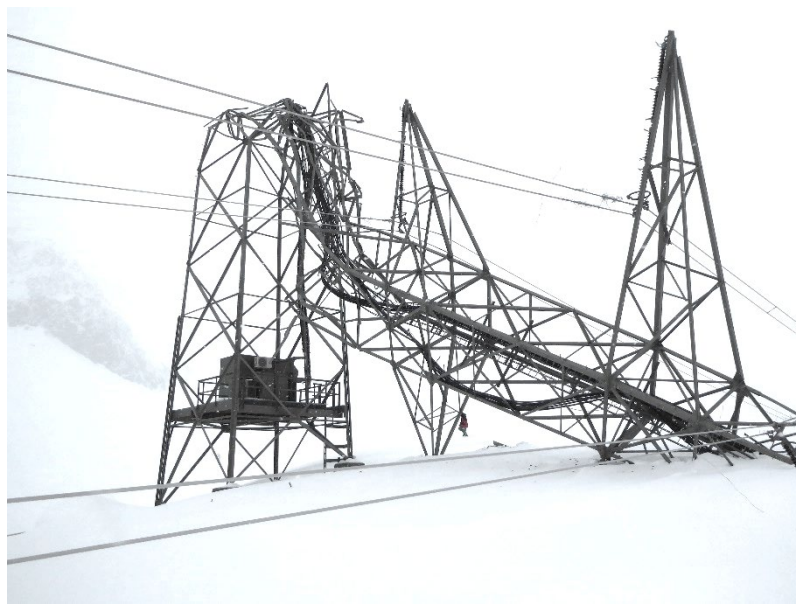
Figure 0.5: Tower n22 after the storm in 2018 (source *SwissGrid*).

Severe but localized damage affected the towers, sign of catastrophic and sudden event restricted to a precise area (Figure 0.6). In such cases, the main difficulty is to differentiate the source and spread of the failure from secondary damage, caused by the contact with the ground.

(a) Tower n22, upper area.

(b) Tower n25, basement.

Figure 0.6: Details of the structural condition (source *SwissGrid*).

Towers n22 and n26 resisted the event (in the backwards, Figure 0.1, Figure 0.3). Tower n26, is a so-called "*Abspannmasten*" (tensioning pylon), a reinforced structure precisely designed for long span line supporting, equipped to withstand and stop the cascade.
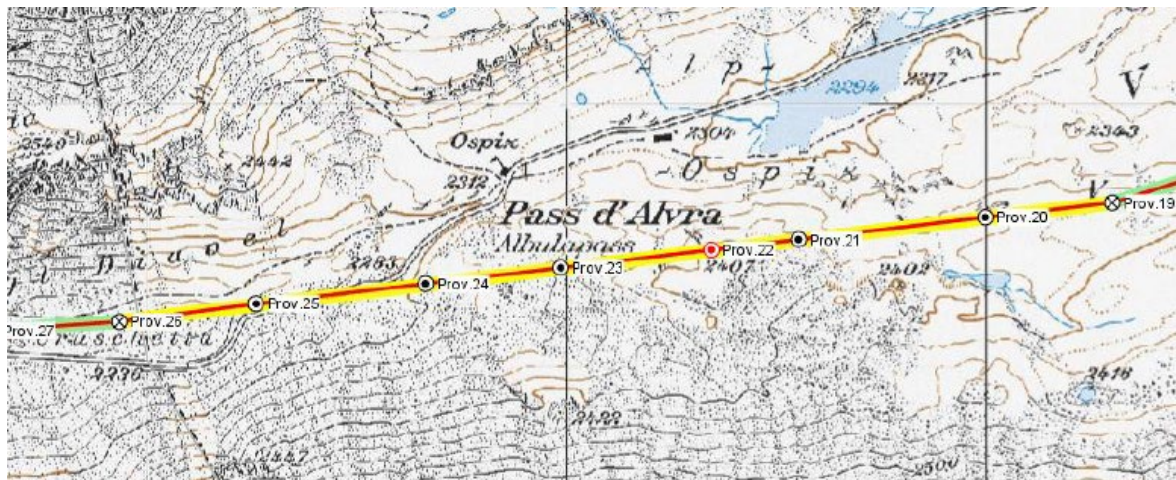
Figure 0.7: Location map of the line segment *"Tragmasten"*, (towers n20 to n25) marked with a dot and "*Abspannmasten*" (towers n26 and n19) with an "x"(source *SwissGrid*).

Historical record in the area

The power transmission line has been in function since the 60s, time at which the towers were designed. *SwissGrid* provided record of the activities since that time.

The area is well known for extreme wind cases, as a similar occurrence happened on April 26, 1986, in the same spot of the line. The resemblance with the event of 2018 is strong, involving the same array of towers and with a shockingly similar failure pattern and direction: tower n25 collapsed at the base, whereas towers n23 and n24 in the upper area (Figure 0.8).

Figure 0.8: Towers n22, n23, n24 and n25 after the event in 1986 (source *SwissGrid*).

Tower n22 at that moment did not have the additional radio equipment installed and it remained intact (Figure 0.8, Figure 0.9).
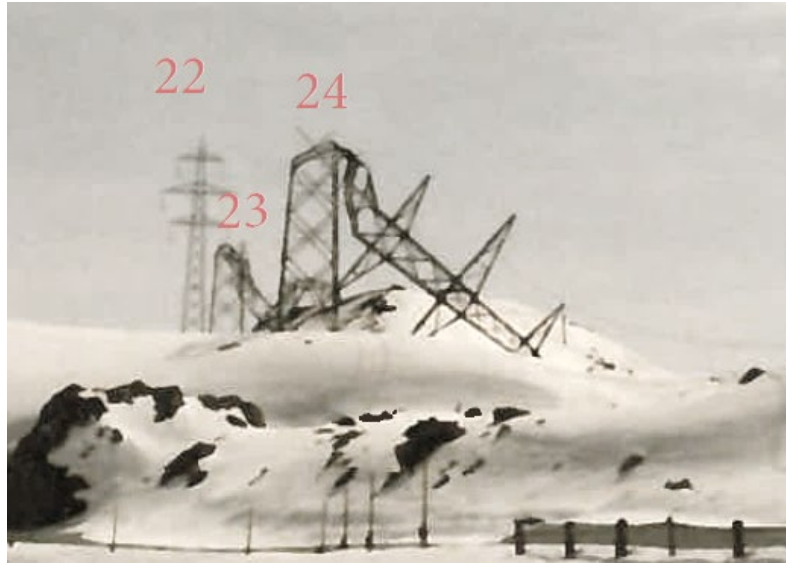
Figure 0.9: Towers n22, n23 and n24 after the event in 1986 (source *SwissGrid*).

The structure condition was, however, unclear at the moment of the collapse, but, according to the available data, it appears that the cause of the collapse was mainly associated with an avalanche tower n25, which caused a cascade effect on n24 and n23.

The concrete basements of the towers were refurbished and the towers rebuilt.

Initial assessments on the 2018 case

There was no ice nor snow on the structures after the event, and the ceramic insulators and wires, features expected to detach under a heavy ice surplus, were still intact. This led to suppose that the sole wind must have been the main cause.

The initial checks on whether the masts were designed in *"state of the art"* in accordance with the current and past standards were performed by a preliminary study by *AF-Consult* [6].

EMPA [7] and *IWT* [8, 9] were initially responsible for the material testing from specimens gathered in the site, as earlier incidents in power conduction lines in Germany were attributed to the negative impact of *"hydrogen embrittlement"* in the structure steel (a check that could be performed by measuring the fracture toughness). Other assessments on the yield and ultimate strength proved that the properties were in fact higher, or in line, with the nominal values for construction steel S355.

For example, the measured yield strength was between 380 and 420 MPa, outclassing the nominal S_y=355 MPa used in the design.
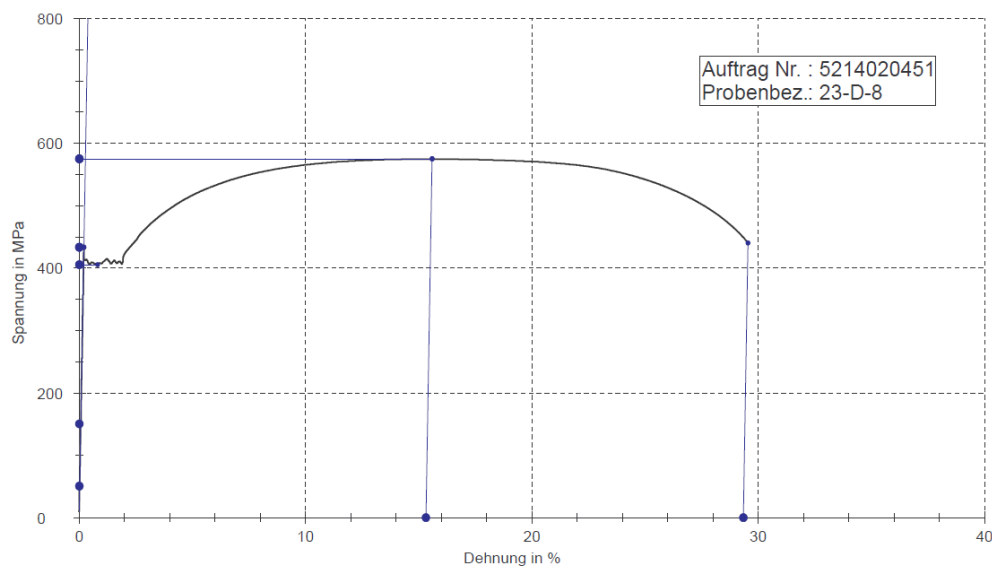
Figure 0.10: Tensile test stress ("*Spannung*") - strain ("*Dehnung* ") curve on a specimen from tower n23's collected components [7].

IED [10] task was to assess the load-carrying capacity of the mast with their *FE* tools. *EMPA* [11] had ultimately to take care of validating the results. The two software used by *IED*, *PLS-Cadd* and *TOWER*, are complementary: the first calculates the towers-cables system static equilibrium based on the applied load case and weather conditions; the latter software inputs the forces at the wire attachment points and the external loads, and performs a linear *FE* analysis of the tower structure. Depending on the chosen design code, it can be also used to assess validity.
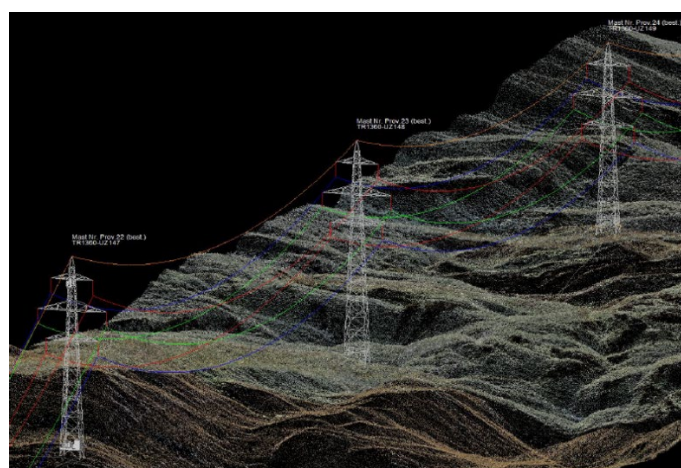
Figure 0.11: *PLS-Cadd* model [10].

The usual approach in these cases is to prove that the masts could actually fail under the conditions present in the incident. However, there was no record of the structure conditions nor the wind pressure, speed or direction at the moment of the collapse.

For this reason, plausible assumptions had to be made by *IED* on the scenario: the wind characteristic had to be estimated from *SIA 261* weather maps [12]. The adopted ground profile was from *SIA 261/1* code [13].
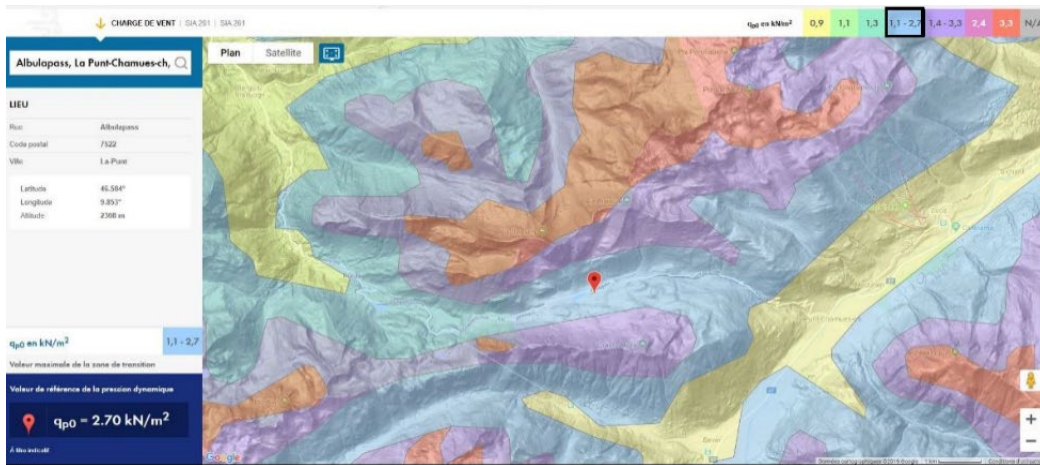
Figure 0.12: *SIA 261* wind pressure map in the *Albulapass* area [10, 12].

It was also examined the possibility of a vertical component to the wind, as the mountainside is inclined of around 30°, as shown in Figure 0.13.

(a) Mountain profile.   (b) Wind inclination.
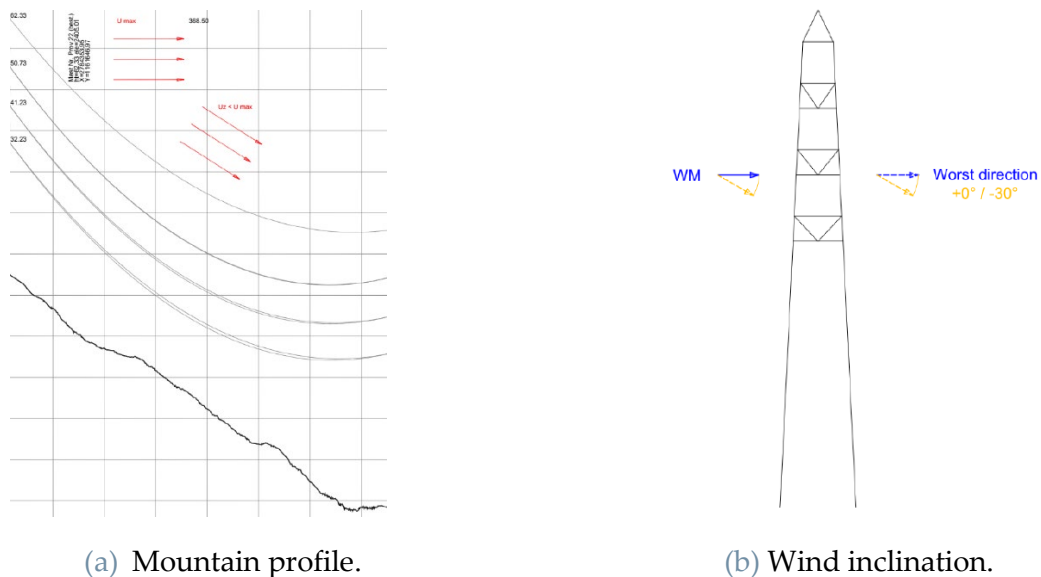
Figure 0.13: Vertical wind component display [10].

The resulting forces at the conductors and the nodal forces in the lattice structure due to wind were represented via polar plots, so-called *"wind rosette"*. Different load cases were applied in *TOWER* changing wind direction, thus obtaining a new rosette for utilization factor of each tower member, compounding the limits from

linear buckling, net section plasticization onset and member end limit states derived from codes and standards (Figure 0.14).
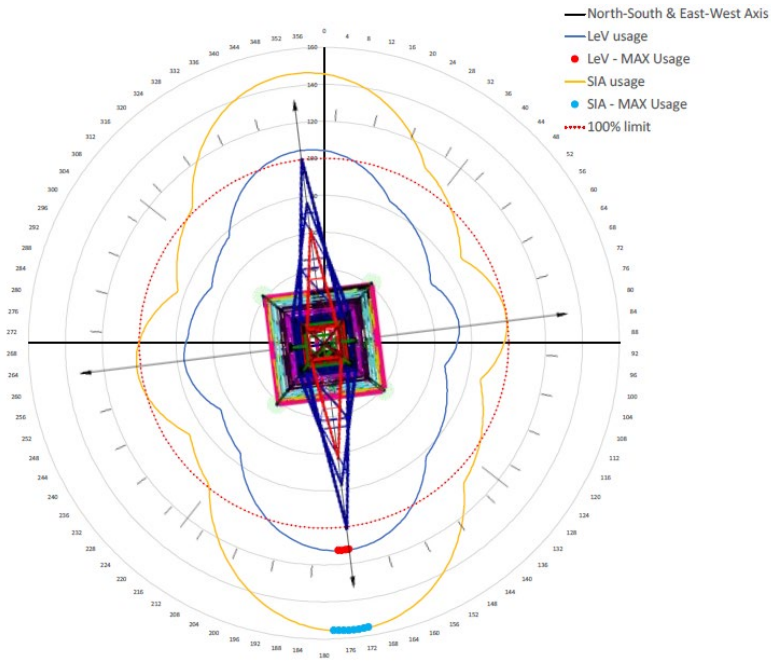
Figure 0.14: "*Wind rosettes*" for wind magnitude [10].

Out of this type of analysis, the obtained critical wind direction was 172° to 180°.

The maximum utilization factor was found in several members of tower n22, some of which close to the area interested in the collapse. Therefore, it was speculated that the line section collapse had initiated from tower n22, and then propagated to the following n23, n24 and n25.
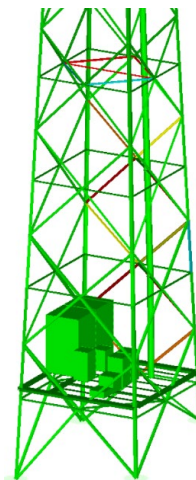
Figure 0.15: "*Utilization factor*" in tower n22, from green (<80%) to red (>100%) in each member [10].

EMPA [11] had validated the results in terms of linear buckling analysis.

Approach to failure analysis

When providing such evidence, the aspect of "conservatism of assumptions" must be taken into account. For a failure analysis case, its meaning can differ quite a lot from what is normally associated with it in the design phase.

	DESIGN PHASE	**FAILURE ANALYSIS**
Loads and actions	High/extreme loads to cover unexpected and unknown interactions and uncertainties.	Plausible/realistic loads that can be reasonably estimated.
Strength and material properties	Low/minimum guaranteed strength, to account for statistical production variability.	Relatively high/true material strength, possibly the highest among the performed tests.

Table 0.1: What means "conservatism" in different analysis types.

In short terms: the design procedure sets as target the survival of a component made of low-end strength material under extreme conditions, whereas a failure analysis aims to prove that even the component with high-end material properties can fail under realistic working conditions.

A small remark on structural instabilities (topic further discussed in Chapter 1): when designing a component, the limit strength is set according to the load that causes the instability to happen, when, the component could actually maintain some residual plastic reserve in the post-instability phase (Figure 1.6) or, in the case of a lattice structure, redundant structural elements.

Limitations of past analysis on the failure topic

Although effective, there are some major limitations to the performed analysis:

- When trying to estimate loads and weather conditions, it is appropriate not to fall into applying too much conservativeness (design-wise speaking).
- *IED* has heavily based their limit load on design standards, giving to elements a *"utilization factor"*. This results in a safe estimation, far from a realistic load-bearing capacity.
- Even though *TOWER* is able to perform geometric nonlinear analysis, it does not account for material plasticity and more complex joint modeling: most of the braces of the lattice structure are regarded as *pinned axially*

connected loaded trusses. No bending moment is transferred across the structure, only forces, and no load eccentricity is present.

- No comparison with the real counterpart was made in order to validate the analysis.
- Only static models were analyzed until maximum load. No collapse simulation, neither of the single tower, nor of the entirety of the line, has been performed. No dynamic loading was considered: possible wind turbulence could cause resonance that might amplify the vibrations.
- Possible model imperfections (geometric from the lattice tower shape, load asymmetry, internal forces on specific members due to uneven assembly or thermal shrinkage) were not investigated.

In short terms: *IED* has employed design tools to analyze a failure case.

The use of finite element methods in failure analysis cases

Many authors have addressed the problem of modeling large and complex structures like power transmission towers.

Past cases offer a good reference and indication on how to properly perform such analysis.

F. Albermani et al. [14] advocate the use of nonlinear analysis as a tool to improve design accuracy and failure prediction, aiming to reduce the need of full-scale testing. Their in-house built *FE* solver, which accounts for geometrical and material nonlinearities, has been used to conduct analysis on different loading cases on a high-voltage transmission tower and has predicted the collapse location and load within 5% of the test result. F. Alminhana et al. [15], adopted the nonlinear method from [14] in their transmission line cable rupture time-response analysis, obtaining results within ±12% of the test data.

W. M. Wang et al. [16], used *FEM* to analyze the progressive collapse of transmission tower-line system under earthquake, applying material nonlinearities (bilinear elastic material model) and element death via *VUMAT* subroutine.

Y. M. Darestani, et al. [17] analyzed the impact of nonlinear material and geometry, imperfections, joint flexibility and failure, as well as stochastic uncertainties, in a pushover analysis using the *FE* software *OpenSEES*, with the purpose of determining the load-bearing capacity under the specific load case. The large scatter of the ultimate load capacity indicates a particular sensitivity on applied imperfection modes.

J. Wang et al. [18] employed the *Eigenmode Assembly Method (EAM)* based on the superimposition of multiple imperfection modes obtained from a *Linear Buckling*

Analysis (LBA), suggesting the best way to model imperfections. C. Affolter et al. [19] analyzed the collapse, due to structural instability, of a high storage rack by means of *FEA* using *Abaqus CAE*. They applied both buckling Eigenmodes imperfections as well as local ones (dents).

N. P. Rao et al. [20] used nonlinear *FE* analysis software *NE-Nastran*, applying the *Arc-Length method* built within it, with the initial purpose of replicating a transmission tower test and ultimately achieved with 3-14% error, accounting for both geometrical and material nonlinearities. In further studies of theirs ([21, 22]), they described the load - displacement curve and rupture position within the same range of accuracy.

Most of the presented techniques, alongside novel proposed approaches, are going to be used in the current study. More on this topic in the following section.

Outline of the study

Methodology

The presented study aims to improve on the failure analysis approach adopted by *IED* [10], by shifting the focus as much as possible on real structural capacity instead of relying on design standards.

For this purpose, *Simulia Abaqus CAE 2021* [4] has been adopted, as it is a general-purpose *3D FE* tool that opens up to a large variety of approaches, including Arc-length methods ([20-22]). Based on the above mentioned past works, introducing all sorts of required model imperfections ([17, 19]), nonlinearities (both geometrical and material) ([14-18]), and joint flexibility (as opposed to a "fixed" or "pinned" approach) ([17]). Moreover, the model was built with different element types and arrangements that better suited the tasks.

Goals

The following questions are going to be developed:

1. *Which is the best way to perform FEA for structural instabilities?*

2. *How would joint flexibility influence the FEA?*

3. *Which modeling approaches are applicable to the modeling of large lattice structures with a multitude of joints?*

4. *What is the load-bearing capacity of the high-voltage transmission towers in AlbulaPass and their sensitivity to imperfections? How is it far from the static design load?*

5. *How can a cascade sequence occur in the power transmission line and, possibly, where it is more likely to have started?*

Structure of the thesis

The structure is summarized in Figure 0.16.

In **Chapter 1**, the optimal procedure and approach for *FE* modeling of structural instabilities is studied. The chapter presents basic concepts of the structural stability under the external loads and the post-instability behavior, as well as the procedures offered by the *FE* software and their applicability to the problem. Some indications on the optimal practices are given as a result of a sensitivity analysis.

In **Chapter 2**, the validation of column nonlinear *FE* models is performed. Both experimental data from buckling tests and design standards are employed for this purpose.

In **Chapter 3**, the modeling of joints in lattice towers is introduced. Two bolted column models with end flexibility are presented and validated against *FEM* and experimental results.

The modeling approaches discussed in Chapters 2 and 3, then applied in **Chapter 4** to lattice assemblies, in order to prove feasibility for larger structures, with some inherent limitations.

In **Chapter 5**, the chosen strategy from Chapter 4 is used to build the towers from the Failure Analysis case. Different wind models from design codes are compared, to find a better load assumption. Their ultimate load capacity is estimated via push-over analysis, and an imperfection sensitivity analysis is carried out.

In **Chapter 6**, the transmission line cascade effect and the collapse sequence hypothesis are investigated, trying to identify the starting point. A simplified multi-body model of the entirety of the line has been built for the purpose, and the full cascade dynamics is simulated.

Dynamic and resonance effects, as well as constraints and possible improvements to the modeling approaches are briefly discussed in **Chapter 7.**

The overall conclusions and final comments are drawn in **Chapter 8**.
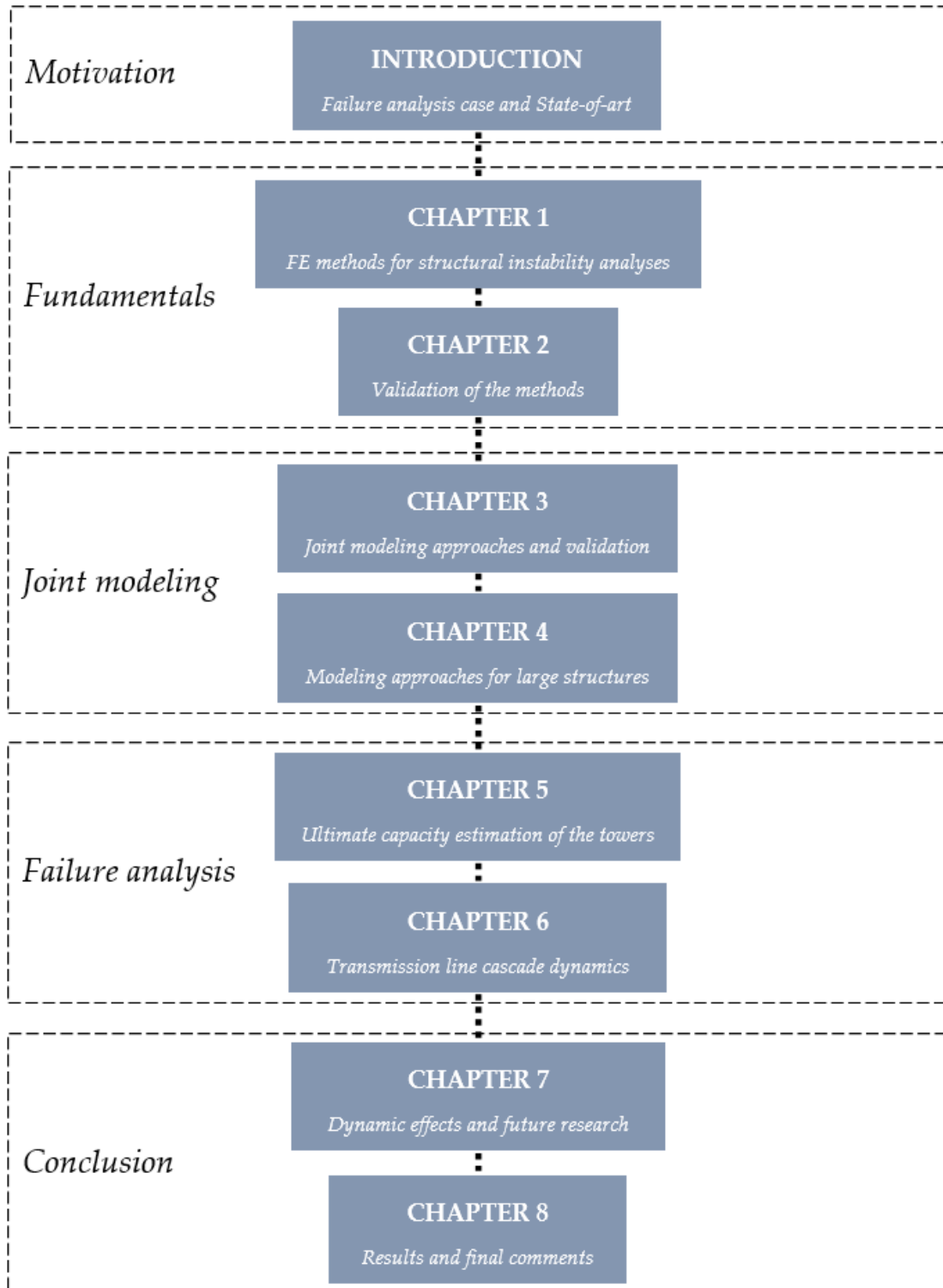
Figure 0.16: Structure of the document and interconnections between different chapters.

1 Chapter one: Best practices for FEA of structural instabilities

The study of structural instabilities with *FE* tools is not a trivial enterprise, especially if there are computational power restrictions or high complexity in the model.

It is well recognized the correlation between mesh size, solution error and time required to compute the solution (Figure 1.1).
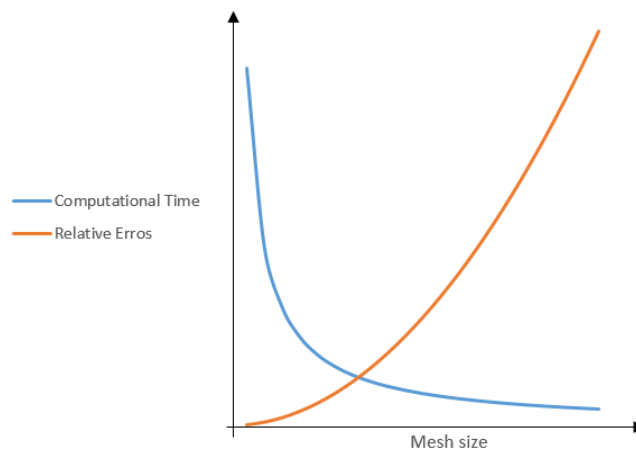
Figure 1.1: Qualitative representation of the relationship between mesh size, solution error and computational time.

Therefore, it is of prime importance to find a compromise between these two opposing variables at the very beginning with a simple, manageable model, in order to set a standard to keep for every further, more complex analysis in the study.

In this initial chapter, the structural instability topics, as well as available types of analysis, mesh and material models within *Simulia Abaqus CAE 2021* [4], are presented and compared in order to set standard methodology for further approaches.

With the purpose of validating the *FEA* results, both analytical formulae and design codes are going to be employed.

1.1. Introduction to the structural instabilities

Mechanical components can fail due to structural instabilities under loads considerably lower than the material strength, leading to a sudden collapse. The problem depends on the equilibrium state internal energy (Figure 1.2) and is a major issue in geometries such as slender columns or thin plates, when the applied loads are of the compressive kind.
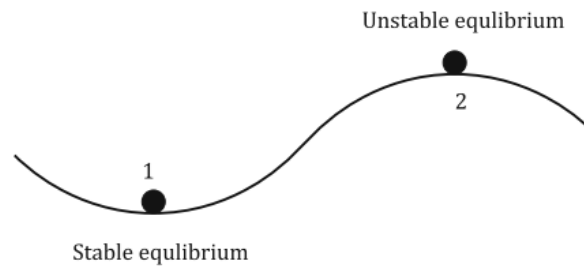
Figure 1.2: Physical explanation of the equilibrium state: when the ball in 1 is given a small disturbance, it would ultimately return to the initial position (stable); any small input to the ball in 2 makes it move away to a new equilibrium state (if exists) [23].

In general, three types of static instability are recognized: *classical buckling* or *bifurcation*, *finite disturbance buckling* and *snap-through buckling*. The kind depends upon factors such as the geometry of the structure, the initial geometric and load imperfections, and boundary conditions. These factors also outline whether the post-buckling path might be stable or not (if, following the instability, a new equilibrium state can be reached).

As for the first type of instability, the structure undergoes a secondary deformation that amplifies the loading, up to a point of instability. The usual representation is of a beam-like member under compression (Figure 1.3).
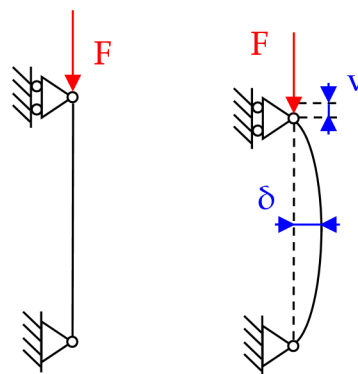
Figure 1.3: Beam member under compression.

If the loading is increased, a *bifurcation point* is reached, upon which the stiffness of the system suddenly changes the beam undergoing lateral deflection (secondary deformation). This secondary path could be either stable or unstable, depending on the potential energy function concavity (similarly to what it is shown in Figure 1.2), which again is a function of the applied force: if the force is over the critical limit, the instability will occur at the bifurcation point.

(a) Load-deformation curve.   (b) Potential energy function.
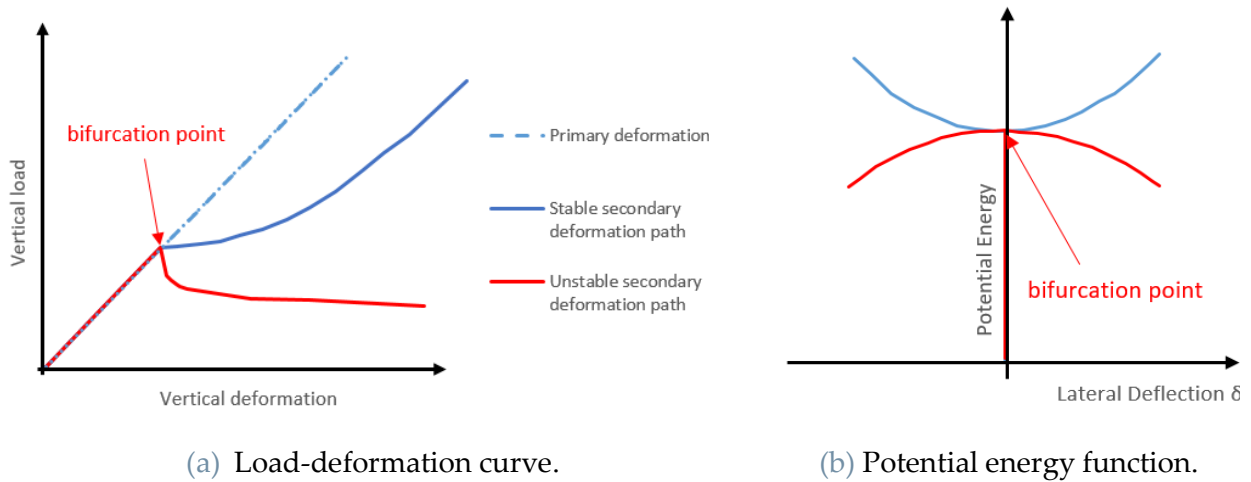
Figure 1.4: Stable and unstable secondary paths.

In this case, the post-buckling behavior is always unstable, since the load-carrying capacity of the column is completely hindered.

There are other examples in which, after the bifurcation point is reached, a stable post-buckling path is obtained.

This is the case of a cylindrical shell under compression or a shallow arc under distributed load.

(a) Shell cylinder under compression.   (b) Shallow arc under distributed load.
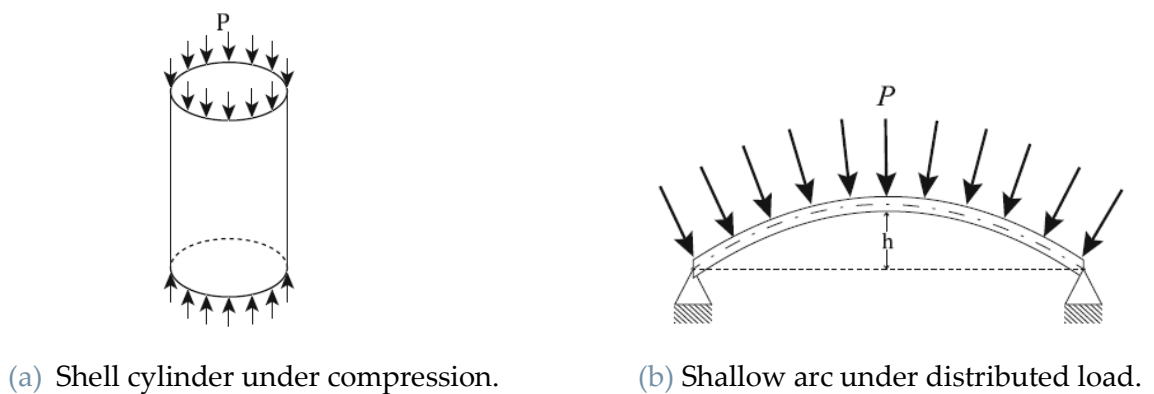
Figure 1.5: Other examples of structural instabilities present in [23].

In the first example, after the first bifurcation point, the load drops and the cylinder wrinkles, in what is called *finite disturbance buckling*.

In the second, when the arc reaches the instability, it suddenly snaps to the opposite deflection shape, obtaining *snap-through buckling.*
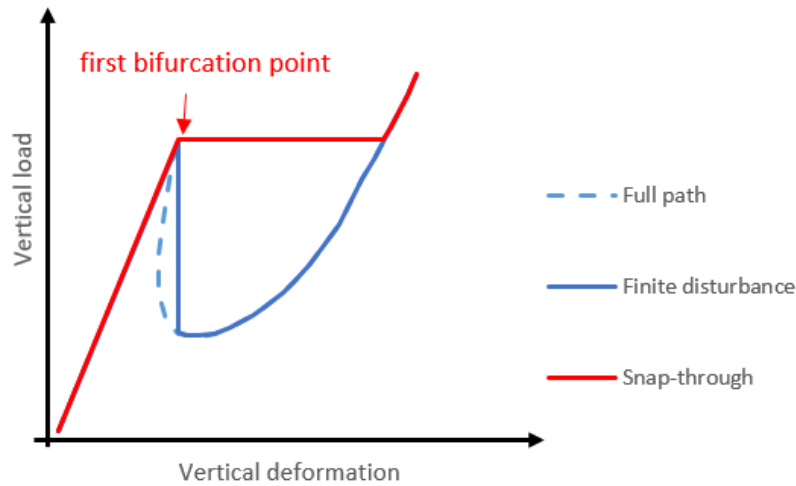
Figure 1.6: Post-buckling behavior in *finite disturbance* and *snap-through buckling*.

The limit critical load for columns is traditionally set by the *Euler buckling formula* [24] or the *Secant formula* [25] for eccentric loading (examples of analytical solutions can be found in the next Chapter 1 and 2), which are derived from the maximum bending moment in the deformed shape.

The solution results as an inverse function of the beam slenderness, function of the length and section properties, and it is always based on the hypothesis of linear elastic deformations (reason for which the limit is often called *Elastic buckling formula*):

$$F_{cr} = \frac{K^2 \cdot E \cdot I}{L^2} = \frac{K^2 \cdot E}{\lambda^2} \tag{1.1}$$

Where $\lambda = L \cdot \sqrt{\frac{I}{A}}$ is the slenderness ratio, E Young's modulus of the material, the chosen axis moment of inertia, A the section area and L the length of the element.

K is a boundary condition dependent variable, which has to be modified according to the end restrains (for example $K=\pi$ for pinned columns*)*. The buckling solution, in fact, is highly sensitive to boundary conditions that can considerably change the load capacity and deformed shape, thus the instability point.

When reducing the slenderness, the buckling critical load approaches the yield load
that causes the section plasticization. The prediction of the bifurcation load in this
area, with both yield and buckling limits, is quite poor and leads to overestimation,
showing an effect of the section yielding in the secondary deformation stiffness.

For this reason, this area goes by the name of *inelastic buckling* and the limit is set by
experimental formulation (such as *Eurocodes buckling curves*), depending on section
and material.

An example of the application of the Euler formula and the codes can be found in
the following chapters.
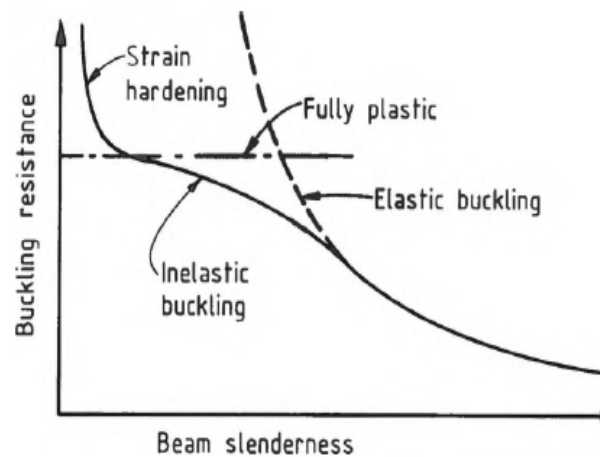
Figure 1.7: Buckling limits comparison [26].

The final load-displacement curve can differ quite a lot if, in fact, more details are
introduced into the model, such as geometric or material nonlinearities (Figure 1.8).
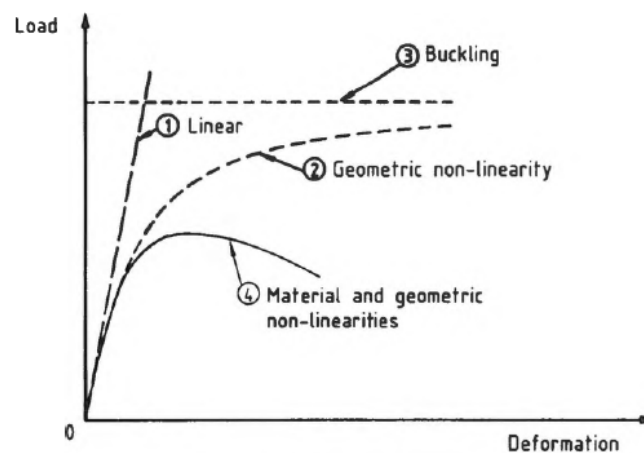
Figure 1.8: Example of load-displacement curve variation, accounting for model geometric
or material nonlinearities [26].

In load and deformation in the structure can be aligned in the same direction or not, depending on the specific classification of instability.
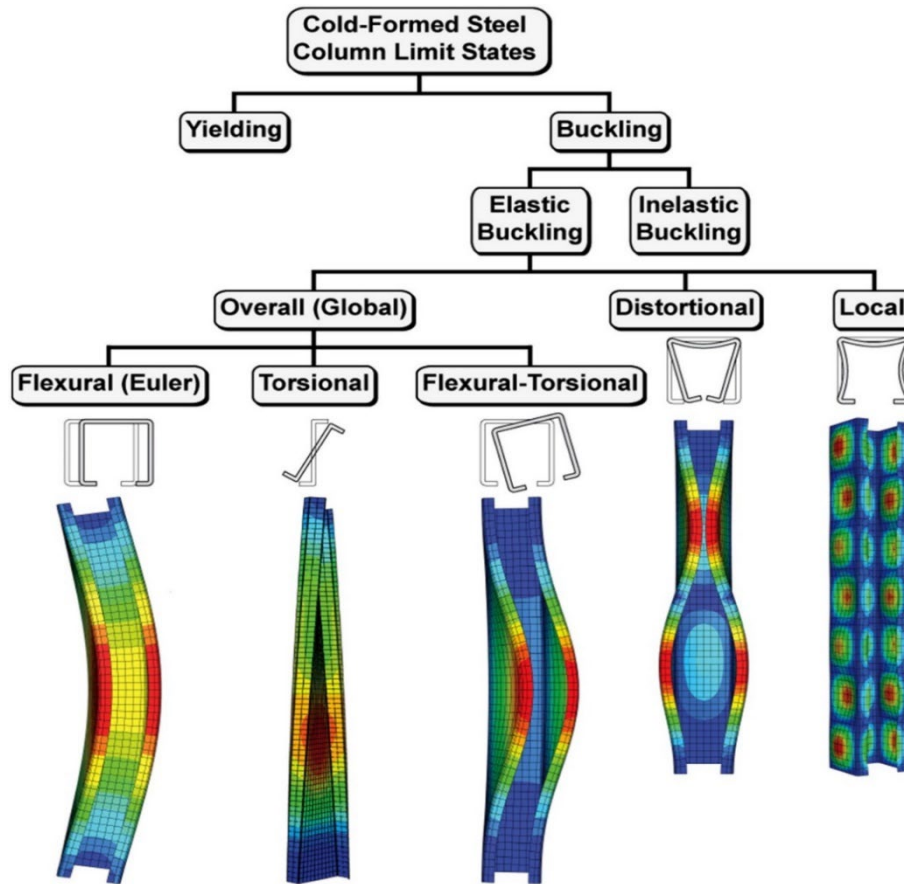
Figure 1.9: Types of possible limit states in columns [27].

In this section, the focus was placed more on the *flexural buckling*, in which the secondary deformation is on the bending around a specific axis. Many other types of structural instabilities do exist (Figure 1.9), but are not in the specific interest of this study, mainly addressing constrained ends *Angle (L-section)* columns subjected to axial loading.

It has to be mentioned that some studies (P. B. Dinis et al. [28]) proved that if the section is particularly thin, *torsional* and *flexural-torsional buckling* could play a relevant role and lower the allowable compressive load limit quite a bit.

However, the analytical or empirical solutions to other buckling modes (like the ones proposed by the *Eurocodes* [4]), are convoluted and require complete knowledge of the forces and moments in the end restrains and state of stress within the element. On top of that, it might not suit a failure analysis case, as the level of approximation and conservativeness applied by the code is unclear.

1.2. Example of buckling problem and solution

The chosen model for the study is a simple *"Pinned-Fixed" beam* under compression (one end completely restrained and the other free to rotate around the cross-section centroid, see Figure 1.10), in order to calculate the analytical solution with ease.

The length of the beam has been chosen as L=1900mm, with an "L" (*Angle*) cross-section L50x4 mm, for two main reasons: to have cross-section and slenderness comparable with the ones present in the larger tower model, and in order to remain in the "*Elastic buckling*" region (refer to Figure 1.7), thus having an accurate analytical solution.

The section properties are listed in Table 1.1, based on Figure 1.10. It is possible to see how the moment of inertia in *v-v* axis (secondary) is the lowest, hence it is the most critical.
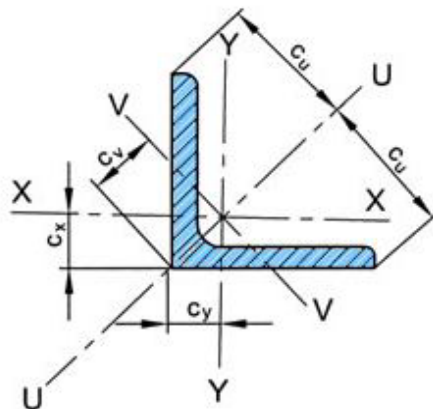
Figure 1.10: *"Angle"* section dimensions.

Property	I_{xx}	I_{yy}	I_{xy}	I_{uu}	I_{vv}	c_x	c_y	c_v	c_u	A	E
Value	92607 mm⁴	92607 mm⁴	55102 mm⁴	147712 mm⁴	37503 mm⁴	13.98 mm	13.98 mm	19.77 mm	35.36 mm	384 mm²	208 GPa

Table 1.1: List of section L50x4 properties.

1.2.1. Analytical solution

The first approach is based on the solution of the equilibrium equation of the deformed column (Figure 1.11).
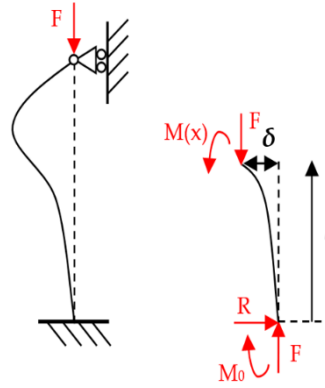
Figure 1.11: Deformed column diagram

The bending equilibrium at distance x is then given by the following equation:

$$M(x) = M_0 - F \cdot \delta - R \cdot l \tag{1.1}$$

With M bending moment through the column length, M_0 bending moment at the fixed end, F vertical force and δ the lateral deflection.

At $l{=}0, \delta(L) = 0$:

$$M(L) = 0 = M_0 - R \cdot l \tag{1.2}$$

$$M_0 = R \cdot x \tag{1.3}$$

$$M(l) = -F \cdot \delta - R \cdot (l - L) \tag{1.4}$$

If we introduce the *Euler Beam* bending moment equation:

$$M(l) = E \cdot I \cdot \frac{\partial^2 \delta}{\partial l^2} \tag{1.5}$$

We finally get the following differential equation:

$$\frac{\partial^2 \delta}{\partial l^2} + K \cdot \delta = \frac{R}{E \cdot I} \, (l - L) \tag{1.6}$$

with $K = \sqrt{\dfrac{F}{E \cdot I}}$. Its solution is of the type:

$$\delta(x) = C1 \cdot \sin(K \cdot l) + C2 \cdot \cos(K \cdot l) + C3 \cdot (L - l) \tag{1.7}$$

The solution to this equation can be found by applying the problem boundary conditions:

$$
\begin{cases}
\delta(0) = C1 \cdot 0 + C2 \cdot 1 + C3 \cdot L = 0, & \text{(1.8a)} \\
\delta(L) = C1 \cdot sin(K \cdot L) + C2 \cdot cos(K \cdot L) + C3 \cdot 0 = 0, & \text{(1.8b)} \\
\dfrac{\partial \delta}{\partial l}(0) = K \cdot C1 \cdot 1 - K \cdot C2 \cdot 0 + C3 = 0 & \text{(1.8c)}
\end{cases}
$$

From which the coefficients of the non-trivial solution ($\delta(l) \neq 0$) can be derived:

$$
\begin{cases}
C2 = K \cdot L \cdot C1, & \text{(1.9a)} \\
C3 = -K \cdot C1, & \text{(1.9b)} \\
tan(K \cdot L) = K \cdot L & \text{(1.9c)}
\end{cases}
$$

The solutions of from Equation 1.9c can be found only iteratively and the first three solutions (modes) are reported in Table 1.2.
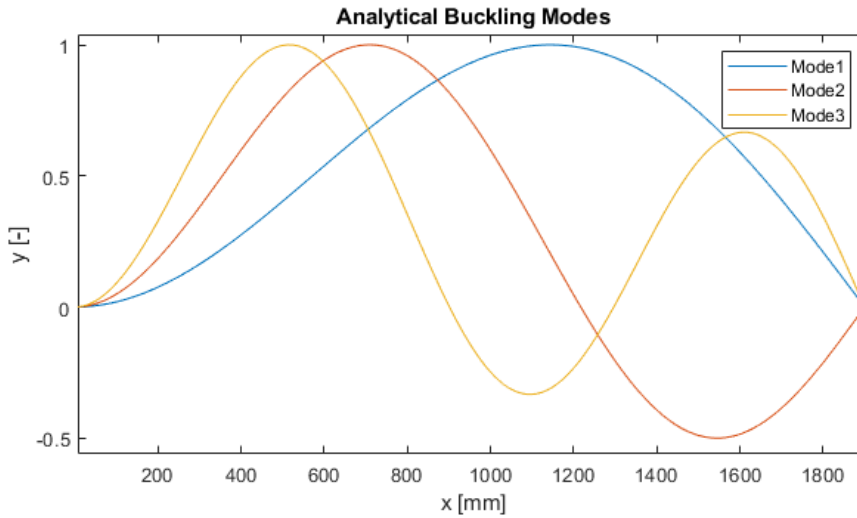
Figure 1.12: Deformed mode shapes 1, 2 and 3 according to the results.

Mode	$K \cdot L$ that satisfy Equation 1.9c
1	4.4934
2	7.7253
3	10.904

Table 1.2: List of $K \cdot L$ values that satisfy the equation.

The resulting deformed shapes are shown in Figure 1.12. The highest deflection point is located at 59.8% of the length for mode 1, 37.2% and 27.1% for mode 2 and 3 respectively.

The critical buckling load is then found by reversing the formula into Equation 1.10:

$$F_{cr} = \frac{(K \cdot L)^2 \cdot E \cdot I}{L^2}$$

(1.10)

The formula is also known under the name of *Euler buckling formula* [24].

The different modes solution can be quantitatively appreciated in Table 1.3.

Mode	F_{cr} in *x-x, y-y* [kN]	F_{cr} in *u-u* [kN]	F_{cr} in *v-v* [kN]
1	107.7	171.8	43.6
2	318.4	507.9	128.9
3	634.4	1011.9	256.9

Table 1.3: Critical buckling loads in every bending axis.

Naturally, the solution of interest is the lowest load of 43.6 kN at which the column buckles on the *v-v* axis.

1.2.2. EC 1993-1.1

The *Eurocode 1993-1.1* [29], based on experimental data, reduces the buckling critical load limit in order to account for the inelastic region, in which there is an interaction between the plasticized section and the buckling mode.

The formulation is taken without the safety factor, as the pure limit is sought.

It has to be said that, however, the formulation of a standard is often very conservative and would consequently give underestimated validation data (supported also by Kettler et al. [30]). Data that would be kept as a lower bound to support our simulation.

$$F_{lim} = X \cdot A \cdot S_y$$

(1.11)

$$\lambda_n = \sqrt{\frac{A \cdot S_y}{F_{cr,eul}}}$$

(1.12)

$$\Phi = 0.5 \cdot (1 + \alpha_\lambda \cdot (\lambda_n - 0.2) + \lambda_n{}^2) \tag{1.13}$$

$$X1 = \frac{1}{\Phi + \sqrt{\Phi^2 - \lambda_n{}^2}} \tag{1.14}$$

$$\begin{cases} X = 1, & if \ X1 > 1 \\ X = X1, & if \ X1 < 1 \end{cases} \qquad \begin{matrix}(1.15a)\\(1.15b)\end{matrix}$$

With $X, X1,$ and Φ buckling parameters, λ_n normalized slenderness ratio according to EC 1993-3.1, and $\alpha_\lambda = 0.34$ imperfection factor for angles.

With $\lambda_n < 0.2$ the buckling effect could be ignored and the limit is the one for pure compression ($X = 1$).
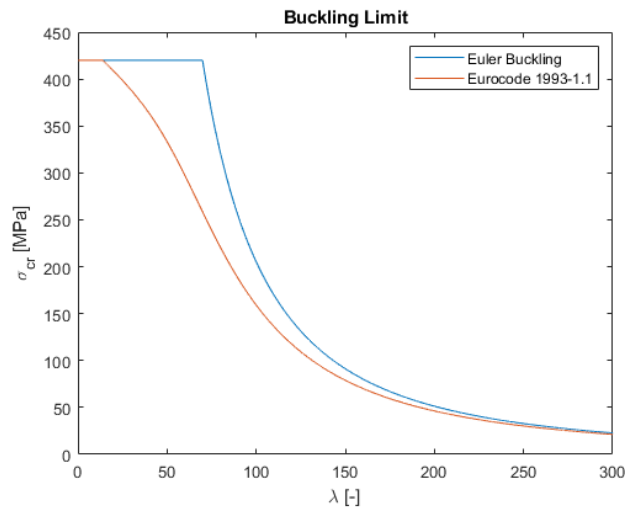

Figure 1.13: Stress limit according to Euler and Eurocode function of the

slenderness.

The buckling limits according to the code are displayed in Table 1.4.

F_{cr} in x-x, y-y [kN]	F_{cr} in u-u [kN]	F_{cr} in v-v [kN]
76.5	101.8	36.8

Table 1.4: Critical buckling loads in every bending axis.

The buckling limit, as well as the slenderness ratio, changes according to the considered axis. It is more natural to display the buckling limit load as a function of the element length instead, in order to immediately spot the axis with the lowest margin.
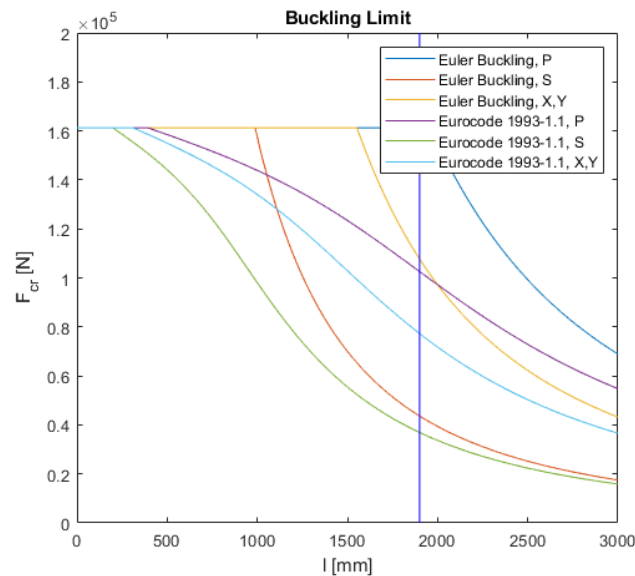
Figure 1.14: Limit load for buckling in different axis. *X* and *Y* refer to the *x-x* and *y-y* axis, *P* to the principal axis (*u-u*), *S* to the secondary (*v-v*).

It is clearly noticeable how the limit introduced by the *Eurocode* curve affects mostly the inelastic buckling region, while it is very close to *Euler* for higher slenderness ratios. In the analyzed case, the lowest limit is in the *v-v* axis and it is equal to 36.8 kN, 13.4% lower than the analytical solution.

1.3.   Introduction to FE procedures in Abaqus

All the Finite Element calculations have been made using *Simulia Abaqus CAE 2021* [4]. The software offers different possibilities of analysis procedures and it is relevant to understand the strength and weaknesses of each and ultimately choose the most adequate for our final purpose.

1.3.1. Linear Buckling Analysis (LBA)

Abaqus *linear buckling analysis (LBA),* as the name hints, is based on the structural linearity theory, therefore inheriting the limits of the approach:

- Small displacements (thus strains)

- Linear elastic material with constant properties (no strain-, strain rate-, temperature-dependent property variation are accounted for)
- Definite stiffness matrices (excludes contact and friction between elements, connector elements and rigid body motion)

The procedure finds the buckling *Eigenmodes* that make the stiffness matrix singular, based on the initial perturbation (force, stress field or prescribed motion):

$$[K] \cdot \bar{u} = \bar{0} \tag{1.16}$$

Therefore, the solution is the series of eigenvalues of the introduced perturbations that make the system unstable (upon which the stiffness is equal to zero). However, it does not mean that the capacity of the structure is always the one that causes instability.

Some of this procedure's limitations can be partly overcome in a second-order *load-displacement (LD)* analysis. A first *LBA* on the structure is anyway always required in order to obtain an initial estimate of the collapse load and the deflection modes, which can be used as initial geometrical imperfections in the *LD* analysis (as generally required for second-order analysis in the *Eurocodes*).

1.3.2. Static and dynamic implicit

The *"General, Static"* and *"Dynamic, Implicit"* procedures are based on the implicit (*Standard*) solver, which finds the new increment's solution from a function of both the current and new state, resulting in a coupled system of equations that requires iterative methods (such as *Newton-Raphson's*) to compute a solution.

Both of them are able to deal with every type of nonlinearity and complexity. The time increment size is not fixed and relatively large, depending on the system complexity and dynamics.

The static solver excludes most dynamic behavior and equations (completely neglecting, for example, inertia forces) in favor of a much quicker computational time and large time increments, thus obtaining steady-state solutions.

The dynamic solver includes the dynamic response, but the large increments could miss, in some specific cases, some quick transients or high-frequency dynamics, resulting in errors: if large enough to overcome iterative solution relative error threshold, the solver might not reach solution convergence. It has to be noted, however, that *Abaqus* includes some internal strategies to obtain more accurate results in these specific cases.

1.3.3. Dynamic explicit

The *explicit* solver (*"Dynamic, Explicit"* procedure) finds the exact solution of an equation in which the next increment state is direct function of the previous one.

This results in a much more accurate computation, with the only possible source of errors being numerical. The best practice suggests reduction via the use of finer mesh and double-precision numbers.

The computational effort needed for every increment is incredibly small, but, in order to solve the equation, it is required to have a very tiny time increment as well to capture all the dynamic effects within the system.

For this reason, the time increments depend on the element size $l_{element}$ and speed of sound s through the material:

$$\Delta t \approx \frac{l_{element}}{c}; \quad s = \sqrt{\frac{E}{\rho}} \qquad (1.17); (1.18)$$

Where ρ is the material density.

Therefore, this kind of approach finds its use in cases in which the problem size and complexity is large and with very fast dynamics, where the implicit approach would require more iterations to find the solution.

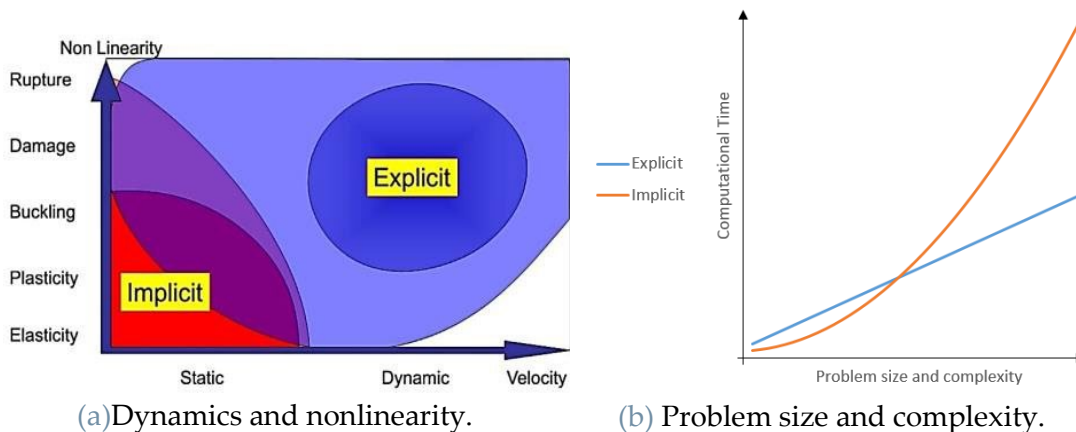(a) Dynamics and nonlinearity. (b) Problem size and complexity.

Figure 1.15: Implicit and explicit comparison.

1.3.4. RIKS / Arch – Lenght method

"General, RIKS" procedure is presented as a different approach to the *LD* problem by detaching from time as the independent variables.

In this method, the increments are no longer time-based, but, in fact, *Arc length* based (also alled *Arc-Length* method)

This new variable is the length of the path between two increments in the load - displacement curve as displayed in the following diagram.
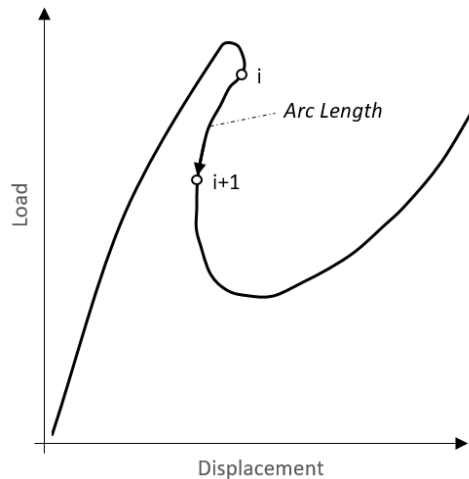

Figure 1.16: *Arc-length* increment displayed in load - displacement curve.

Both the load and displacement are then variables in the simulation and they can vary deliberately in magnitude and direction, using the initial input value only when reaching the initial instability load.

The points of instability are stabilized via the introduction of fictitious viscosity to reach an equilibrium, later released in order to reach an accurate prediction at the following increment.

However, this approach requires the introduction of an initial imperfection (load eccentricity, mesh asymmetry or in boundary conditions), in order to guide the path after the point of instability.

The only limitation of this approach is that the dynamics (transients and vibrations) cannot be displayed (which could also be seen as an upside) and it cannot properly display bodies detachment in contact interaction problems (such as slip in bolted joints, which might be relevant in our study).

1.4.   FE modeling of buckling

The following analysis steps have been compared for different element types and mesh sizes:

1. *"Linear Perturbation, Buckle": for Linear Buckling Analysis (LBA).*

2. *"General, Static":* for static analysis.
3. *"General, RIKS":* for *Load-Displacement (LD)* analysis.
4. *"Dynamic, Implicit" and "Dynamic, Explicit":* for dynamic and quasi-static analysis.

P. Uriz et al. [31] presented modeling approaches to analyze inelastic buckling for different sections, aiming to achieve results that are more accurate. For modeling it in L-sections, they suggest at least 3-4 elements through the width of the flange and, when using *3D* elements, 2-3 elements through the thickness. Different combinations have been tried.

Shell elements in an angle section can be extruded from the mid-plane in different ways (Figure 1.17). The three cases have been tested.

(a) Top   (b) Mid   (c) Bottom
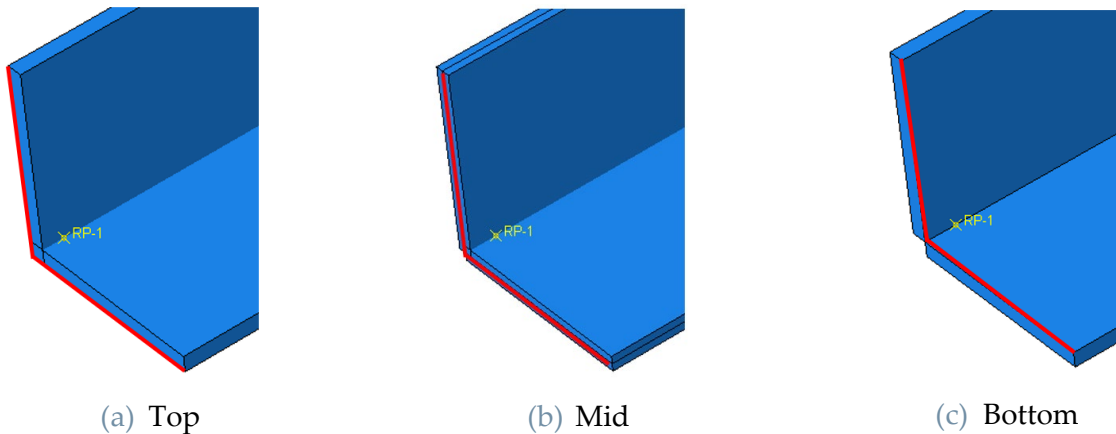
Figure 1.17: Types of *shell* element extrusion, highlighted in red the mid-plane.

The case in Section 1.2 was analyzed, and a set of different mesh sizes was initially selected for the analysis steps (Table 1.5).

Element type – element discretization – (size) – shell el. extrusion plane
1D Beam - Quadratic - (5 mm)
1D Beam - Linear - (50 mm)
1D Beam - Quadratic - (150 mm)
3D Shell - Quadratic - (5x5 mm) – top extrusion
3D Shell - Quadratic - (5x5 mm) – mid extrusion
3D Shell - Linear Full Integration - (5x5 mm) – bottom extrusion
3D Shell - Linear Reduced Integration - (15x40 mm) - mid extrusion
3D Shell - Linear Full Integration - (15x40 mm) - mid extrusion
3D Shell - Quadratic - (50x50 mm) - top extrusion
3D Shell - Quadratic - (50x50 mm) - mid extrusion
3D Shell - Quadratic - (50x50 mm) - bottom extrusion

3D Solid - Quadratic Full Integration - (5x5x1.33 mm)
3D Solid - Quadratic Reduced Integration - (5x5x1.33 mm)
3D Solid - Quadratic Reduced Integration - (5x5x4 mm)
3D Solid - Linear Full Integration - (5x5x4 mm)
3D Solid - Quadratic Full Integration - (12.5x30x2 mm)
3D Solid - Quadratic Red Int. - (12.5x30x2 mm)
3D Solid - Quad. Red. Int. - (16.66x70x4 mm)
3D Solid - Linear Full Int. - (16.66x40x4 mm)
3D Solid - Linear Red. Int. - (16.66x40x4 mm)
3D Solid - Quadratic - (50x50x4 mm)

Table 1.5: Selected mesh sizes.

Two different load introduction approaches have been used for the procedures:

- Prescribed motion in *"General, Static"*;
- Force controlled in *"Dynamic, Implicit"* and *"Dynamic, Explicit"*;
- Arc-length controlled in *"General, RIKS"*.

The simulations using explicit solvers were carried out with force-controlled *"General, Static"* preloading step, up to 80% the load-bearing capacity, in order to have a more efficient computation. As seen before, explicit solvers are fairly slow if used in simple but refined mesh models (Figure 1.15b) and not very keen on quasi-static forcing (Figure 1.15a) due to the limitation in time increment length (Equation 1.17). The preloading is achieved via *"Restart"* or *"Initial condition"* options, which allow the results (coordinates, displacements, material conditions and internal forces) to be transferred from the last step of one model to the first of another. This is extremely useful since *"General, Static"* and *"Dynamic, Explicit"* procedures are based on different solvers altogether and cannot be employed within the same model.

This results in a different behavior at discontinuities like the collapse of a structure, with the inertia of the structure playing a big role after the load capacity is reached. This is better shown in Figure 1.18: if the load - displacement curve is not monotonic, neither of the two approaches is correctly able to fully represent it, therefore a different approach for this specific case is required.

In all the analysis procedures, a standard imperfection (according to *Section 5.3.2, EC 1993-1.1* [29]) coefficient *e=l/300,* based on the first buckling mode, has been used.
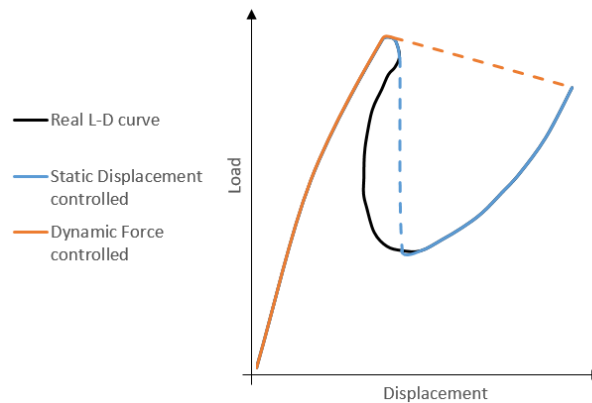
Figure 1.18: Post-collapse behavior in force and displacement controlled simulations.

1.4.1. Material models

The complete material characteristic is well known, thanks to thorough testing made by Empa on the specimens collected in the failure site. However, a more detailed material characteristic would prove to be challenging to be used for a very large model, increasing the problem complexity (and so the computational effort) without bringing effective benefits. For this reason, three different material models have been compared in the following section:

1. Linear Elastic: *linear* with simple Young's Modulus E=208000 MPa, Poisson's ratio v=0.3.
2. Elasto-Plastic: *bi-linear* with yielding at S_y=420 Mpa.
3. Nonlinear: full representation of the material true stress – true strain curve.

Figure 1.19 shows the different approaches for stress – strain curve.
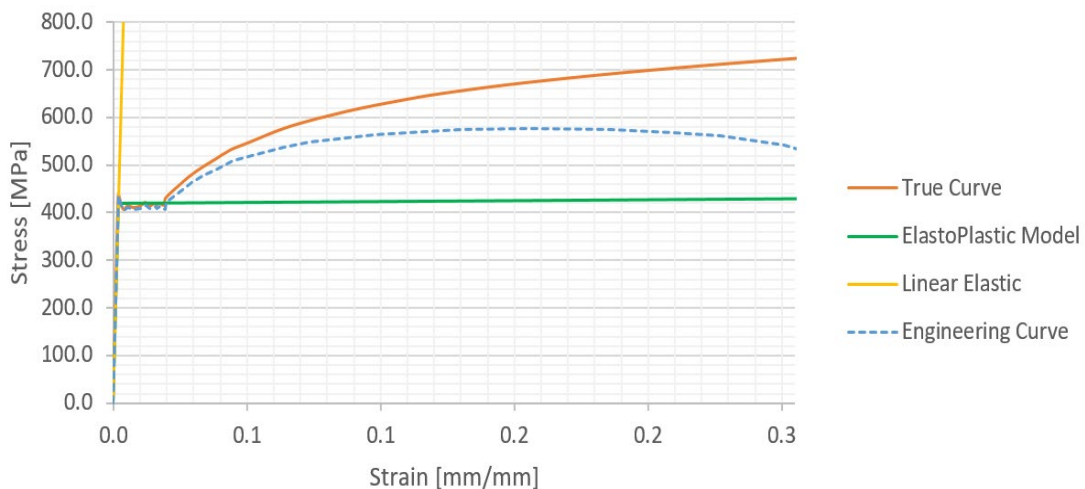

Figure 1.19: Material characteristics and different models.

Note: plastic deformation recovery upon unloading is left treated as isotropic hardening (same S_y both in loading and unloading), completely neglecting the kinematic hardening (*Bauschienger effect*). This simplification is supported by the fact that we do not expect, during the collapse, that the structure undergoes inelastic cycling or some parts reach yielding limit upon unloading and loading in the opposite direction, or, at least, not more than once, with a very limited overall effect.

Moreover, the *bi-lineari* model has a slight inclination (420 MPa at 0.2% strain to 430 MPa at 30% strain) to improve solver convergence, as it avoids large accumulation of strains at the yielding onset.

1.4.2. Linear Buckling Analysis (LBA)

With the initial *LBA*, the first 6 buckling *Eigenmodes* were analyzed.

In Figure 1.20 some examples of the usual modes the column undergoes are reported. Note that however not every mode is clearly displayed for every mesh type or/and size, and sometimes higher *Eigenmodes* are shown instead (Table 1.6). In this study, the focus would be on the 1st mode, being the one with the lowest critical load. The results from the 1st mode from *LBA* are summarized in Figure 1.21.

(a) 1st *flexural* Eigenmode on secondary axis.

(b) 1st *flexural* Eigenmode on x- or y- axis.

(c) 2nd *flexural* Eigenmode on secondary axis.

(d) 1st *torsional* Eigenmode.

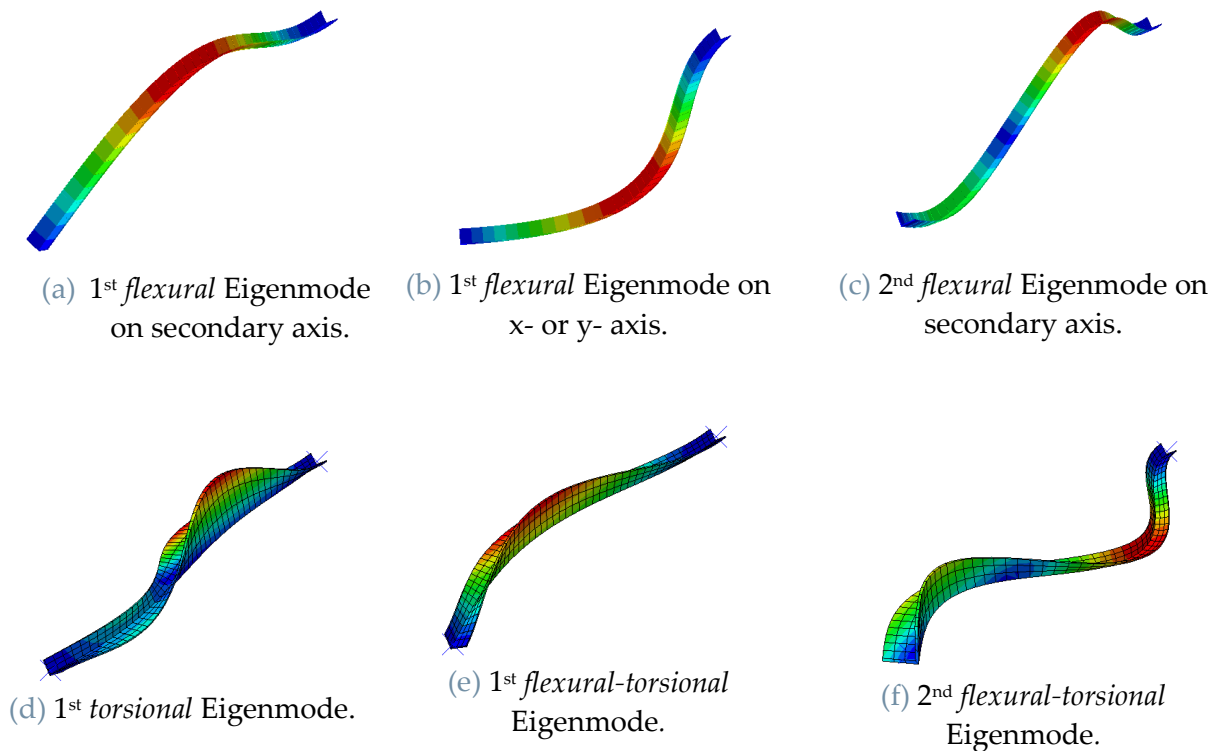(e) 1st *flexural-torsional* Eigenmode.

(f) 2nd *flexural-torsional* Eigenmode.

Figure 1.20: Buckling Eigenmodes from *LBA*.

Element type	Flexural, secondary		Flexural, x- or y-		Torsional	Flexural-torsional	
	Mode 1	Mode 2	Mode 1	Mode 2	Mode 1	Mode 1	Mode 2
Beam	o	o	o	o	x	x	x
Shell	o	o	x	x	o	x	o
3D	o	o	o	x	o	o	o

Table 1.6: Mode types the element is able (marked with "o"), or not (with "x"), to display.
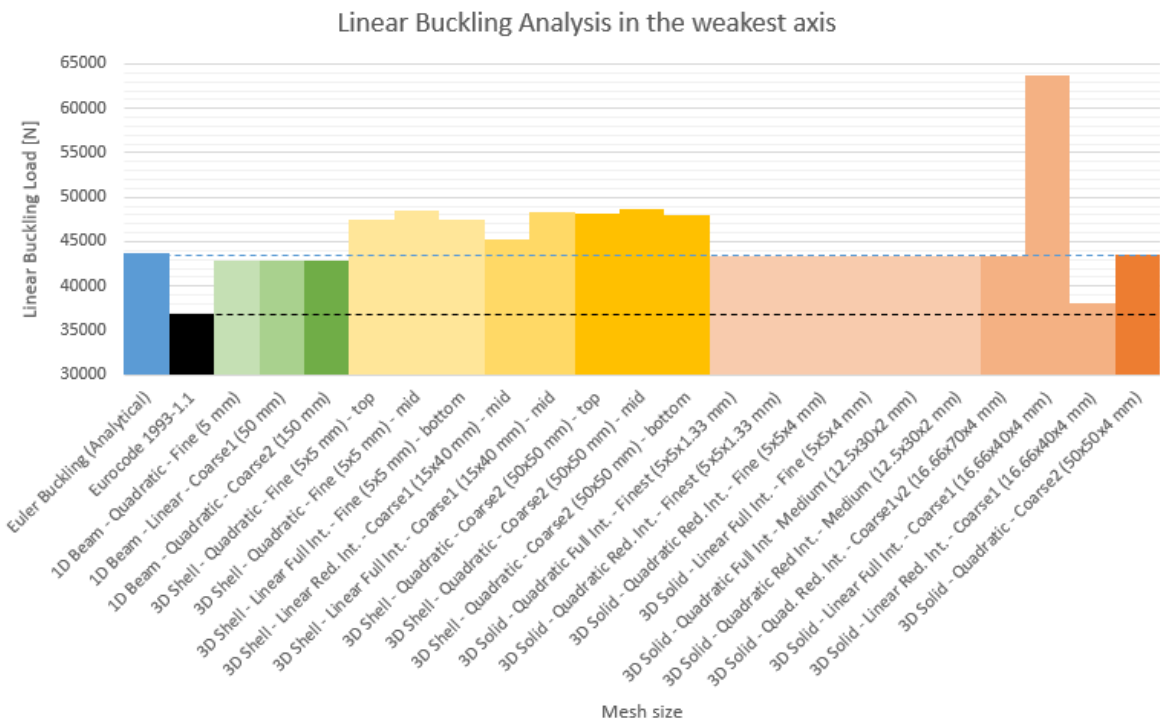

Figure 1.21: Linear buckling load for every mesh size. Notice the large disparity in very coarse *3D* elements.

Most of the mesh sizes match almost perfectly the *Euler* analytical result. Full integration elements are inconsistent and do not provide any improvement, while there is a slight difference if coarser meshes are discretized with linear or quadratic elements. The *Shell* elements have proven to be "*stiffer*" than *1D* and *3D* elements, and there is a scatter in ultimate load depending on the way the *shell* element is extruded (Figure 1.21).

The *Eurocode* load is considerably lower than the linear elastic solution.

1.4.3.   Nonlinear geometry, with linear elastic material

The results of the different types of analysis procedures are reported in Figure 1.22. The post-buckling behavior of the column is monotonic. It remains unclear why the dynamic simulations using *beam* element types have lower capacity.
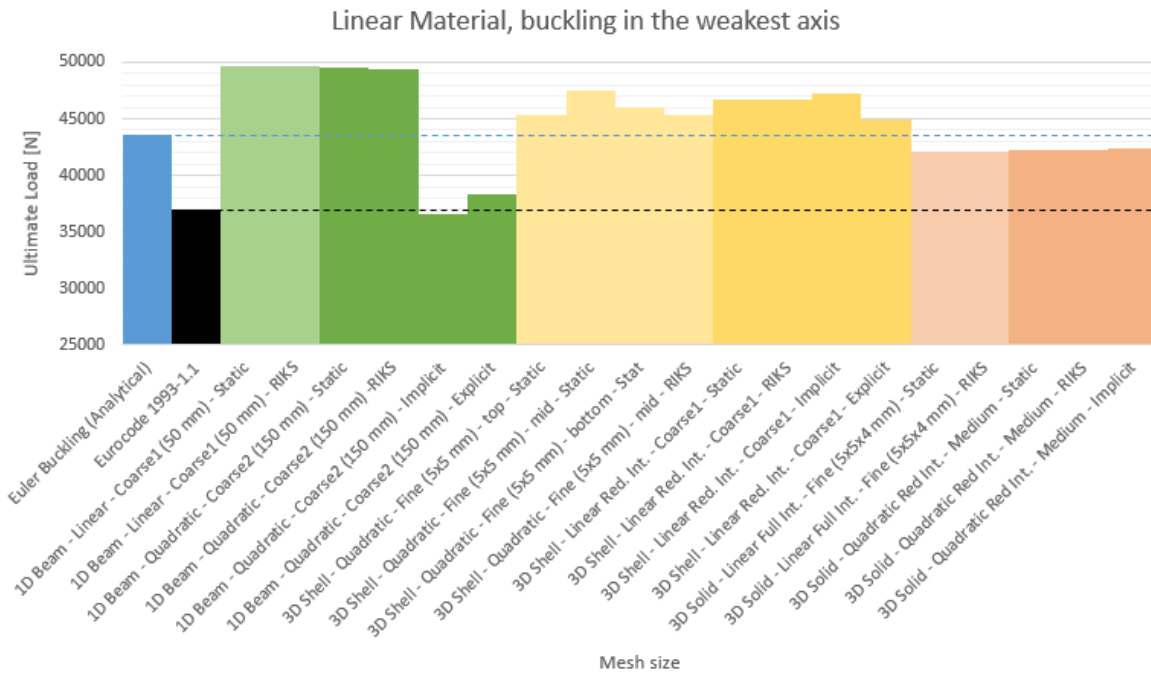
Figure 1.22: Load capacity for every mesh size and analysis type, linear material.

1.4.4. Material nonlinearity

By introducing the material nonlinearity, the section in the deflected area is fully plasticized (Figure 1.23), thus reducing the ultimate load. The deflection shape upon instability (Figure 1.24) in the bilinear or nonlinear models slightly shifts away from the midpoint of the column (located at 24.2% of the total length).

(a) Linear elastic material.
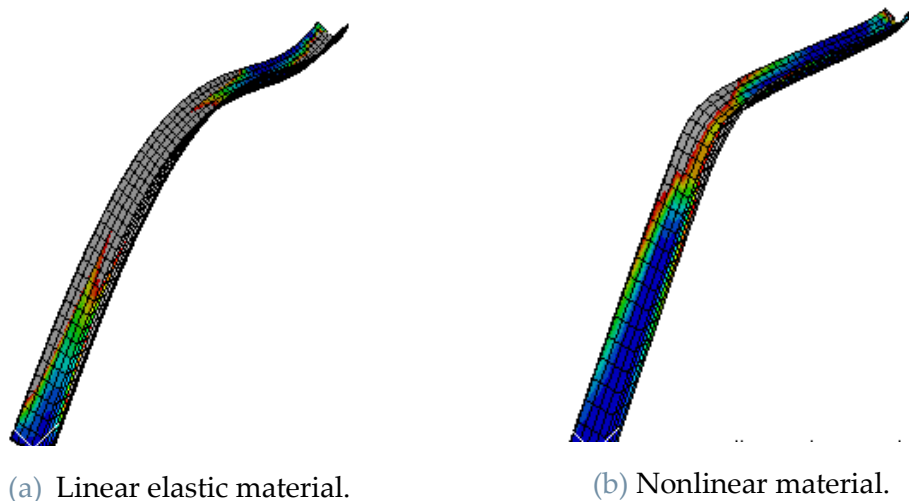
(b) Nonlinear material.

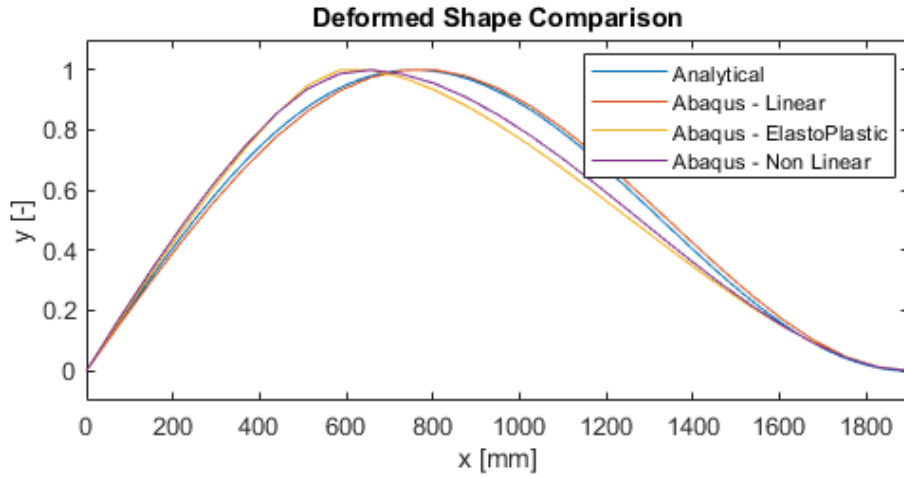Figure 1.23: Deformed column shape, in grey the area that has yielded.

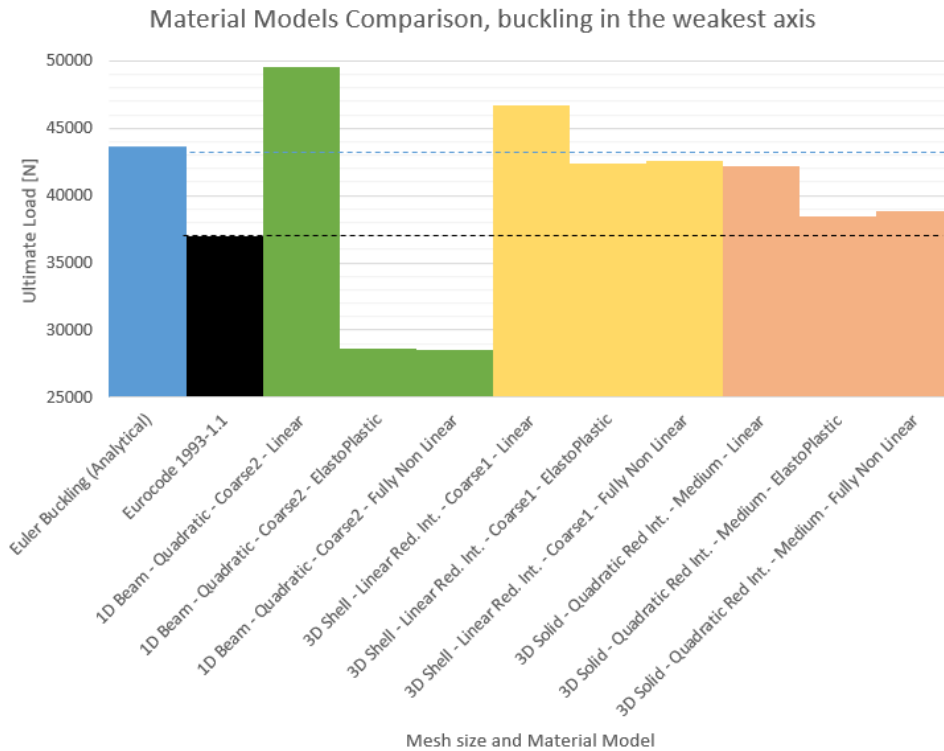Figure 1.24: Deflection shapes with different material models.

Figure 1.25: Load capacity for different material models and element types.

The *nonlinear* and *bilinear* material models are virtually equivalent (0.5% difference), as can also be observed in the load-displacement curves for "*General, RIKS*" procedures (Figure 1.25). For this reason, the *Elasto-Plastic* material model is almost as accurate as the complete curve and it is worth using it for the following nonlinear analysis of the study.

The load capacities (Figure 1.27) are now to be compared with the *Eurocode* values: *beam* elements seem to underestimate the load of 23%, while *Shell* and *3D* overestimate of 15% and 4.5% respectively.

(a) *Linear elastic* material.
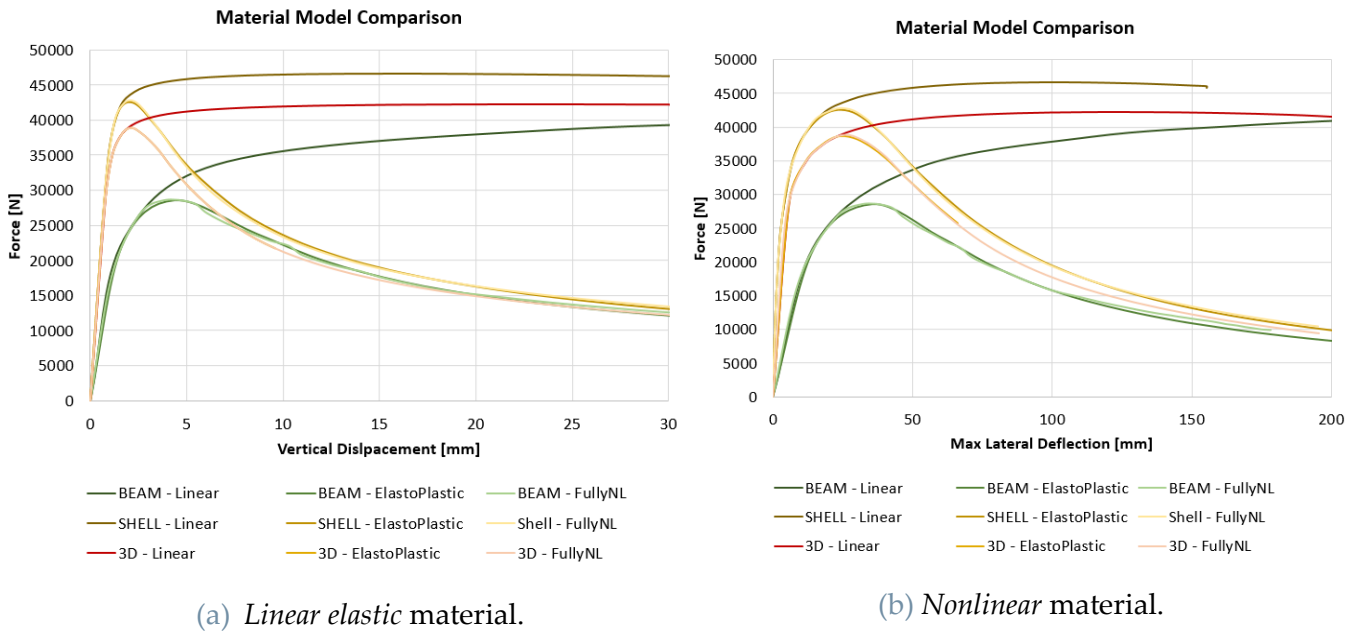
(b) *Nonlinear* material.

Figure 1.26: Load - displacement curves of different element type and material model,
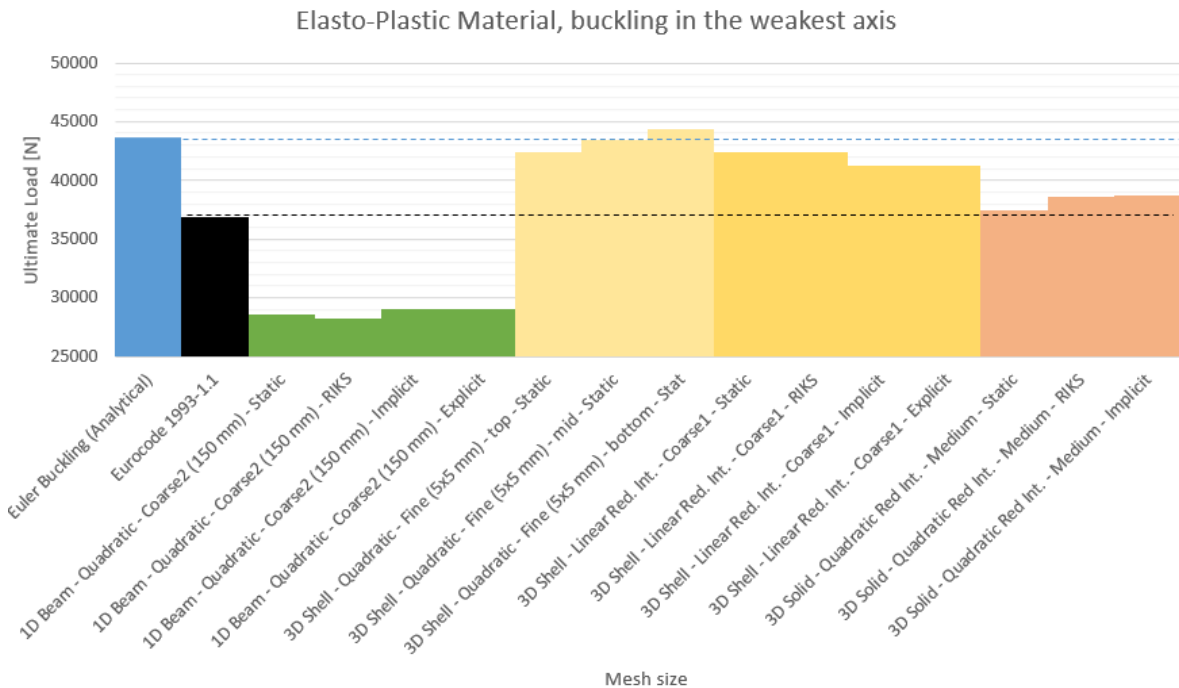performed in *Arc-Length* analysis procedure.

Figure 1.27: Load capacity for different mesh sizes and element types.

This structural energy released upon ultimate loading (highlighted in Figure 1.28)
is then converted into the acceleration of the structure during the sudden collapse
(*Snap*). With the nonlinear material, the dynamic simulations show inertia that
keeps higher stability in the post-buckling phase.
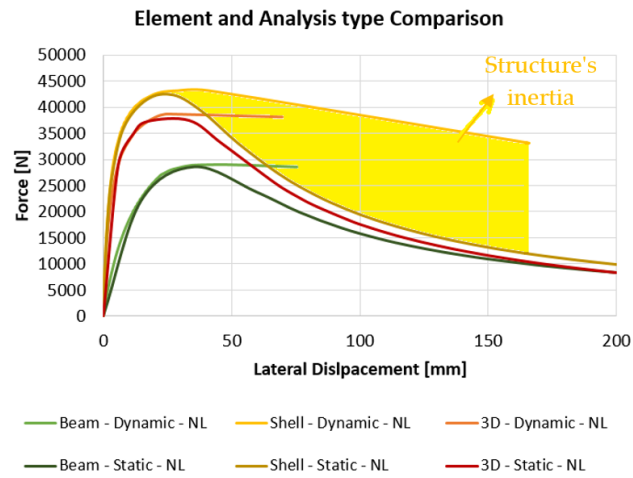
Figure 1.28: Load - displacement curve for different analysis procedures and element types.

(a) Fine *3D*.

(b) Medium *3D*.

(c) Coarse *3D*.

(d) Fine *Shell*.

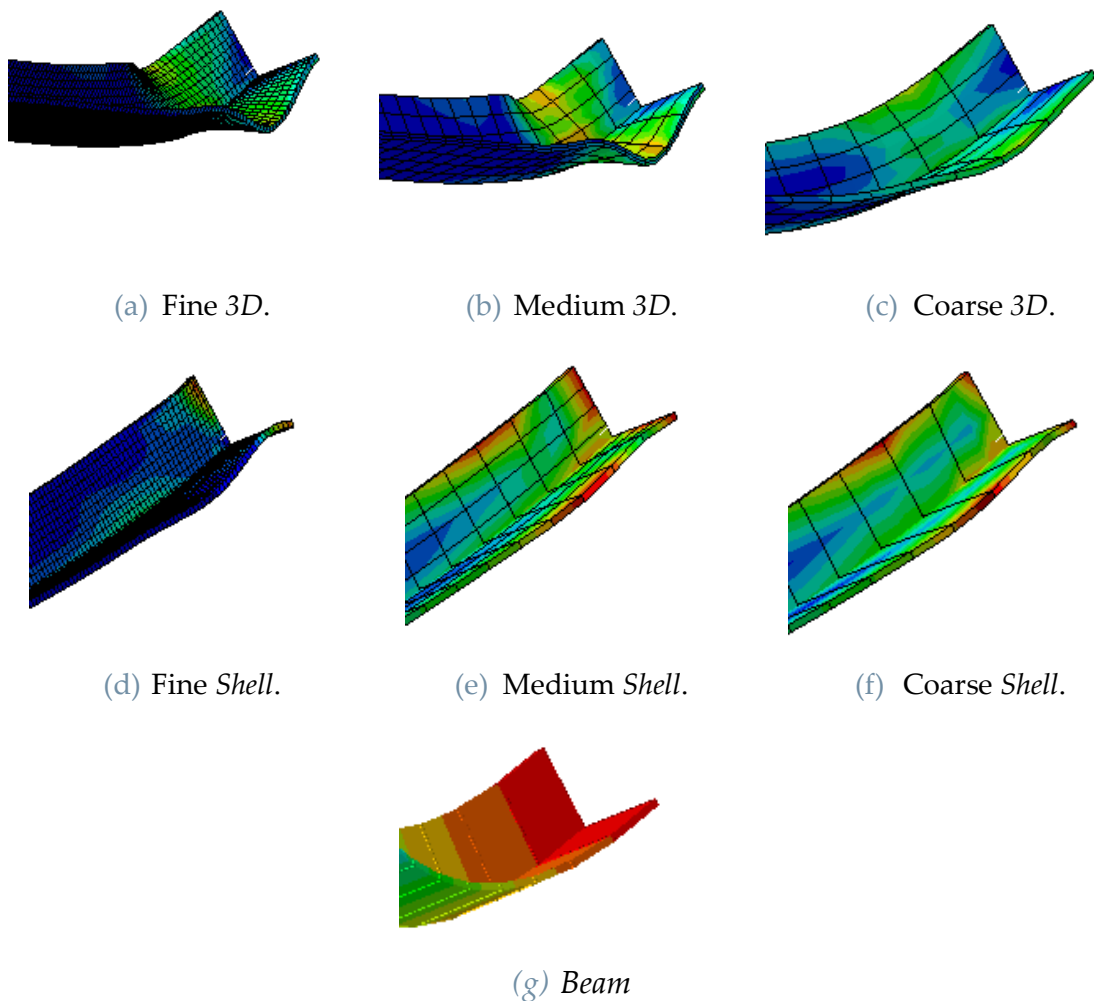(e) Medium *Shell*.

(f) Coarse *Shell*.

(g) Beam

Figure 1.29: Different local buckling shapes at different mesh sizes. Notice how the fine-meshed columns (a, b and d) are able to show a local buckling of the flanges.

As in the previous analysis, the *shell* element proved to be the stiffest, while the *1D* the softer. In addition, the difference between load capacities with different mesh size appears more pronounced than in the linear material case. The reason behind these two behaviors could be related to the local buckling happening on the flanges, close to the fixed end of the column, which develops differently depending on mesh and element type (Figure 1.29).

1.5. Conclusive discussion on the results

In the Chapter, the structural instability problem has been introduced and numerical methods have been developed aiming to improve simulation performances.

In conclusion, it has been possible to assess:

- Only with fine mesh *3D* or *Shell* elements, the local buckling is able to be properly displayed. *Shell* elements do not show local deformation, thus resulting in a more stiff deflection at midspan than the others types, whereas *3D* elements, by accurately simulating this behavior, have a slightly lower buckling load.

- *1D* elements do not show any sign of local effects, thus resulting in an overall softer element type and lower load to collapse.

- Only *Shell* and *3D* element types are able to display a sign of other buckling modes, such as *flexural-torsional*.

- As P. Uriz et al. [31] suggest, at least 3-4 elements per flange are necessary to simulate buckling reliably.

- A bi-linear model is enough to show the material nonlinearity effects and section yielding in the elastic and inelastic buckling areas.

- In general, if the *3D* elements are considered a good reference, it is possible to state that the *Eurocodes* underestimate the ultimate load. This is an intrinsic feature of a design standard, as it needs to assure safety rather than accuracy (visible in the comparison between the design limit and the tests on which these standards are based, Figure 1.30).

The element types better suited for a nonlinear *FE* buckling analysis of a large structure cannot however be *3D*, as they are very computationally expensive. *Shell* elements can be used in areas where a local effect is expected, while *1D* elements are to be used in areas of not primary importance as a way to reduce the computational cost.
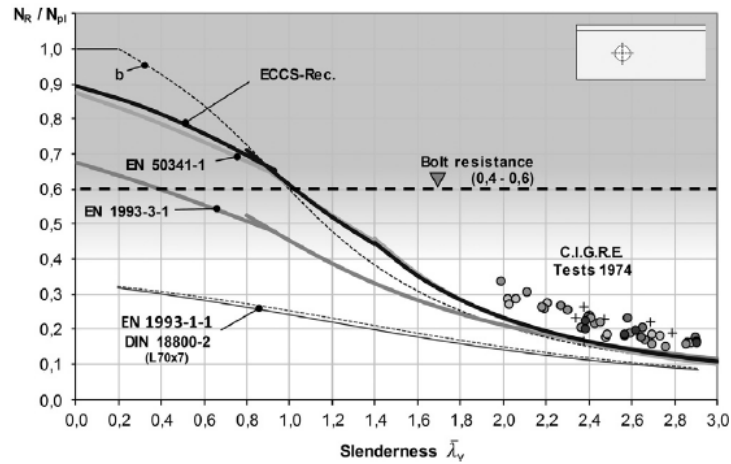
Figure 1.30: Example of buckling limits for single bolt end restrain (more about this in the following Chapters) according to different standards, compared to the 1974 C.I.G.R.E. test campaign [32].

Based on these grounds, in the next Chapters' investigations, the following mesh types are going to be used, when referring to a specific type of element:

- *3D Solid* - Quadratic Reduced Integration - 5 elements per flange width - 3 elements per thickness - 100 elements per member length (biased towards the edges). In detailed regions, such as the bolt position, the number of elements per width is going to be increased up to 20.

- *3D Shell* - Linear Reduced Integration - 6 elements per flange width - mid extrusion - 60 elements per member length (biased towards the edges).

- *1D Beam* - Linear - 40 elements per member length.

2   Chapter two: Validation of FE models

Design codes or analytical solutions are limited in their applicability, given the conservativeness purposes and the analytical models' limitations. Therefore, validation experiments are a necessary step to support a *FE* model accuracy. Moreover, in most experimental setups the end restrain condition is very simplified or the initial assumption to model imperfections is non-existent. Very conveniently, Kettler et al. [30, 32], have thoroughly treated the same issue in a complete and methodic approach to *FE* modeling of structural instabilities in slender columns.

In this Chapter, the experimental ([30]) and modeling ([32]) setup is described and two bolted columns with different end restrains are modeled and validated with experimental results.

2.1.   Experiments

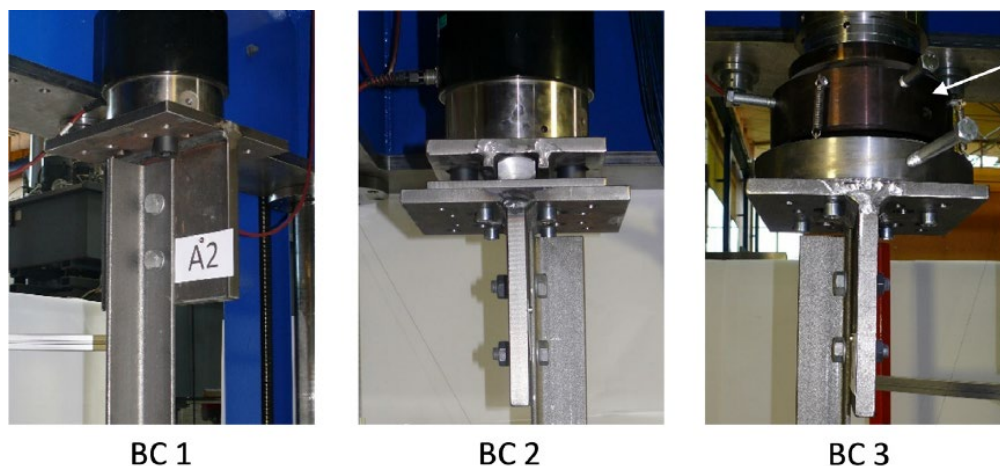The columns studied by Kettler are *angles* connected to a gusset plate on each end by one or two bolts.

Figure 2.1: *BC1*, *BC2 and BC3* from Kettler's experiments. In *BC2*, the end is connected by knife support (one free rotational degree of freedom), in *BC3* to a spherical joint, in order to have all rotational degrees of freedom free [30].

As it is shown in Figure 2.1, in their experiments they have applied three different types of end constraints to the gusset plates:

BC1: clamped support with all rotational degrees of freedom restraint at both member's ends;

BC2: a knife-edge support (centered in the axis of the gusset plate) that allows only for rotations about the axis parallel to the connected leg;

BC3: pinned support (centered in the axis of the gusset plate) with only the rotation about the longitudinal axis restraint.

The chosen experiment to replicate (A5 and C1, as marked in [30]), are both of section L80x8 mm, with different end-restrain and column length. The common section properties are reported in Table 2.1, based on Figure 2.2. The two braces have different lengths and end restrains, thus a new *"system length"* has to be introduced, between the two points of load application, and to be used for critical load estimation:

$$\text{A, BC2:} \qquad L_{sys} = L_{column} + 215mm \qquad (2.1a)$$

$$\text{B, BC1:} \qquad L_{sys} = L_{column} + 40mm \qquad (2.1b)$$

Moreover, they have also different geometrical and material properties, found by tensile testing, as highlighted in Table 2.2 and Figure 2.3.
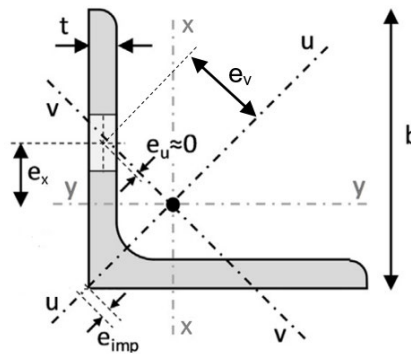

Figure 2.2: *Angle* section dimensions [30].

Property	I_{xx}	I_{yy}	I_{uu}	I_{vv}	e_y	e_x	e_v	e_U	b	t	A
Value	737298 mm^4	737298 mm^4	1173850 mm^4	300751 mm^4	18.95 mm	18.95 mm	26.79 mm	0 mm	80 mm	8 mm	1216 mm^2

Table 2.1: List of section L80x8 properties.

Note that in [30], the imperfection is only accounted in the *v-v* axis, when in reality it could be in any direction and make a large difference on the failure mode and result.

Experiment	Ref. in [30]	End restrain	Number of bolts	L_{member} [mm]	L_{sys} [mm]	e_{imp} [mm]	L_{sys}/e_{imp} [-]	E [MPa]	S_y [MPa]
A	**A5**	BC2	2	1550	1765	1.15	1535	212400	289.9
B	**C1**	BC1	1	3170	3210	1.10	2918	209300	333.9

Table 2.2: A and B experiments properties [30].

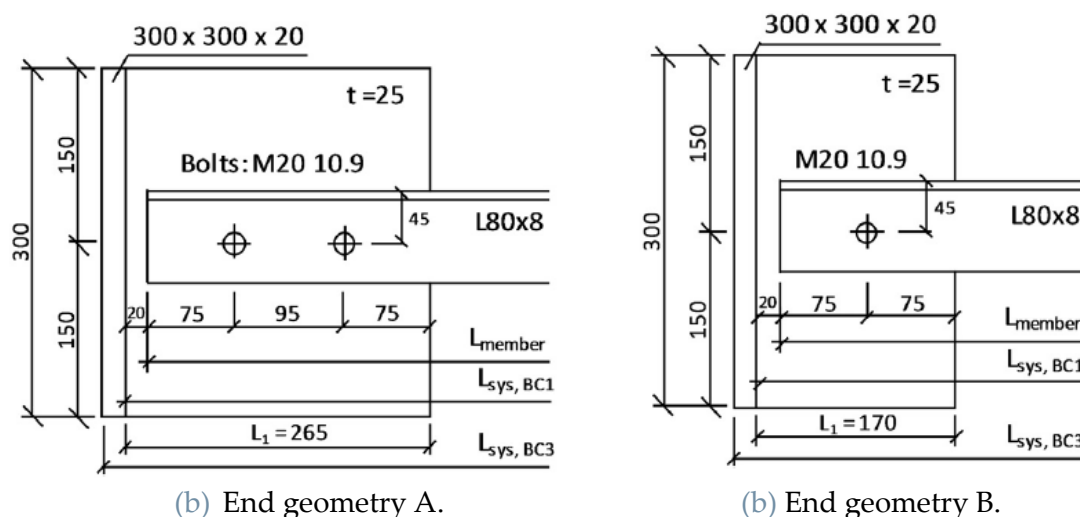(b) End geometry A.   (b) End geometry B.

Figure 2.3: End gusset geometry for the two experiments [30].

2.2.   Analytical solutions and applicable standards

With the purpose of having an additional reference, other two methods have been used in this case:

1- Analytical results from the *'Secant Formula"* [25] for eccentric loading, related to the before used *"Euler buckling" formulation* [24] (Section 1.2).

2- *Eurocode 1993-1.1* [29] code for lattice structures, taken without any safety factors.

3- *Eurocode 1993-3.1* [4] code for lattice tower members, taken without any safety factors.

2.2.1. Secant formula

The first approach is based, as *Euler's formula,* on the solution of the equilibrium equation of the *Pinned-Pinned* column with eccentricity. The same approach as in Section 1.2 was used, from the bending equilibrium at distance x is then given by the following equation:

$$M(x) = -F \cdot (\delta + e_0) \tag{2.2}$$

With $\delta(L) = 0$:

$$M(l) = -F \cdot e_0 \tag{2.3}$$

If we introduce the *Euler Beam* bending moment equation:

$$M(x) = E \cdot I \cdot \frac{\partial^2 \delta}{\partial l^2} \tag{2.4}$$

We finally get the following differential equation:

$$\frac{\partial^2 \delta}{\partial l^2} + K^2 \cdot \delta = -K^2 \cdot e_0 \tag{2.5}$$

with $K = \sqrt{\frac{F}{E \cdot I}}$. Its solution is of the type:

$$\delta(l) = C1 \cdot \sin(K \cdot l) + C2 \cdot \cos(K \cdot l) - e_0 \tag{2.6}$$

The constants $C1$, $C2$ in this equation can be found by applying the problem boundary conditions:

$$\begin{cases} \delta(0) = C1 \cdot 0 + C2 \cdot 1 - e_0 = 0, & \text{(2.7a)} \\ \delta(L) = C1 \cdot \sin(K \cdot L) + C2 \cdot \cos(K \cdot L) - e_0 = 0, & \text{(2.7b)} \\ \frac{\partial \delta}{\partial x}\left(\frac{L}{2}\right) = K \cdot C1 \cdot \cos\left(K \cdot \frac{L}{2}\right) - K \cdot C2 \cdot \sin\left(K \cdot \frac{L}{2}\right) = 0 & \text{(2.7c)} \end{cases}$$

From which the coefficients of the non-trivial solution $(v(x) \neq 0)$ can be derived:

$$\begin{cases} C1 = e_0 \cdot \tan\left(K \cdot \frac{L}{2}\right), & \text{(2.8a)} \\ C2 = e_0, & \text{(2.8b)} \\ K \cdot L = \pi & \text{(2.8c)} \end{cases}$$

The solutions of K from Equation 2.8c are $K \cdot \frac{L}{2} = n \cdot \frac{L}{\pi}$, valid for every integer $n > 0$.

The resulting deformed shapes are shown in Figure 2.4; all the first three modes have the highest deformation at midspan.
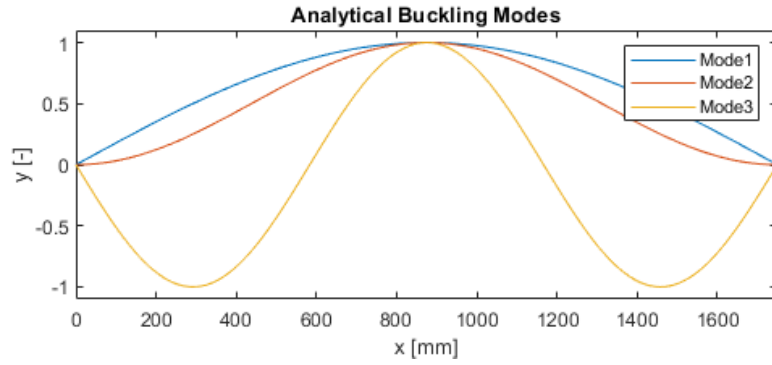
Figure 2.4: Analytical mode shapes, based on experiment B length.

The critical *Euler buckling load* is then found in Equation 2.9:

$$F_{cr} = \frac{\pi^2 \cdot E \cdot I}{L^2} \tag{2.9}$$

From the maximum deflection at midspan, the *Secant formula* can be then derived:

$$\begin{aligned}
\delta\left(\frac{L}{2}\right) &= e_0 \left(\frac{\sin^2\left(K \cdot \frac{L}{2}\right) + \cos^2\left(K \cdot \frac{L}{2}\right)}{\cos\left(K \cdot \frac{L}{2}\right)} - 1 \right) \\
&= e_0 \left(\sec\left(K \cdot \frac{L}{2}\right) - 1 \right)
\end{aligned} \tag{2.10}$$

$$M\left(\frac{L}{2}\right) = F \cdot e_0 + F \cdot \delta\left(\frac{L}{2}\right) = F \cdot e_0 \cdot \sec\left(K \cdot \frac{L}{2}\right) \tag{2.11}$$

If the maximum stress condition at midspan is then computed as follows:

$$\sigma_{max}\left(\frac{L}{2}\right) = \frac{F}{A} + \frac{M\left(\frac{L}{2}\right)}{W} = \frac{F}{A}\left(1 + \frac{A \cdot e_0 \cdot \sec\left(\frac{\pi}{2} \cdot \sqrt{\frac{F}{F_{cr,eul}}}\right)}{W} \right) \tag{2.12}$$

The solution is found by iterating on F, setting as a limit state the onset of yielding in the midspan section $\sigma_{max}\left(\frac{l}{2}\right) = S_y$.

It should be observed, however, that this result would be conservative for ductile materials that can easily withstand the full section plasticization.

The other limitation of this approach is that at the very beginning, a *Pinned-Pinned* ends column has to be considered, thus somewhat increasing the conservativeness for a more stiff joining, such as the two-bolt connection in A.

2.2.2. EC 1993-1.1

The *EC 1993-1.1, Annex BB* [29] for lattice structures modifies the slenderness ratio in the buckling directions, depending only on the end-constrains and neglecting the eccentricity.

If single bolt brace, the result is taken as the one from *EC 1993-1.1* for columns (used in Section 1.2), without any amendment.

If double bolted, the slenderness ratio has to be modified as follows:

$$\lambda_{eff} = 0.35 + 0.7 \cdot \lambda_n, \qquad in \ v - v \qquad\qquad (2.13a)$$
$$\lambda_{eff} = 0.5 + 0.7 \cdot \lambda_n, \qquad in \ x - x \ and \ y - y \qquad\qquad (2.13b)$$

The resulting limit values can be quantitatively appreciated in Table 2.3 and 2.4.

2.2.3. EC 1993-3.1

EC 1993-3.1, Annex G1 [4] is specifically for lattice towers members and, similarly to the previous code, adds a modification of the slenderness for secondary braces to the base *EC 1993-1.1* [29]. The element length is either the distance between the two inner bolts that connect it to other primary or secondary elements (Figure 2.5). In the current case, the system length is used instead (as it is the pivot position, in accordance to [30]).
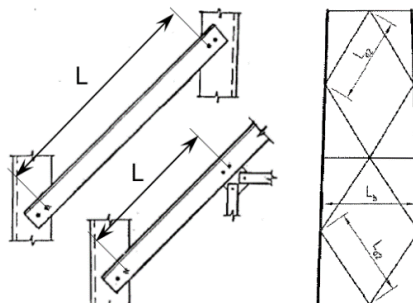

Figure 2.5: Buckling length, from *Table G2, EC 1993-3.1* [4].

If singe bolt brace, the slenderness ratio has to be modified as follows:

$$\lambda_{eff} = 0.35 + 0.7 \cdot \lambda_n, \qquad in \ v - v \tag{2.14a}$$
$$\lambda_{eff} = 0.58 + 0.7 \cdot \lambda_n, \qquad in \ x - x \ and \ y - y \tag{2.14b}$$

If instead double bolted, the slenderness ratio has to be amended as follows:

$$\lambda_{eff} = 0.35 + 0.7 \cdot \lambda_n, \qquad in \ v - v \tag{2.15a}$$
$$\lambda_{eff} = 0.4 + 0.7 \cdot \lambda_n, \qquad in \ x - x \ and \ y - y \tag{2.15b}$$

The resulting limit values can be quantitatively appreciated in Table 2.3 and 2.4.

2.2.4. Graphical display of load limits

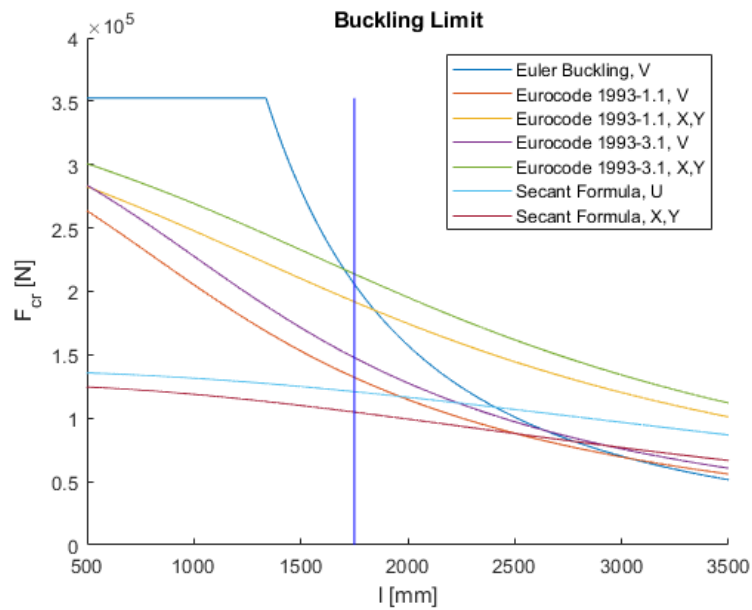The ultimate loads according to analytical formulas and standards are summarized in Table 2.3 and 2.4.
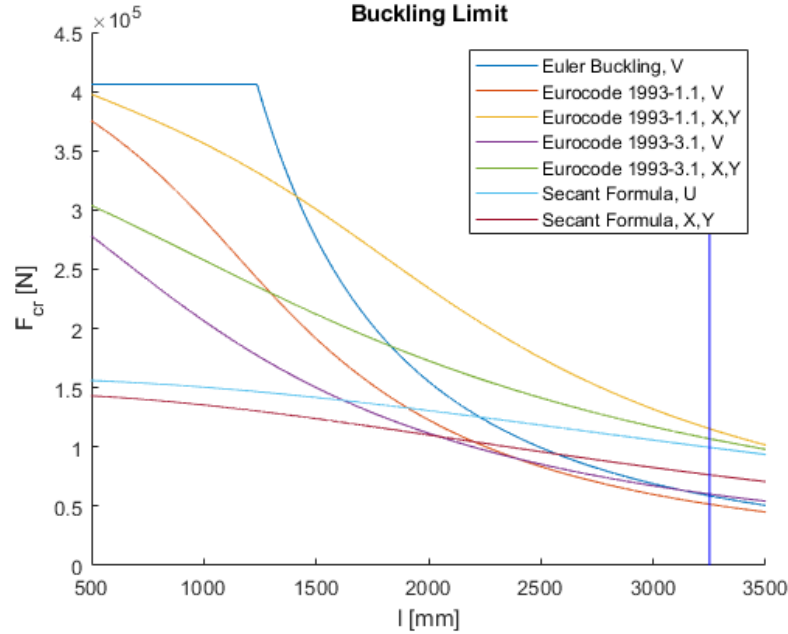

Figure 2.6: Critical load in different flexural buckling axis, according to analytical solutions and standards, experiment A

Mode	Fcr in x-x, y-y [kN]	Fcr in u-u [kN]	Fcr in v-v [kN]
Euler	494.2	786.8	201.6
Secant	104.8	120.9	201.6
EC 1993-1.1	191.8	-	132.2
EC 1993-3.1	213.8	-	147.7

Table 2.3: Critical buckling loads for every bending axis, based on column A.

Figure 2.7: Critical load in different flexural buckling axis, according to analytical solutions and standards, experiment B.

Mode	Fcr in x-x, y-y [kN]	Fcr in u-u [kN]	Fcr in v-v [kN]
Euler	146.8	233.8	59.9
Secant	76.5	99.6	59.9
EC 1993-1.1	115.4	-	51.7
EC 1993-3.1	106.9	-	60.2

Table 2.4: Critical buckling loads for every bending axis, based on column B.

Note that experiment A is within the inelastic region, while B is in the elastic region in almost every considered axis (reference Figure 1.7).

The lowest limit estimations appear to be the one from the *Secant Formula* in *x-x* or *y-y* axis, and the *EC 1993-1.1* [29] and *EC 1993-3.1* in the secondary axis (*v-v*).

2.3. FE Model

The *FE* analysis was carried out using a static displacement controlled procedure, since the slow displacement rate of the experiment should not introduce dynamic effects on the structure and, as it has been proved in the last Section, an angle's buckling curve is of the monotonic kind.

To match the experimental data, and to have a more clear and complete picture of sensitivity to variables, different models with different imperfection magnitude and direction, friction coefficient and/or bolt class have been analyzed.

As for gusset plate properties, a simple linear elastic material model, with E=210000 MPa, has been adopted as in [32], since the plate thickness (and overall size) is much larger than the angle and thus expected to experience very little deformation in the process (remaining in elastic regime).

The bolts are also taken as linear elastic with E=210000 MPa, as in [32]. The bolt connection is designed according to *Eurocode 1993-1.8* [33], with a bolt M20 class 10.9 (R_m=1000 MPa, S_y=900 MPa) and a bolt pre-tensioning factor γ_{M7}=1:

$$N_{Pretensioning} = 0.7 \cdot \frac{R_m \cdot A_S}{\gamma_{M7}} = 201600 \ N \qquad (2.16)$$

A_S is taken as the nominal bolt area with a diameter of 20mm.

The friction coefficient is taken as in the *FE* model in [32], as a simple penalty factor f=0.25.

Note that according to *buckling curve b, Table 5.1, EC 1993-1.1* [29], a standards imperfection magnitude is e_0=L/250 for elastic analysis e_0=L/200 for plastic analysis. Y. M. Darestani et al. [17] and P.Uriz et al. [31] use a simple sinusoidal imperfection (maximum displacement at the center of the element) of 0.05-0.1% the length (e_0=L/500 to e_0=L/1000). J. Wang et al. [18] employed the *Eigenmode Assembly Method (EAM)* based on the superimposition of multiple imperfection modes obtained from a *Linear Buckling Analysis (LBA)*.

The following models have been used for experiment A:

- *Standard e_0=L/300, f=0.25:* with all the variables as in [32];
- *Reduced imperfections e_0=L/1350, f=0.25;*
- *Reduced imperfections, 5.6 class bolt e_0=L/1350, f=0.25;*

And for experiment B:

- *Standard e_0=L/300, f=0.25:* as in [32];
- *Reduced imperfections e_0=L/1350, f=0.25;*
- *Multiple mode imperfections (EAM [5]) and increased friction e_0=L/400, f=0.4;*

2.3.1. Results for case A

Despite lower axial stiffness (in Z, Figure 2.8), the deflection in the failure direction Y (Figure 2.9) perfectly matches both the experimental and numerical results ([30, 32]), a sign that all the models undergo the same failure mode.
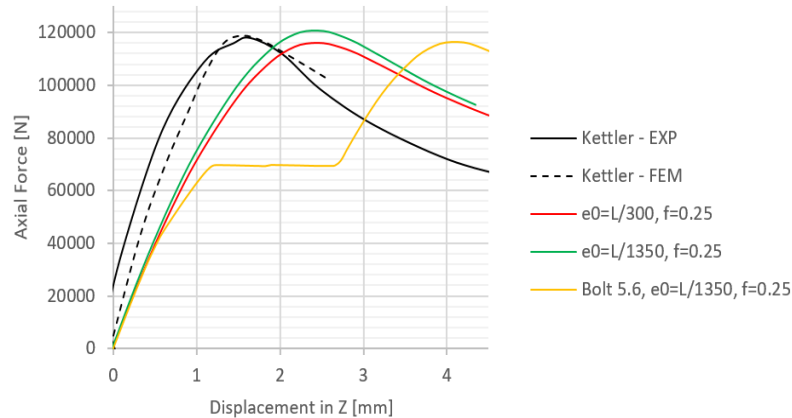

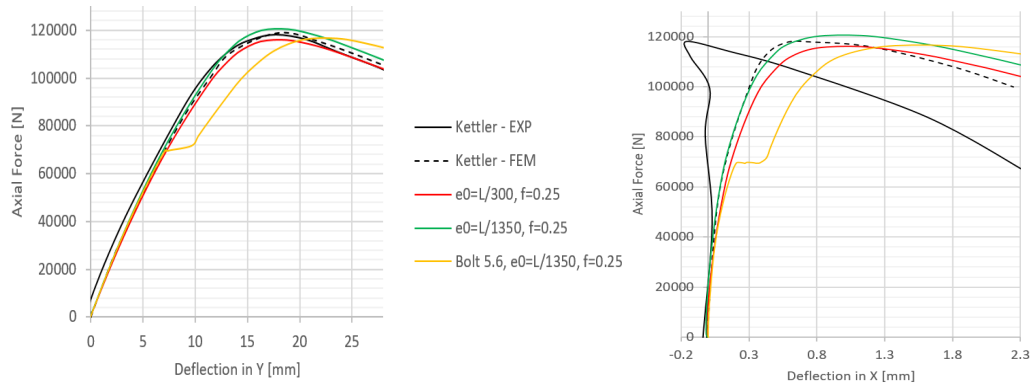Figure 2.8: Force – axial displacement (Z) curves for model A [30, 32].

Figure 2.9: Axial force – midspan deflection curves (in Y and X) for model A [30, 32].

The models proved to be fairly accurate in the ultimate load estimation, as reported in Table 2.5. The connection slip barely affects the ultimate load of the column and the initial stiffness, but only the displacement at failure.

	Kettler EXP	Kettler FEM	e_0=L/1350, f=0.25	e_0=L/300, f=0.25	Bolt 5.6, e_0=L/1350, f=0.25
Load capacity [kN]	**118.0**	119.0	120.6	116.0	116.5
Err. [%]	-	0.8%	2.3%	-1.6%	-1.2%

Table 2.5: Load comparison with the experimental value.

A qualitative comparison with the failure mode of the real experiment is displayed in Figure 2.10. It is possible to notice how almost the entirety of the section is also

undergoing yielding upon buckling: there is an correlation between the two
phenomena that reduces the load-bearing capacity as the length is within the
inelastic buckling region.

(a) *FEM A, deformation scale 2.*
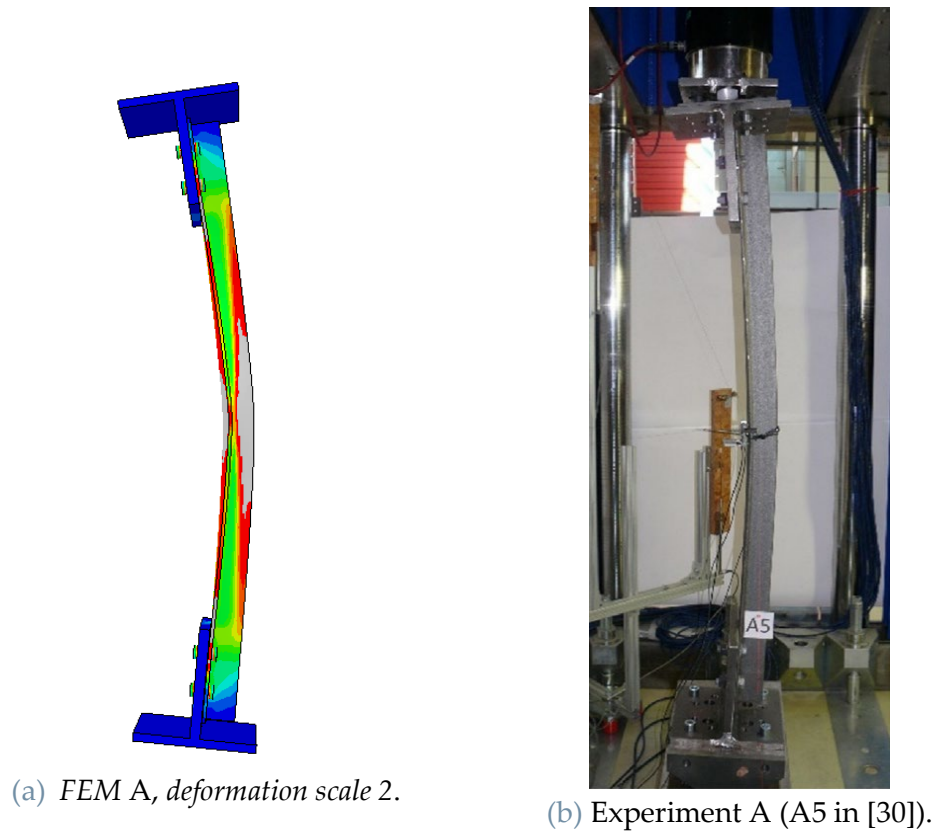
(b) Experiment A (A5 in [30]).
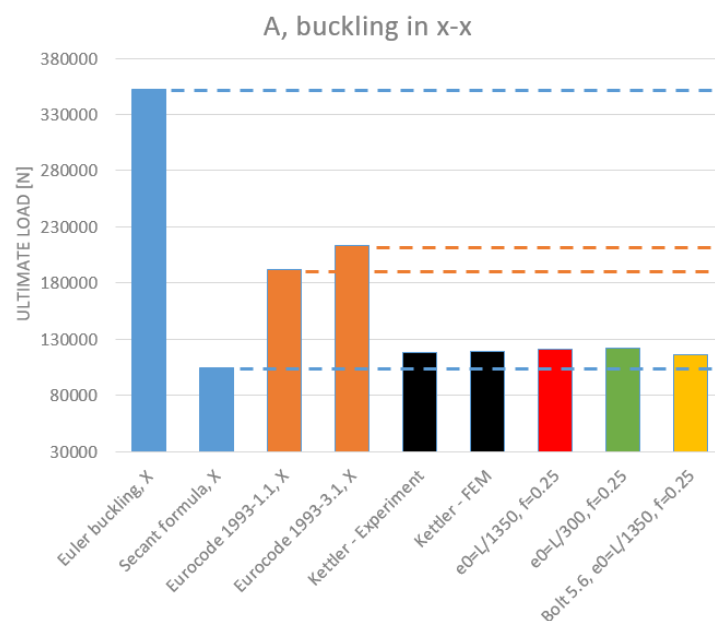
Figure 2.10: Comparison with the real counterpart.

Figure 2.11: Load capacity of every model, analytical solutions and standards.

The results are then compared with the analytical and standards for buckling in *x-x* in Figure 2.11: the codes greatly overestimate this specific case, while the secant formula provides a more accurate description. The load eccentricity, perhaps, plays a more important role than the end restrain condition, if the collapse degree of freedom is left free to rotate, while the standards consider the brace closer to completely restrained in all directions.
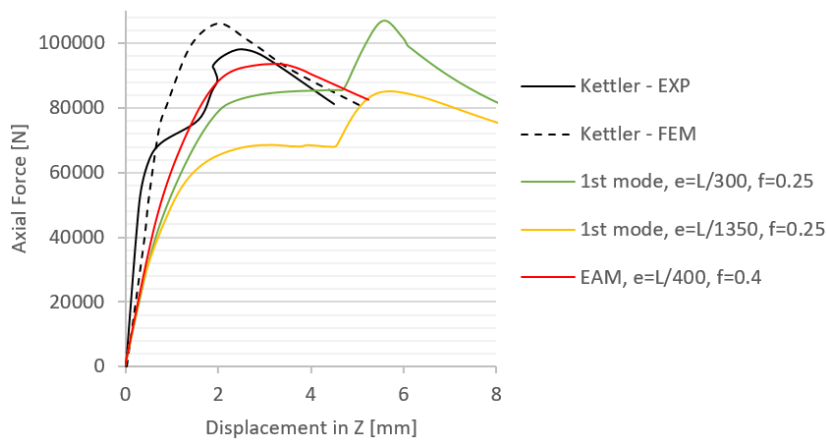
2.3.2. Results for case B

Figure 2.12: Force – axial displacement (Z) curves for model B [30, 32].
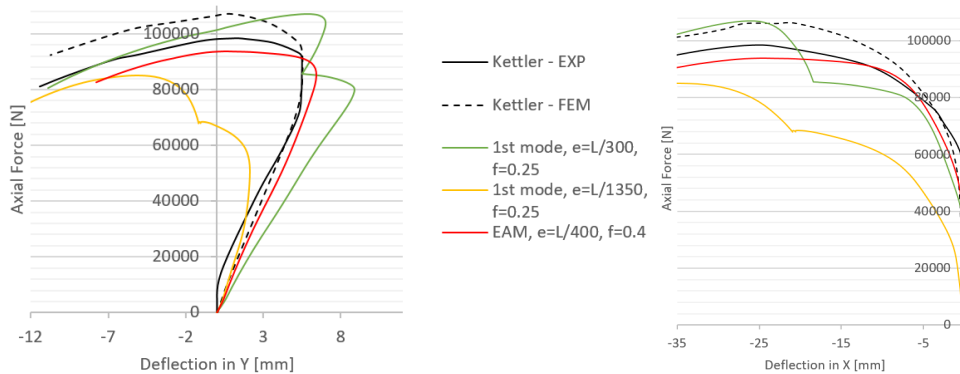

Figure 2.13: Axial force – midspan deflection curves (in Y and X) for model B [30, 32].

As in model A, the numerical results show lower axial stiffness in Z (Figure 2.12), but the deflection in the failure direction in X is well matched (Figure 2.13), with all the models undergoing the same failure mode. Even with the 10.9 bolt, the single bolt connection slips with friction coefficient *f*=0.25. Only the model with increased friction (and *EAM*) does not display the behavior, thus better reproducing the experiment.

The models showed a large scatter in the ultimate load estimation, largely dependent on the type and magnitude of imperfections and friction, as reported in

Table 2.6. The lower initial imperfection gives the higher ultimate load in this specific case. This is due to the fact that the superimposed buckling mode is in the opposite direction to the actual failure.

	Kettler EXP	Kettler FEM	e_0=L/300, f=0.25	e_0=L/1350, f=0.25	EAM, e_0=L/400, f=0.4
Load Capacity [kN]	98.5	107.0	106.9	85.0	93.7
Relative Err. [%]	-	8.6%	8.6%	-13.7%	-4.8%

Table 2.6: Load capacity comparison with the experimental value.

(b) *FEM* B, deformation factor 2.

(b) Experiment B (C1 in [30]).
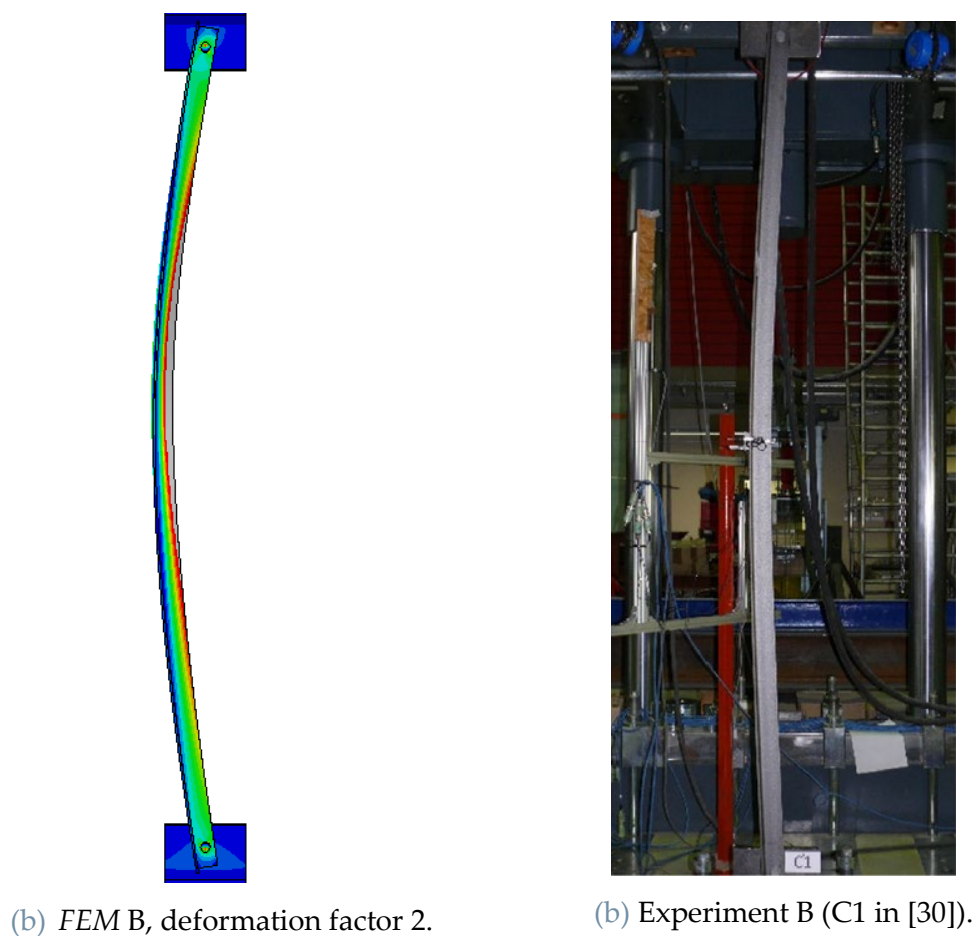
Figure 2.14: Comparison with the real counterpart.

In Figure 2.14, a qualitative comparison of the failure mode with the real counterpart: being in the elastic buckling area (Figure 1.7), the column does not undergo complete section plasticization at peak load (not even afterwards).

The results are then compared with the analytical and standards for buckling in *y-y*, in Figure 2.15. Overall, the results are better represented by the *Eurocodes*,

probably because the case more closely resembles the *Pinned-Pinned column,* upon which those standards are based.
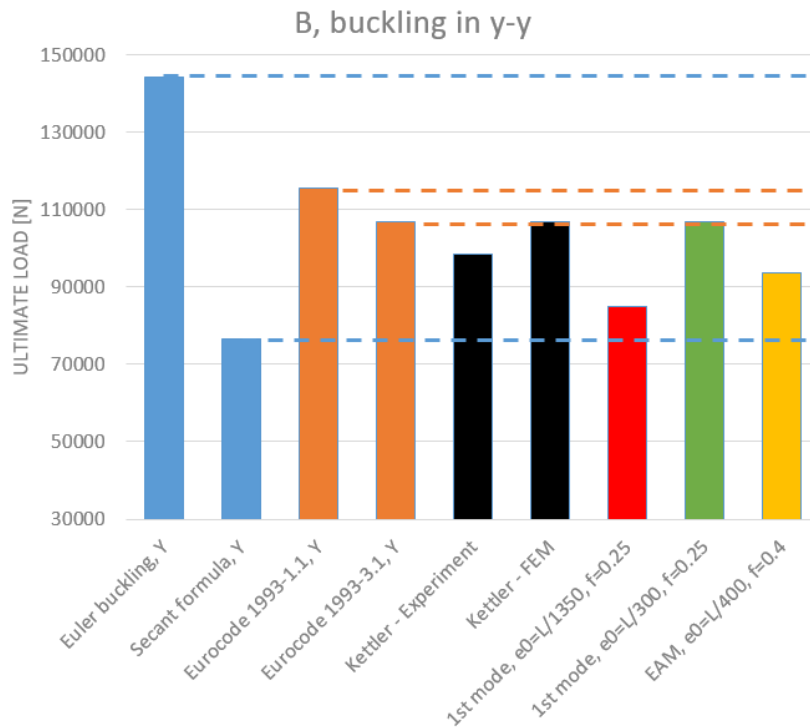

Figure 2.15: Load capacity for every model, analytical solutions and standards.

2.4.   Conclusive discussion on the results

The validation procedure aimed to verify that the *FE* methods and the modeling approaches studied so far can be employed to accurately describe a real phenomena.

Either of the analyzed models can achieve a good estimation (within 3%) in the ultimate load capacity for A, whereas for B only the *EAM* model achieved within 5% accuracy. However, depending on which buckling imperfection mode is applied, the models show a large scatter in the ultimate load and displacement at collapse (around 3.9% difference in experiment A, 22.3% in B). This could be attributed to the clearances and assembly misalignments present within the real systems and not accounted in the *FE* model.

The single mode superposition seem to be too restrictive in terms of buckling direction (as in B, it could be a "false" mode and the element would otherwise take a different path). The *EAM* method in [18] can be a more equilibrated approach.

Furthermore, by simplifying the contact problem with a penalty friction coefficient (without displacement rate dependent effects) it might be possible to miss time

dependent effects that happen if the collapse is sudden (such is the nature of the instability).

The analyzed standards for ultimate buckling load do not estimate effectively the ultimate load. The complexity of the end-restrain conditions is not trivial and cannot be portrayed by simplified formulas and assumptions. This is also in line to what Kettler et al. [30] have found similar results in their tests (Figure 2.16) and there is the need of a more accurate or less "conservative" design standard.
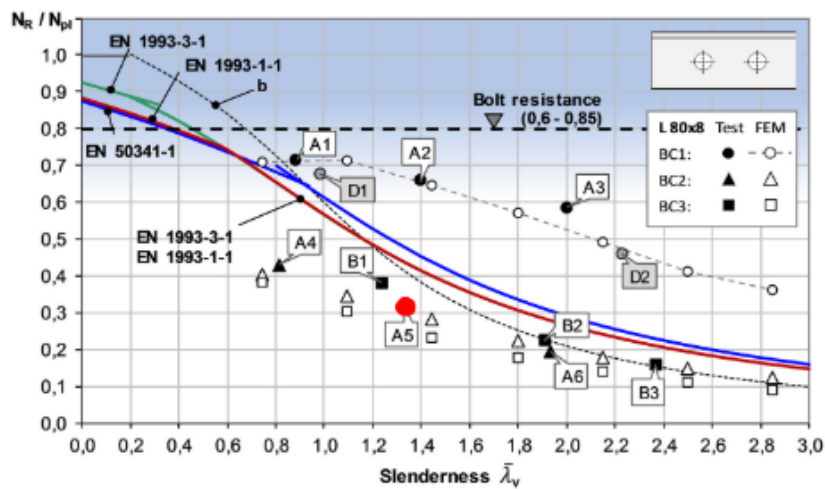

Figure 2.16: Normalized member capacity – slenderness ratio for two-bolt connection experiments, compared to current standards [30]. Marked in red, the experiment A (A5 as in [30]).

3 Chapter three: Boundary conditions modeling

Modelling a whole lattice tower as a full *3D* assembly would be also time consuming and computationally unfeasible: a simpler and more effective approach is required.

As seen in Chapters 1 and 2, the buckling modes and critical loads are highly dependent on the boundary conditions of the analyzed elements. In a lattice structure, the members are connected among each other, thus the load sharing and the flexibility of the joints is of extreme importance.

The topic of modeling joints and restrains is not new: Y. M. Darestani et al. [17] analyzed the impact of nonlinear material, geometry, imperfections and joint flexibility; W. Q. Jiang et al. [34] used stiffness functions to describe joint behavior in a lattice structure.

Relying on a single stiffness coefficient would not make for an accurate description of the slip phenomena after the friction limit is reached and the progressive shearing of the bolt shanks after the gap is cleared. A more complex modeling technique was first proposed by Ungkurapinan et al. [35], introducing a *"joint slippage model"* consisting of a series of linear stiffness coefficients, depending on the specific case.
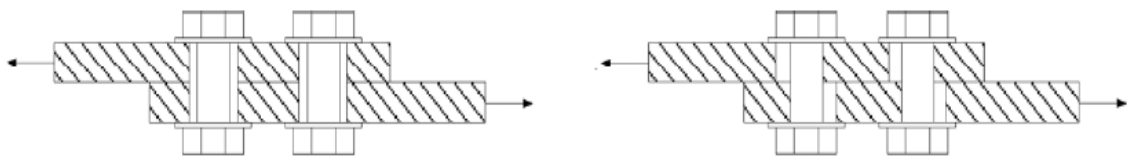

Figure 3.1: Bolted connection between bolted laps, slipping under tension [34].

Kettler et al. [36] offers a solution to this problem, by introducing a handy and user-friendly 3-steps method to obtain end restrain stiffness, based on the experimental results in [30], with the ultimate goal of introducing it as a variable to be accounted for in the member design procedure.

In the Chapter, *Kettler's* approach has been reviewed and some joint modeling options are tested and validated on the experimental results from [30].

3.1. Kettler's approach to joint modeling

The approach is based on three main steps:

Step 1) Calibration of the *FE* model with equivalent geometric imperfections on experimental tests from literature or on additional tests.

Step 2) Development of spring stiffness functions based on *FE* numerical results: the end restrain of the brace is loaded in each direction, recording the load – displacement curve. Only the gusset plate and the bolts are linear elastic, the column end is set as rigid, as the bending stiffness of the beam is already part of the following model.

Step 3) Validation of the design model by comparison with experimental tests and with an additional *FE* study on *3D*-angle members with detailed joint configuration.
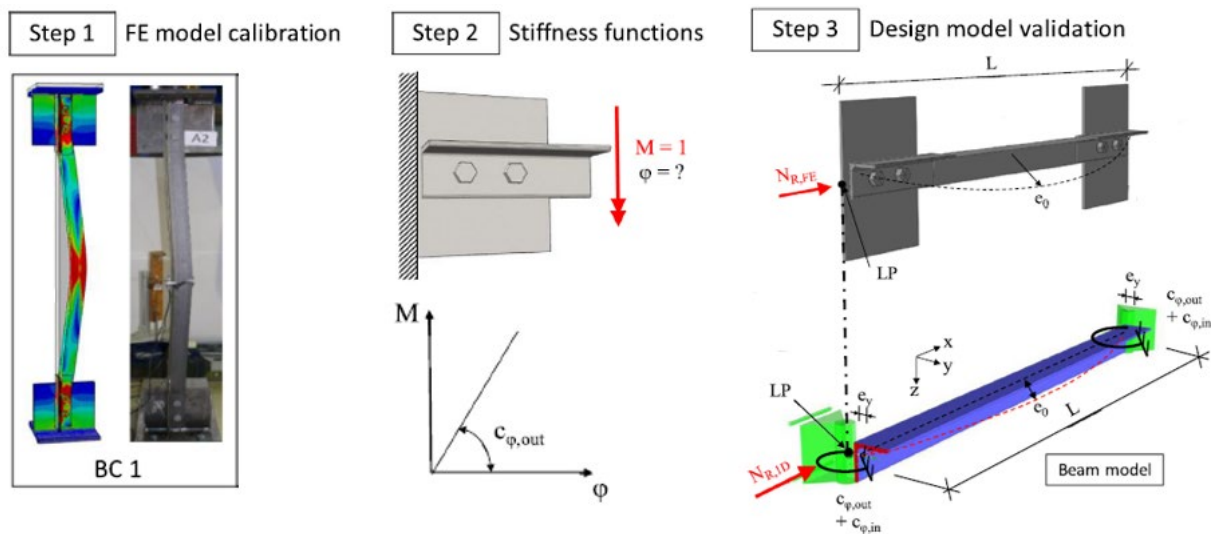
Figure 3.2: The three steps from Kettler's procedure, schematized [36].

Note that the purpose of *Kettler's* approach, is to outline new design rules for braced components: as it could be seen in the past sections, the present *Eurocodes* do not show great accuracy in forecasting of the load capacity for braced columns, even leading to overestimation. Understandably, a more detailed description is needed and it might find its roots in [36].

3.2. FE Model

The first calibration step was carried out in the previous Chapter 2 experiments A and B, thus the *FE* models used refer to Section 2.3. All the following *FE* analysis, as before, were carried out using a static displacement controlled procedure, as the Load - displacement curve is of the monotonic kind (Figure 2.8 and Figure 2.12).

The reference model to be matched was taken as the previous full *3D* simulation "*Standard e_0=L/300, f=0.25*", for two main reasons:

- it has same input parameters as [32] and has fairly close results to both experimental and *FE* results [30, 32];

- It showed the slip at the bolted connections, thus more compelling from a "*demonstrator*" standpoint.

To match the reference data, and to have a clearer and complete picture on some variables sensitivity, several models with different imperfection magnitude have been analyzed.

3.2.1. Modeling of stiffness functions
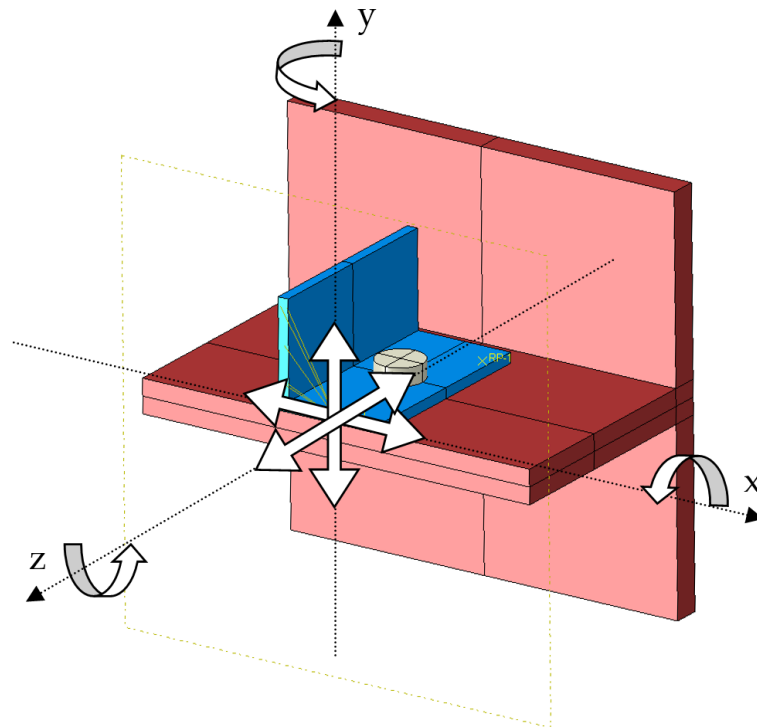
Figure 3.3: End model loading.

The end stiffness functions have been retrieved from a full *3D* model of the latter, but differently to the presented *Step 2*, deformable parts with elastoplastic material

characterization have been subjected to loading in every direction, from the column side, with the end of the gusset plate fixed in place (thus characterizing the whole system stiffness).

As an example (as it is a straightforward representation), the resulting stiffness function for the case of tension and compression along Z axis, in experiment B (single-bolt restrain), is reported in Figure 3.4. It is possible to notice the bolt slippage and the full section yielding.

All the directions shown in Figure 3.3 have been characterized in a similar manner.
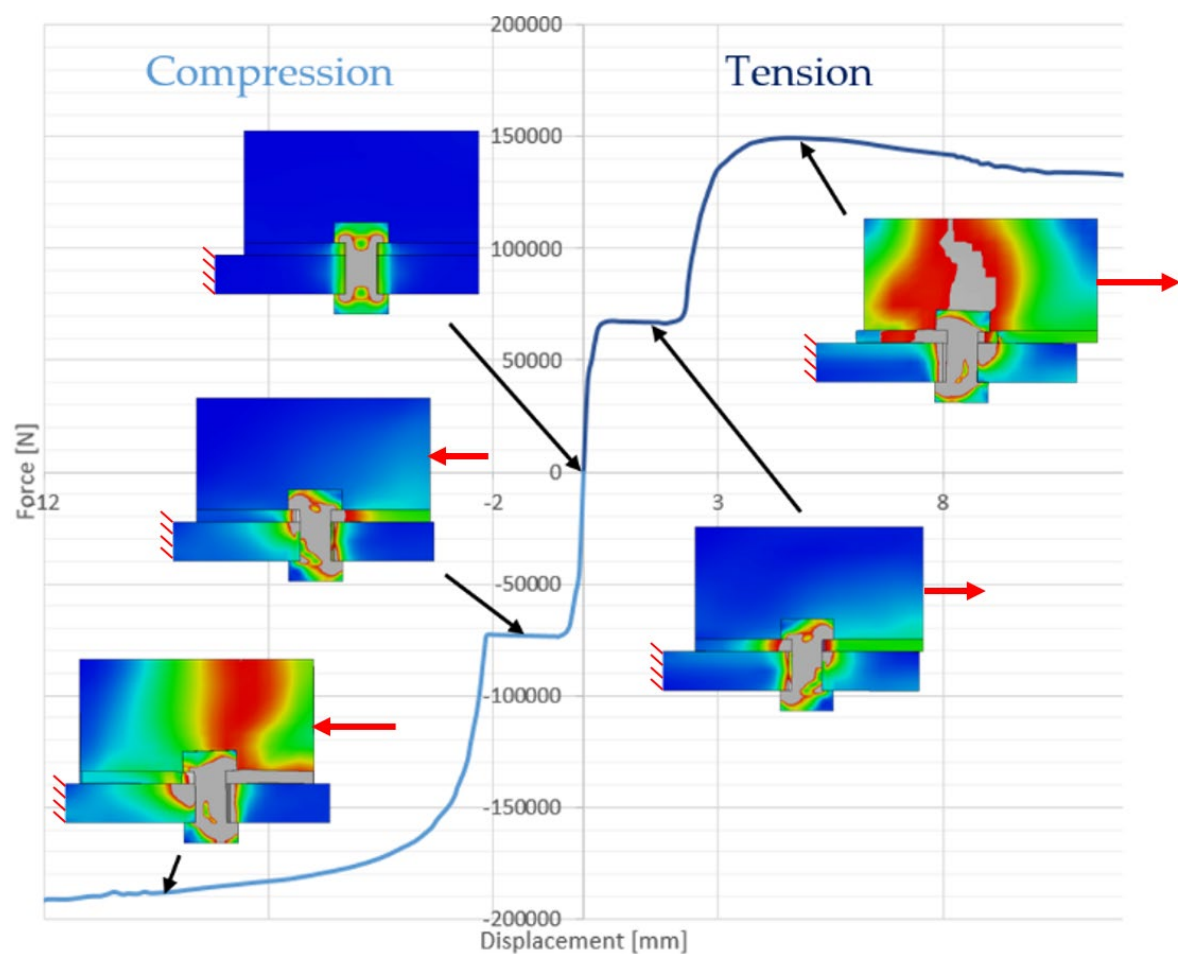
Figure 3.4: Stiffness functions for tension and compression in Z, experiment B.

The resulting functions have been employed in a connector model that simulates what happens at the beam-ends, in the following ways:

- *Linear*: by using the linear stiffness coefficients, using *Shell* element type;
- *Nonlinear*: by using the complete force-displacement curve/stiffness function (as in Figure 3.4), with either *3D*, *Shell* or *Beam* element types.

- *Rigid*: completely compliant joint (fixed) in A, with only a rotational degree of freedom in Y in B (able to pivot around the bolt axis), using *Shell* elements.

Note that, differently to Kettler's, in which the beam is then extended to the points of force application, the column is cut at the joint end and the part in contact with the gusset is completely simulated by the stiffness function.
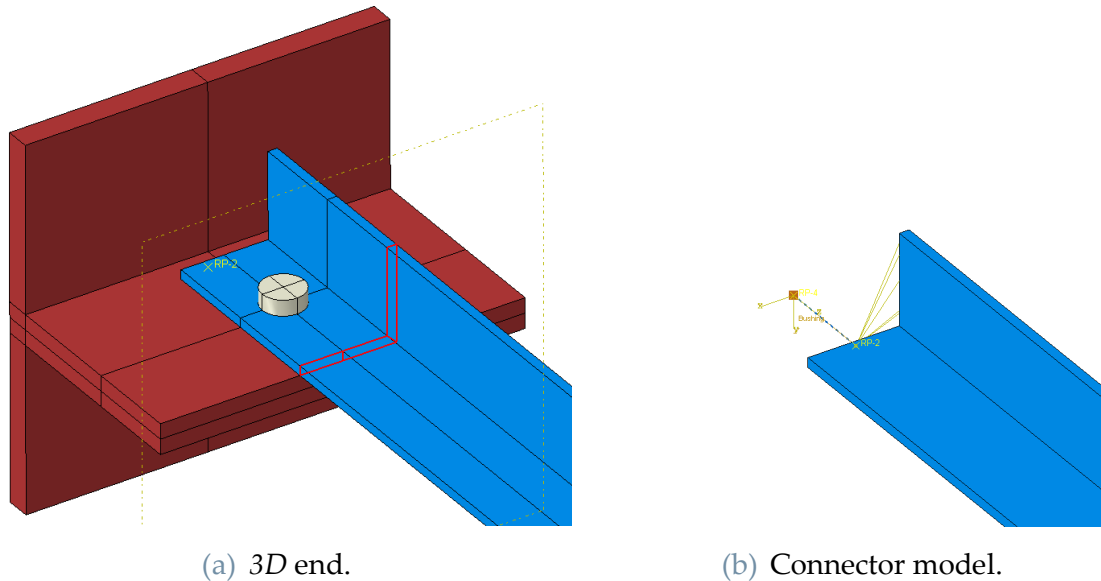

(a) *3D* end.   (b) Connector model.

Figure 3.5: *3D* end and connector modeling.

There are three main limitations to this approach:

- local deformations close to the joint are misrepresented: the section surface at the cut is planar and compliant to the loading node, thus losing any possibility of deforming in both the joint model and the beam with connector (however, it could be improved by increasing the offset from the bolt);
- multiaxial loading that cannot be properly represented by mere uniaxial stiffness functions, especially when friction plays an important role;
- no time-dependent effect, such as dynamic friction or damping, can be modeled, as there is no possibility of knowing the displacement or load rates beforehand.

3.2.2. EC 1993-1.8 for joint modeling

The classification of joints as pinned, rigid or semi-rigid is addressed between *Section 5, EC 1993-1.8* of the above-mentioned standard [33] and could hint at the correct way to model them.

According to the standard, the classification depends on the initial stiffness:

- *Rigid:*

$$K_0 > 25 \cdot \frac{E \cdot I_v}{L} \tag{3.1}$$

- *Pinned:*

$$K_0 < 0.5 \cdot \frac{E \cdot I_v}{L} \tag{3.2}$$

- *Semirigid:* if it does not fit these two classes.

The initial joint stiffness and the limit is reported in Figure 3.6 (in kN/rad).

Joint stiffness classification

	A, Km,x	A, Km,y	B, Km,x	B, Km,y
▲ Rigid limit	90736	90736	49572	49572
■ Pinned limit	18147	18147	9914	9914
● Model stiffness	110205	58270	91743	29135

Figure 3.6: Limits according to *EC 1993-1.8* [33].
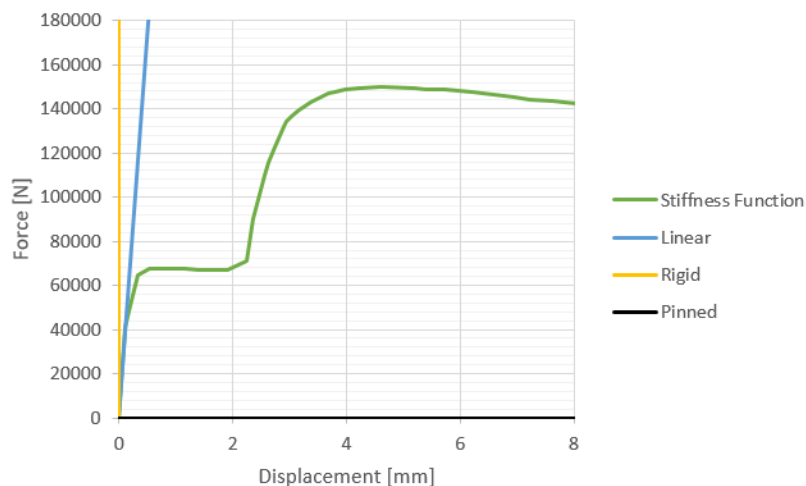
Figure 3.7: Connection force – displacement curve according to different modeling strategies.

The stiffness in X is over the rigid limit, thus the modeling as fixed can be an option. In plane (in Y), the two joints are clearly semi-rigid.

The standard, however, compares the two stiffness coefficients only with the lowest bending stiffness of the member, ignoring the possibility that considering the stiffness along other axes, the classifications could differ. As an example, considering the moment of inertia along x or y, both would fall into the semi-rigid category in X and be close to pinned in Y (Figure 3.8).
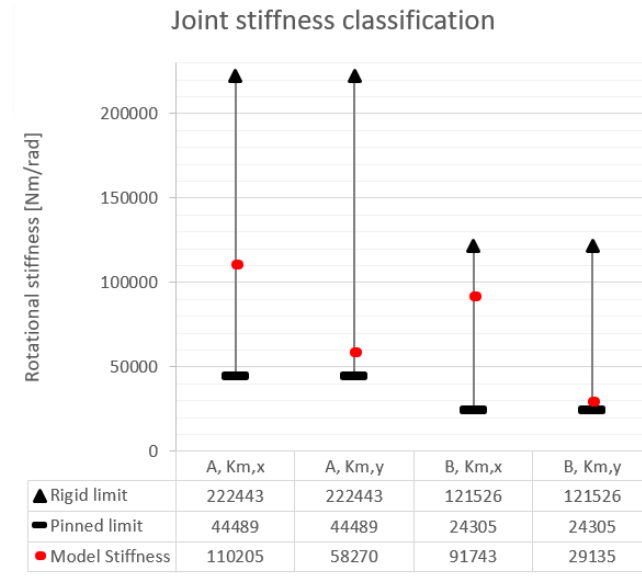
Figure 3.8: Limits according to *EC 1993-1.8*, but considering the corresponding rotational axis.

3.2.3. Results for A

The displacement in Z (Figure 3.9) and the deflection in Y are perfectly matched (Figure 3.10), but in X most of the models show larger deviation. They are undergoing an intermediate mode between *x-x* and *v-v*, probably due to lower rotational stiffness in Z, as this does not happen in the completely rigid model, which has almost the failure mode as the *3D* model and the experiment.
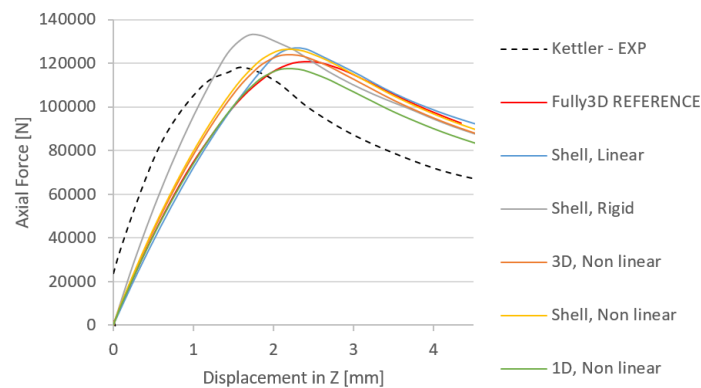
Figure 3.9: Force – axial displacement (Z) curves for model A [30, 32].
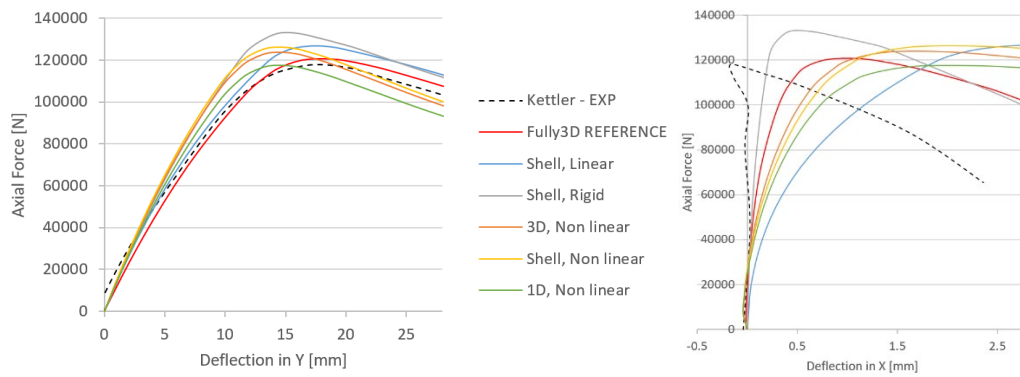
Figure 3.10: Axial force – midspan deflection curves (in Y and X) for model A [30, 32].

Almost all the models have proven to be accurate in the ultimate load estimation, as reported in Table 3.1, the *Shell* elements show around a 5% to 10% overestimation with respect to the reference. *Rigid* and *Linear* models are able to represent the behavior almost as close as the others, probably due to the lack of slippage in the experiment.

	Fully3D REF.	Shell, Rigid joint	Shell, Linear joint	3D, Nonlinear	Shell, Nonlinear	1D, Nonlinear
Load Capacity [kN]	120.7	133.1	126.9	123.8	126.3	117.6
Relative Err. [%]	-	10.5%	5.3%	2.7%	4.8%	-2.6%

Table 3.1: Load capacity comparison with the 3D reference.

(a) *FEM A – With end connector model, deformation scale 2.*

(b) *FEM A, deformation scale 2.*

(c) Experiment A (A5 in [30]).
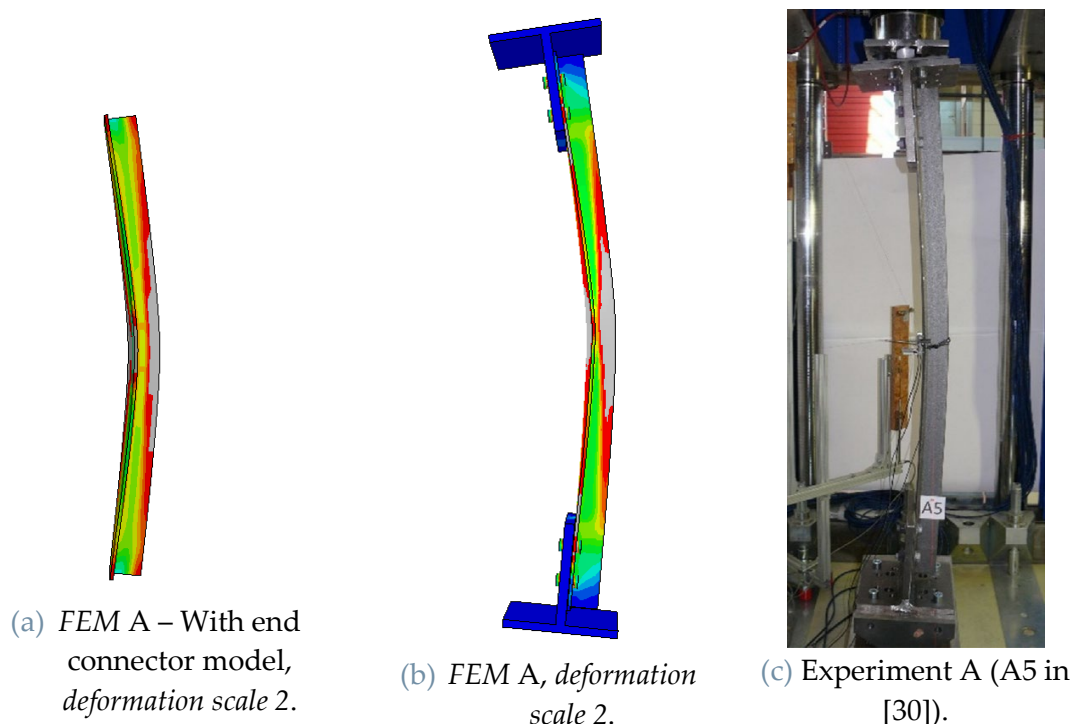
Figure 3.11: Comparison with the *3D FE* reference and the real counterpart.

3.2.4. Results for B

The load-displacement curves correctly show the slippage of the joints in axial direction (Figure 3.12), but not in the transversal (Figure 3.13). The deformation at ultimate load is identical in each direction, the failure mode is similar to the reference and the real counterpart, showing at least a fair level of accuracy.
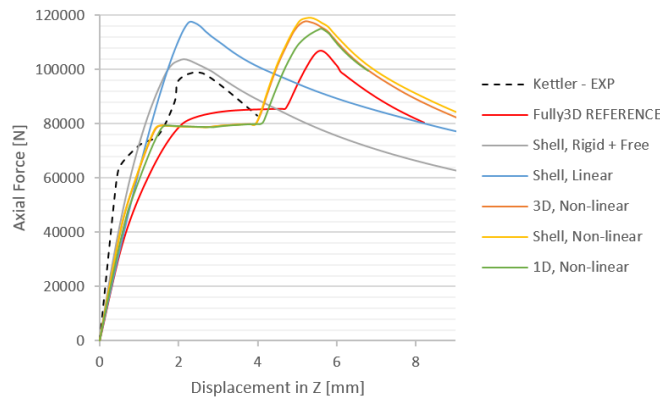

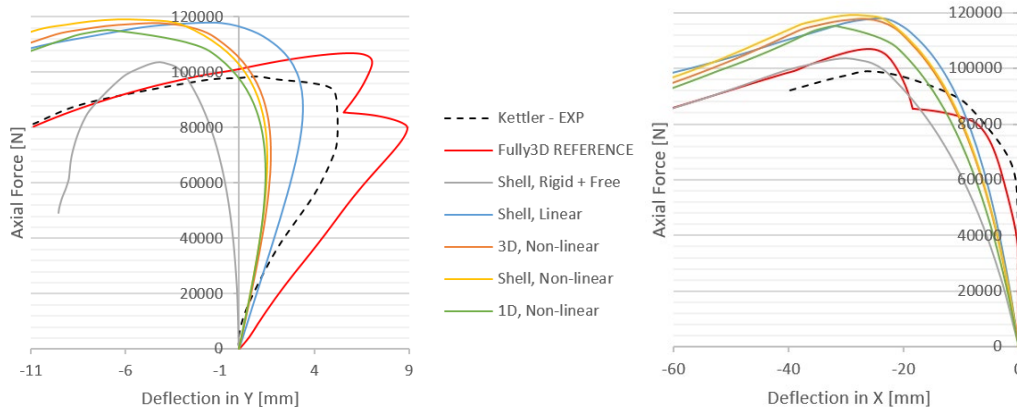Figure 3.12: Force – axial displacement (Z) curves for model B [30, 32].

Figure 3.13: Axial force – midspan deflection curves (in Y and X) for model B [30, 32].

Compared to the reference (Table 3.2), the ultimate load is overestimated by a factor of around 10%. The dissimilarity is probably due to a combination of large end-displacements in multiaxial direction that cannot be well expressed by simple uniaxial stiffness functions.

	Fully3D REF.	Shell, Rigid+Free	Shell, Linear	3D, Nonlinear	Shell, Nonlinear	1D, Nonlinear
Load Capacity [kN]	106.9	103.7	117.6	117.8	119.2	115.1
Relative Err. [%]	-	-3.0%	10.0%	10.2%	11.5%	7.7%

Table 3.2: Load capacity comparison with the reference.

A qualitative comparison of the failure mode with the real experiment can be found in Figure 3.14.
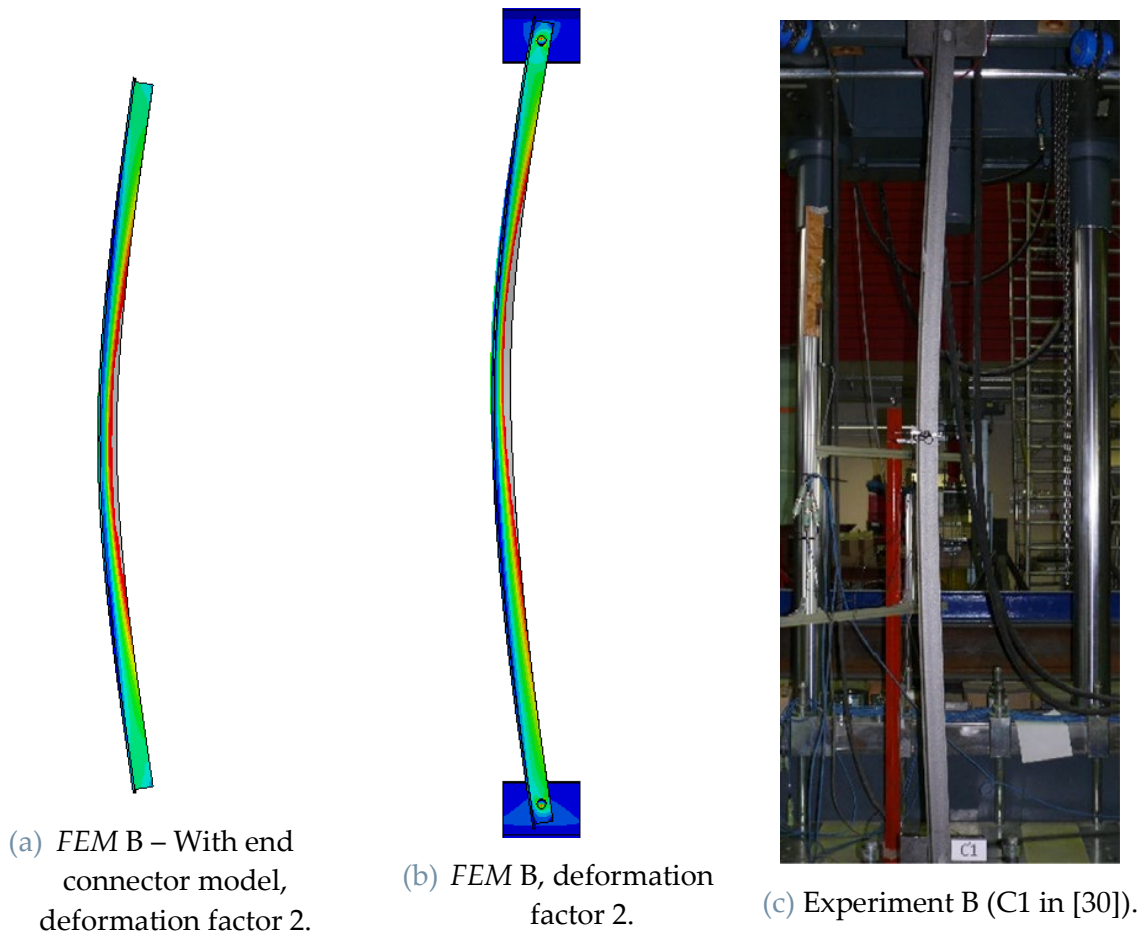

(a) *FEM* B – With end connector model, deformation factor 2.

(b) *FEM* B, deformation factor 2.

(c) Experiment B (C1 in [30]).

Figure 3.14: Comparison with the *3D FE* reference and real counterpart.

3.3. Conclusive discussion on the results

Different joint modeling methodologies have been tested and the results have been compared to the more detailed *3D FEM* and experimental data. The following can be said about the results:

- The simpler connector models, such as *Rigid* or *Linear*, have in general a fair accuracy on the display of at least the ultimate load and the right mode, and, given their simplicity, they are of interest in the study of the lattice tower.
- *Beam* elements with joint connector models are as accurate as the other types, if not more. In other words, it is possible to assess that if the boundary conditions are well represented (and if the buckling mode is not local), the element type does not affect the load estimation.

- The single bolt model is strongly sensitive to initial applied geometrical imperfection, which partly explains the large range of ultimate loads obtained.
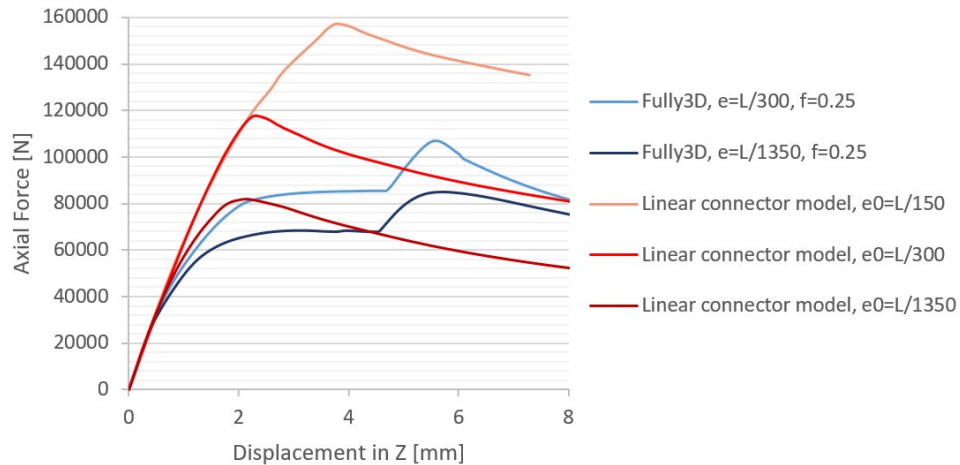
Figure 3.15: Load - displacement curves for models with different initial imperfections. Depending on the applied imperfection magnitude, the ultimate load in (linear) connector models ranges of around ±34%, in *3D* models of around 25%.

This shows how, more than the single initial imperfection magnitude, the imperfection shape and position within the brace can play a huge role in the load capacity estimation using *FEM*. This is supported by the studies of J. Wang et al. [18], which have found that, depending on the type and magnitude of the applied initial imperfection, the buckling capacity of tower members can vary between 82 and 125% of the nominal value. Similarly, in their study case, C. Affolter et al. [19] found a difference of around 10% in structure ultimate load estimation, depending on the applied mode.

4 Chapter four: Modeling of an assembly

It is crucial to assess how the knowledge built up in the last few Chapters, in simpler models, would transfer to a more complicated system.

The idea of using spring and dampers to model connections between lattice tower members is not new and it has been well documented: W.Q. Jiang et al. [34] and R. Ramalingam et al. [37] used Ungkurapinan stiffness functions [35] to model all the joints present in a lattice tower, then comparing the results with the experimental counterpart; M. Fong et al [38] applied linear spring to a simple model, experimentally verifying it.
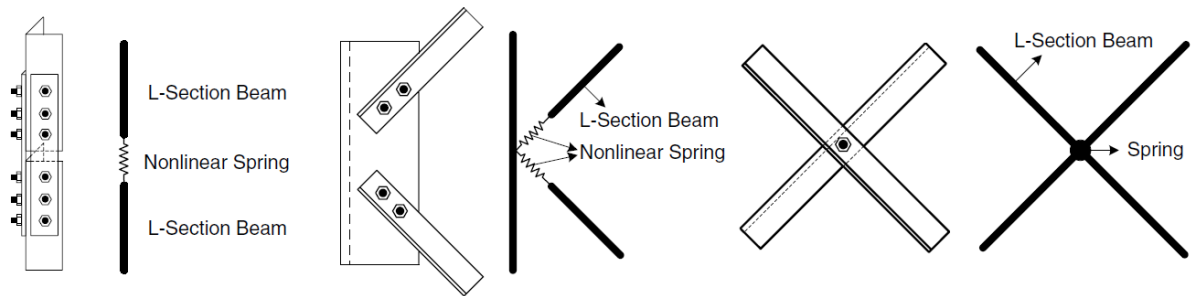
Figure 4.1: Model of the joints in [34].

In this Chapter, the joint modeling is applied to a simple subassembly of the lattice tower, later subjected to two different load cases, aiming to focus on different parts of the structure and visualizing what the effects of model simplification are.

As it is not possible to validate the lattice structures results with design standards, nor with any analytical solution, due to large displacements in the non-elastic regime and variable joint flexibility, the results are only compared with a *3D* model, when possible. Considerations on the applied methodologies are drawn in the view of employing them in the modeling of large lattice structures.

4.1. FE Model

Two similar sub-models have been built in order to test the capabilities of the methodology, the first one being a simple planar model of lattice structure face, the second a simplified section of the tower.

In all the simulations, a geometrical imperfection based on the previous *LBA* of *e=10mm* (*e₀=L/500*, with reference *L=5000mm*) has been adopted. The material parameters were the ones from the *bi-linear* model in Chapter 1, with yield strength S_y=420 MPa, and young modulus E=210 GPa.

Displacement controlled static step is again chosen as load application method, as the resulting load - displacement curve is monotonic.

4.1.1. Planar model

The structure is part of a section of the tower, specifically the 5th level from the base:
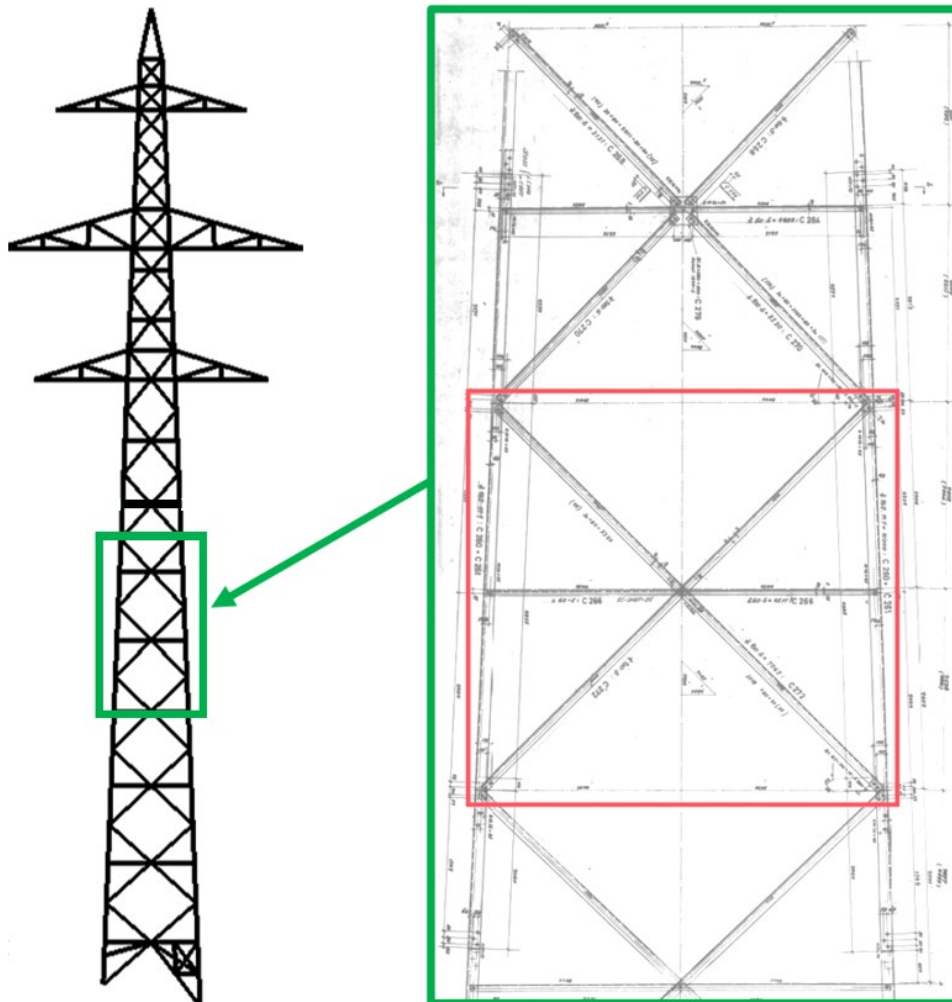
Figure 4.2: Side of the full tower sketch, the 5th level highlighted.

For the sake of reducing the modeling complications and possible misalignments, since the focus is only a comparative study between different methodologies, the face has been simplified, nullifying the tapering and rounding main the dimensions.

The resulting shape, with dimensions, is reported in Figure 4.3.
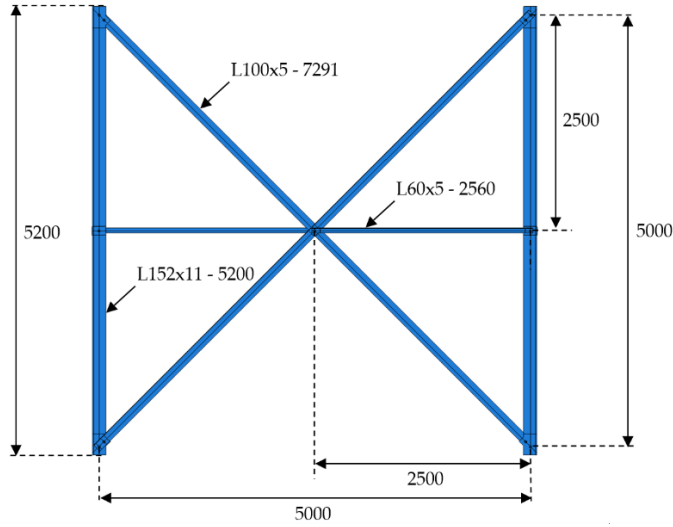
Figure 4.3: Dimensions of the chosen model.

Single-bolt connections have been placed in the horizontal braces (Figure 4.4b and 4.4c) and double for the diagonals when attached to the main legs (Figure 4.4a), slightly simplifying the head and nut geometry as the average between the hexagonal head's inscribing and circumscribing circumferences.

(a) Double-bolt   (b) Single-pin   (c) Single bolt
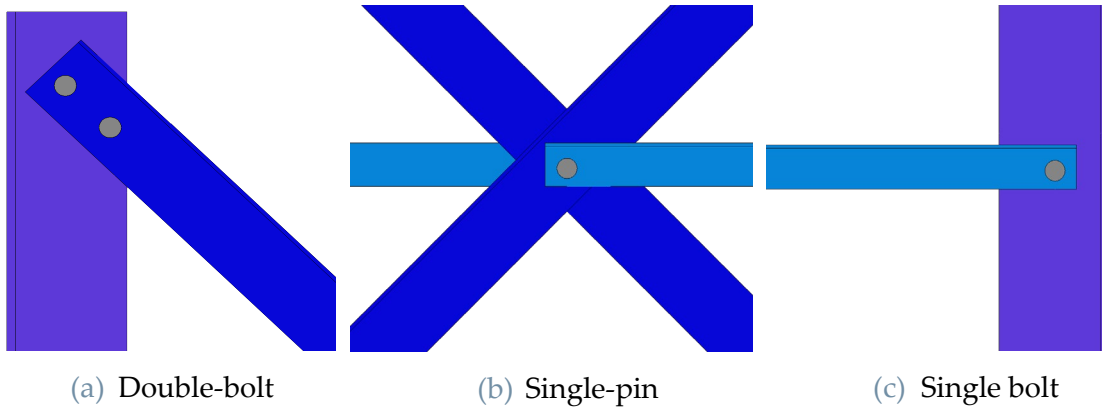
Figure 4.4: Details of the joints of the lattice structure.

Several model strategies have been tested:

- *3D model:* reference, with different friction coefficients *f=0.05, f=0.25, f=2.0*. Class 6 M16 (R_m=600 MPa, S_y=480 MPa) bolts have been used for the connections, according to *Eurocode 1993-1.8* [33] with a bolt pre-tensioning factor γ_{M7}=1.25:

$$N_{Pretensioning} = 0.7 \cdot \frac{R_m \cdot A_s}{\gamma_{M7}} = 67556 \ N \tag{4.1}$$

A_s is the nominal bolt area with a diameter of 16mm.

- *Beam model*: modeled in a single part made of *beam* elements rigidly connected;
- *Shell model:* modeled in a single part made of *shell* elements rigidly connected;
- *Shell+Beam model:* modeled in a single part with main legs modeled with *shell*, braces with *beam,* attached with stringers to have a more uniform load transfer.

4.1.2. 3D sub-structure model

The entirety of the section (highlighted in green in Figure 4.2) has been modeled, using similar strategies as in the planar model:

- *Beam model*: modeled in a single part made of *beam* elements rigidly connected;
- *Shell+Beam model:* modeled in a single part with main legs modeled with *shell*, braces with *beam,* attached with stringers to have a more uniform load transfer.

A complete *3D* model was not a possibility for such large substructure, due to time constrains in assembly, as it required the accurate positioning of such large number of parts and bolts. Even in a single part with only *shell* elements, the extrusion of the elements is as tedious and inefficient. Another limitation is the large number of elements created, exponentially increasing the computation time.
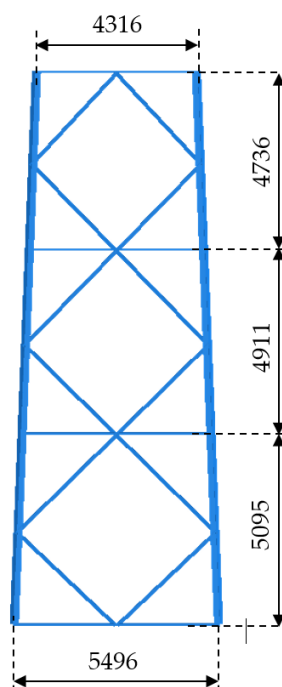
Figure 4.5: Dimensions of the model face.
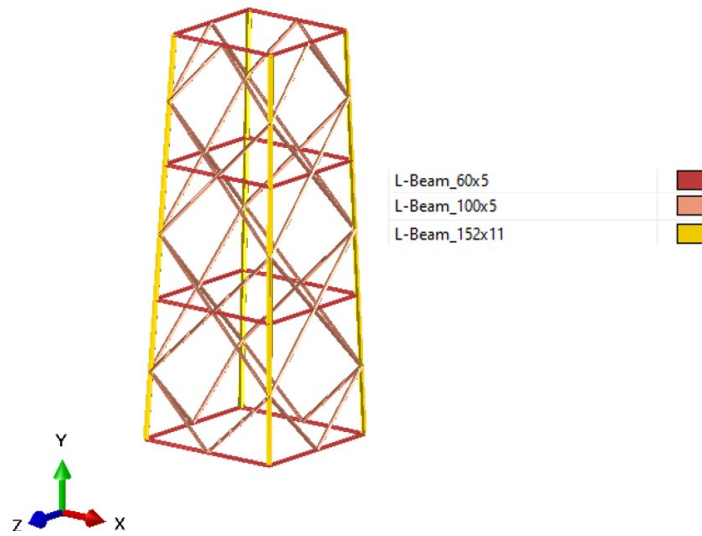
Figure 4.6: Model sections.

4.1.3. Connector models

Furthermore, three *connector models* have been analyzed for both the planar and *3D* substructure, based on "*Shell+Beam*" builds, and with stiffness functions out of full *3D* joint characteristics, in a similar way to the second step of the connector-modeling paragraph in Section 3.2.

The joint undergoes a series of load cases (a total of 12, two in each direction), in order to obtain the load-displacement curve (or stiffness function). Subsequently, a connector element is put in its place, using the previously obtained joint data.

The following models are created:

- *Shell+Beam, Linear Connector:* initial stiffness coefficient.
- *Shell+Beam, Nonlinear Connector:* full stiffness function.
- *Shell+Beam, Rigid+Free Connector:* hinge in the single bolt, rigid in double.

The result mimics what was done by W.Q. Jiang in [34]:
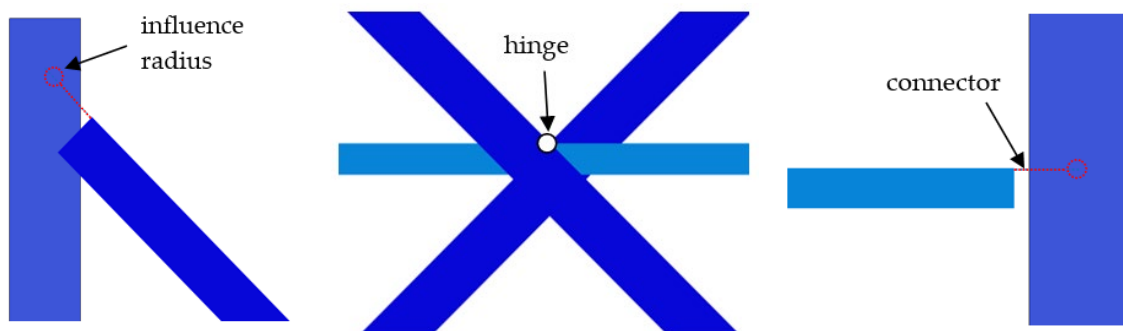
Figure 4.7: Details of the connectors as joints in the simplified structure.

4.1.4. Results for planar substructure

The load-displacement curves and the load capacity table, in terms of ultimate load on the single leg (total divided by two), are reported in Figure 4.8. None of the models has shown evidence of joint slippage. The ultimate load, in fact, does not have a large deviation in the *3D* models when changing the friction coefficient, nor when using different connector models.
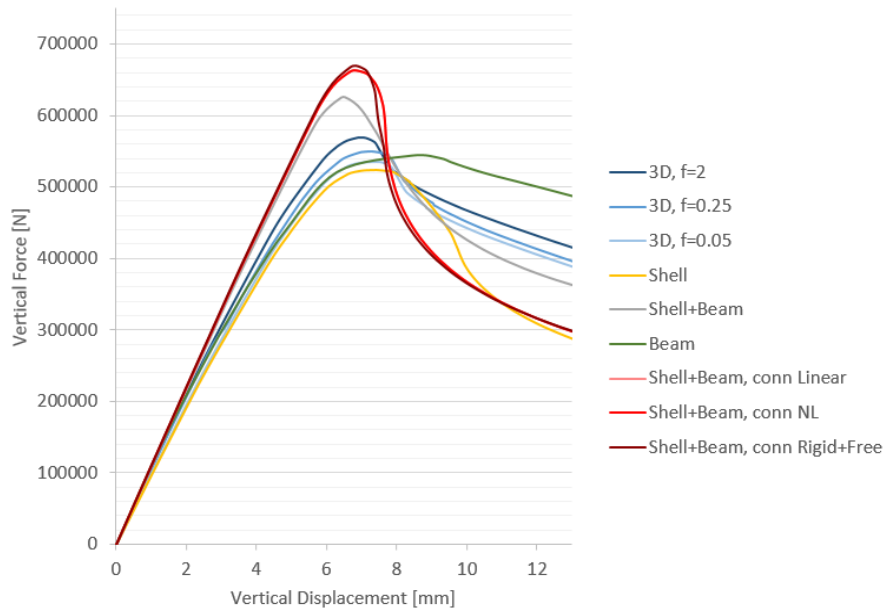

Figure 4.8: Load - displacement curves at the loading points.

	3D, f=0.25	Shell	Shell+Beam	Beam	Shell+Beam, conn Linear	Shell+Beam, conn NL	Shell+Beam, conn Rigid+Free
Load [kN]	534.8	524.2	625.4	544.4	662.9	662.8	669.1
Err. [%]	-	-2.9%	15.8%	0.8%	22.8%	22.8%	23.9%

Table 4.1: Load capacity compared to the *3D* model reference.

The main reason could be that the buckling is localized in the main legs with a flexural- buckling mode in *v-v* axis, close to the boundary, thus limiting the load sharing between legs and braces.

The models made solely of *beam* and *shell* elements appear to match the *3D* results the best, in terms of ultimate load, while all the hybrid models, built with both *shell* and *beam* elements, overestimate the load capacity quite a bit and undergo a different mode (*flexural-torsional* buckling). However, the accuracy of the results is debatable, as the buckling mode is very dependent on the boundary conditions, which in this case are too close to the diagonals attachment points.
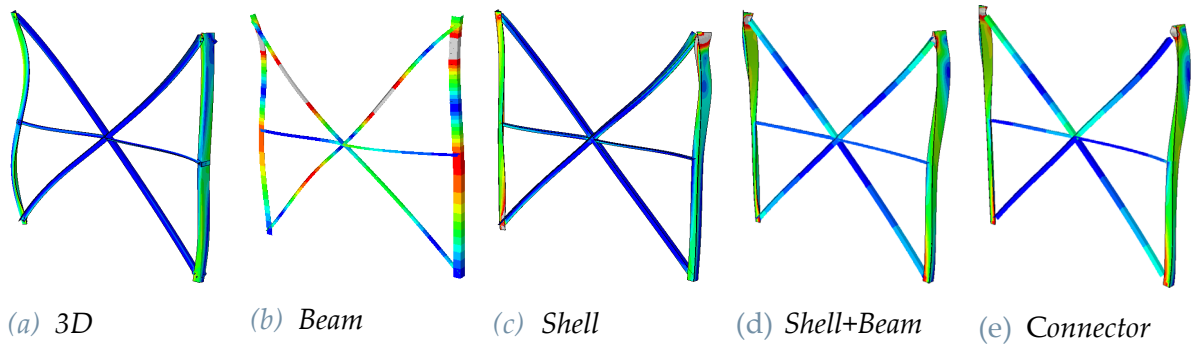
(a) 3D   *(b) Beam*   *(c) Shell*   *(d) Shell+Beam*   *(e) Connector*

Figure 4.9: Different buckling shapes for different models, scale factor of 10.

4.1.5. Results for 3D substructure

The load-displacement curves and the load capacity table, in terms of ultimate load on each leg (total divided by four), are reported in Figure 4.10 and Table 4.2.
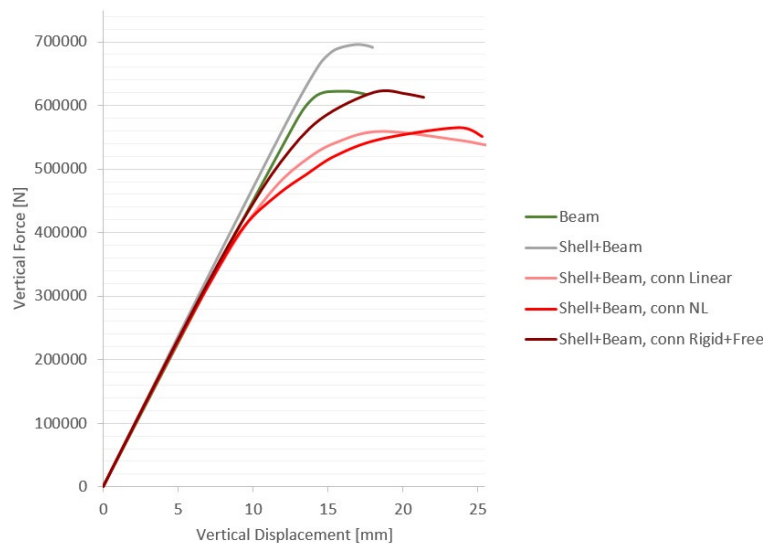

Figure 4.10: Load - displacement curves at the loading points.

	Shell+Beam	Beam	Shell+Beam, conn Linear	Shell+Beam, conn NL	Shell+Beam, conn Rigid+Free
Load 3D structure [kN]	696.0	621.8	559.1	564.7	621.0

Table 4.2: Load capacity comparison between *3D* geometry models.

In this case, the boundary conditions are well set and all the models undergo the same flexural buckling mode in the *v-v* axis.

The difference between the models with rigid joints and the ones with connector stiffness is now more substantial. There is also a minor difference between the one using only the initial stiffness and the one using the joint model, the slip does not

change the load capacity. The model with rigid connectors shows a higher load of around 10% with respect to the linear and nonlinear stiffness models. This is in line with the results from Y. M. Darestani et al. [17] predicted, a load capacity reduction of 6% and an increase in displacement at ultimate load of 16.7% when using joint flexibility models accounting for slippage in large assemblies.

The *Shell+Beam* strategy has between 12.1 to 24.5% higher instability load than the rest of the models. One reason might be the extreme stiffening provided by the stringer elements that connect the diagonals to the legs.

| *(a)* *Beam* | *(b)* *Shell+Beam* | *(c)* *Connector* |
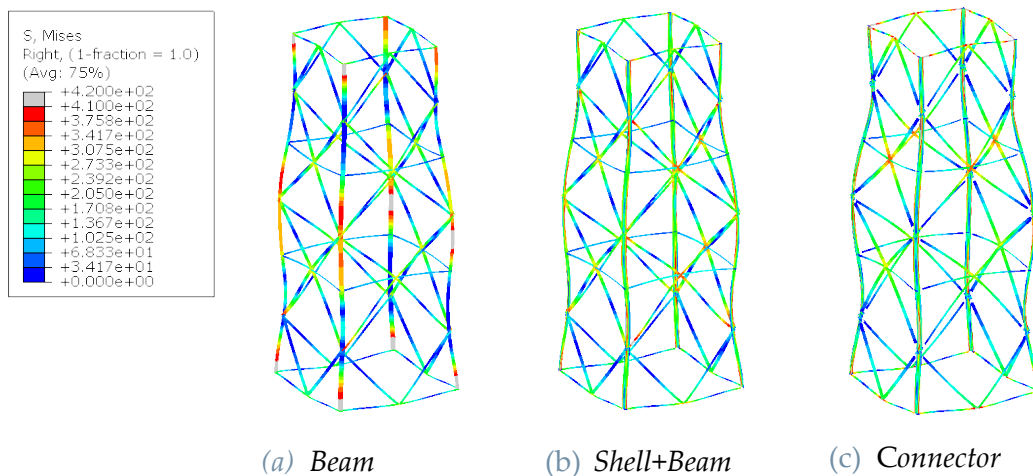
Figure 4.11: Different buckling shapes for different models, scale factor of 10.

However, since a *3D* model accounting for joint slip was not analyzed, it is hard to say which modeling approach is the most accurate.

4.2. Conclusive discussion on the results

Two subassembly geometries have been analyzed with different modeling approaches and the results have been compared.

Even if there is a clear overestimation, the joint simulation produces coherent results and can be adopted to achieve a physically accurate phenomena description. However, it requires consistent effort for *3D* joint sub-model creation, stiffness function modeling, connector built up and validation, thus losing convenience if these steps have to be carried out for a large number of times. It might as well be easier to build a completely *3D* structure. Moreover, connector models take a long to be set up, since no quick way to set up multiple joints at once is present in *Abaqus 2021.*

The hybrid (*Shell+Beam*) models are the most suited for the modeling of a large structure of the studied case, being easy to set up. It consistently tends to overestimate the buckling capacity, thus being conservative in the sense of failure analysis. Moreover, contrarily to a model made only with *1D* elements, it is also able to display different buckling modes other than the purely *flexural*.

However, in a more general design approach, a *Shell+Beam* model is not suited for all the design phases, as a lower load capacity estimation is preferred. Nevertheless, it could be used for *Failure Mode, Effects, and Criticality Analysis (FMECA)*, in which the correct reproduction of failure causes and effects is preferred.

5   Chapter five: Towers analysis and load capacity estimation

The initial studies and analysis on-site suggest that the collapse of the structure is due to the overcoming of the load-bearing capacity due to excessive wind loads.

The first topic to address is the load capacity estimation under quasi-static loading.

Having perfected the approach to structural analysis for frame structures in the past Chapters, the main challenge was related to the wind direction and speed realistic estimation. Different design standards and experimentally derived methods have been compared.

The structural analysis is conducted initially via *LBA*, to obtain an initial estimate, later with *RIKS*, to perform a static *pushover* analysis, determining the ultimate load as a margin with respect to the design values, and hinting on the post-buckling behavior.

5.1.   Line FE model for load estimation

This model's goal is to set up the line loading.

The entirety of the line segment from tower n19 to tower n26 has been modeled. The first and last towers have been neglected and replaced with pin joints, as they are "*Abspannmasten*" (tensioning pylons) designed to stop a cascade propagation in events of this type.

The positioning of the towers (which stand over concrete foundations), has been done according to the technical data. They are aligned in an almost straight line.
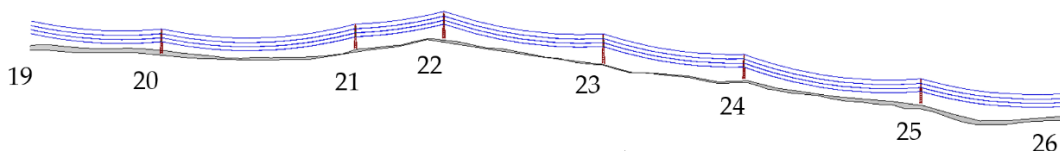
Figure 5.1: Tower position in the line.

The modeling has been done following the conclusions drawn in Chapter 4. The two options were to use *beam* elements for the entirety of the structure or a hybrid between *beam* and *shell* elements.

In this initial stage, this model was used only for the load case estimation. As the main focus was to accurately reproduce the tower deformation within elastic domain, the towers are modeled using single-span *1D* elements connecting the intersections, a stable enough solution that avoids the diverging plastic hinge behavior for loadings approaching collapse (more about that in Section 5.4).
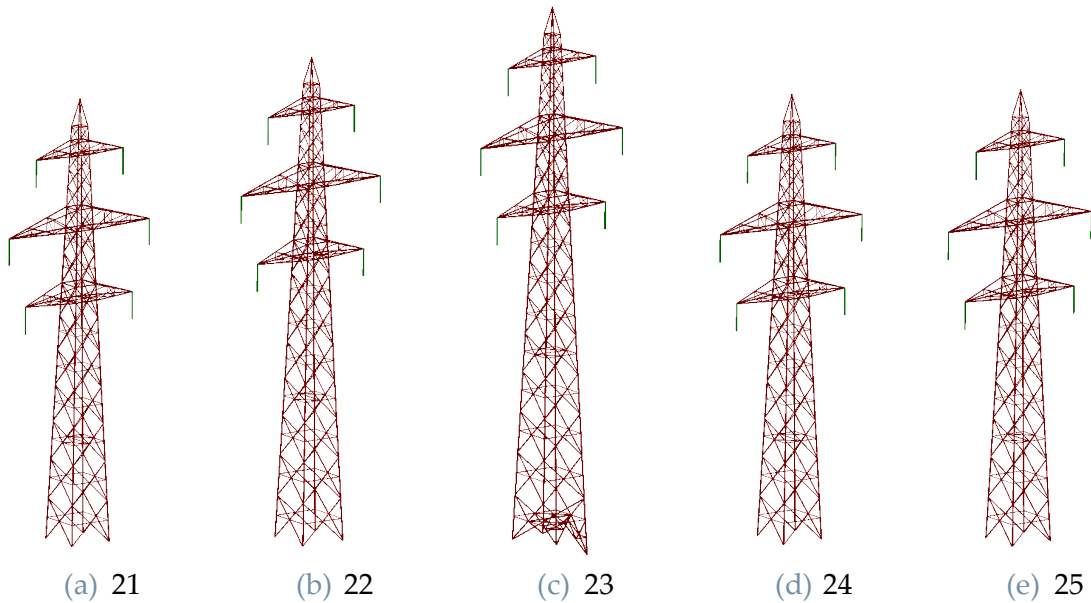

| (a) 21 | (b) 22 | (c) 23 | (d) 24 | (e) 25 |

Figure 5.2: Towers shape.

The cables, as in X. Liu et al. [39], were modeled as truss elements, *1D* elements that have only unidirectional tension elasticity, in accordance also to the ideal string hypothesis.

The loading of the cable, on which the loading on the masts depends, is basically shape-governed, thus it is focal to have good precision in its estimation.

The deformed shape of each wire under gravitational load was taken from technical drawings (Figure 5.3) using an image data extraction tool.

The lack of data on the undeformed shape has been addressed via iterative estimation:

1. A simple but effective first guess value could be obtained by subtracting the displacement under gravitational load of a straight string of the same span.

2. By using *Abaqus FE*, the undeformed shape can be checked under gravity if it matches with the deformed.

3. If not, correct the undeformed shape of the error, until it is small enough.
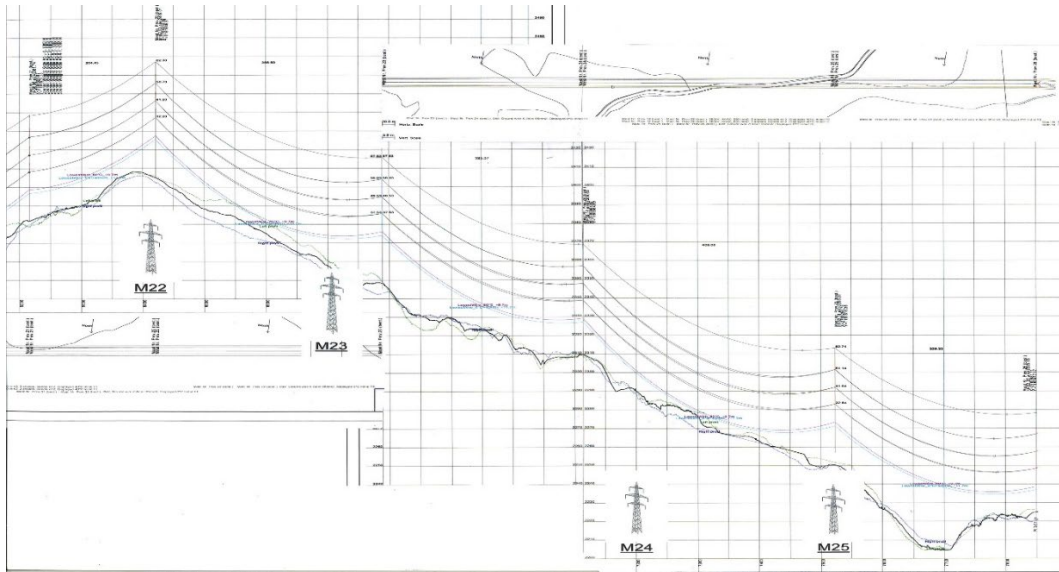
Figure 5.3: Line span dimensions [10].
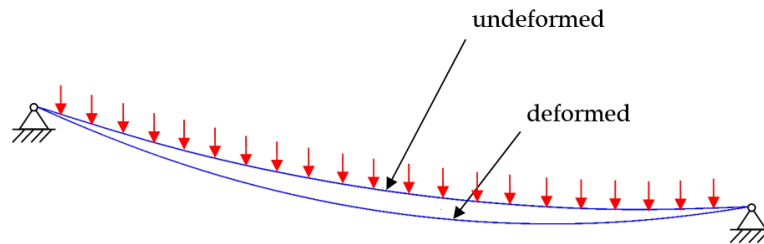
Figure 5.4: Cable deformation under load.

Another way could be to use the formula for catenary elements, but the matter is fairly complicated and not the scope of the study.

An example of the method could be found in R. Anshika [40], or in X. Liu et al. [39], in which the method is applied for the determination of the sag profile.

The ground profile was taken from the technical drawings as well, as a rigid surface swept between the profile underneath the line and the one 20m on the right side. This profile has been linearly extended further to around 80m, in order to contain the collapsed towers and cables.
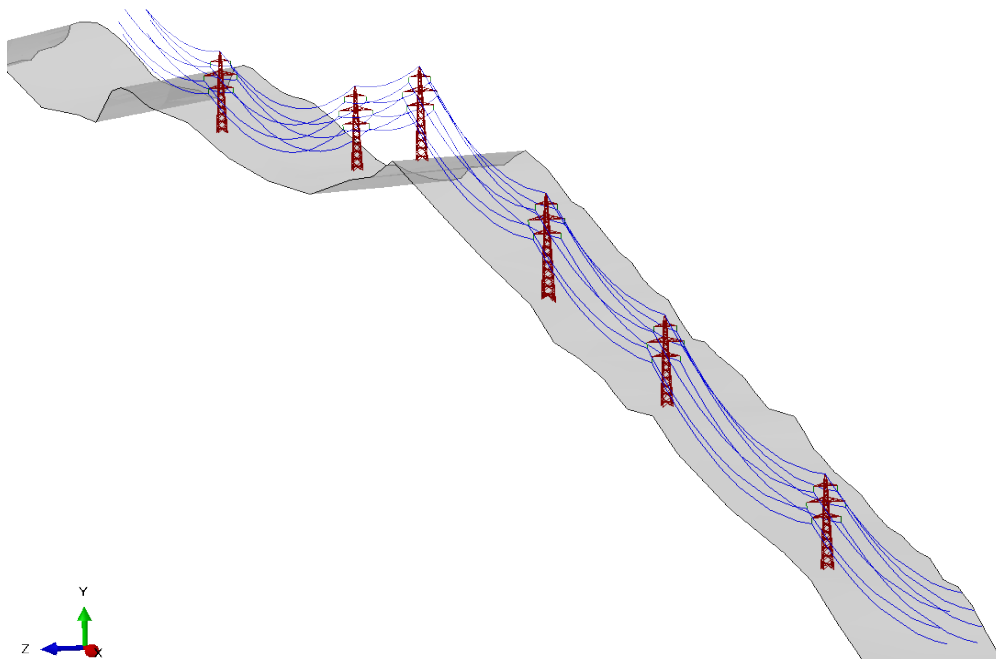
Figure 5.5: Line model view.

The span dimensions are the following:

Considered span	Span length [m]
n19 – n20	321.1
n20 – n21	445.4
n21 – n22	204.4
n22 – n23	368.5
n23 – n24	325.3
n24 – n25	409.0
n25 – n26	329.3
Total	2370.9

Table 5.1: List of cable spans, source *IED* [41].

Property	AAAC-600mm^2 (transmission)	Steel-95mm^2 (earthwire)
Cross-section area [mm2]	600.38	93.3
Outer diameter [mm]	31.86	12.62
Density [Kg/m3]	2813.3	7298.7
Ultimate tension [kN]	177.1	123.5
Modulus of elasticity [Mpa]	55000	175400
Thermal expansion [10-6]	2.3	1.15

Table 5.2: List of cables mechanical properties, source *IED* [41].

Considered tower	Elevation [m]
n19	2388.8
n20	2375.6
n21	2381.7
n22	2405.2
n23	2348.0
n24	2314.2
n25	2256.6
n26	2225.1

Table 5.3: Line elevation, source *IED* [41].

As for the insulators, they have been modeled as *beam* elements with circular cross-section of diameter 250mm, length of 4.95m and weight of 110 Kg.
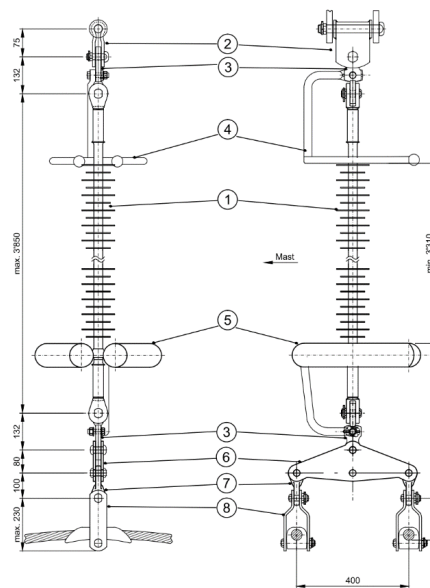
Figure 5.6: Insulators design [41].

5.2. Wind model

How to model the wind is a challenging and focal task. Without experimental or computational reference, the only remaining option is to rely on standards. A comparison is required, to obtain a better sense of the problem and avoid too conservative assumptions.

SIA 261/1 [13] and *RS 734.31* [42] are considered as a mean of comparison with the load cases provided by *IED* [10], while the *Eurocodes* would provide a different perspective.

Moreover, an empirical method has been developed based on experimental data.

All the following calculation methods have been integrated into a *MatLab* [43] code, in order to easily create the load cases in *Abaqus* [5] via *Macros*.

The load, according to the different codes considered, can be applied in several ways:

a) As an overall, considering the entire wind facing area;

b) Level-wise, dividing the tower into sub-assemblies and applying the codes separately on each;

c) To every single brace, accounting for the force separately on every element that the tower consists of.
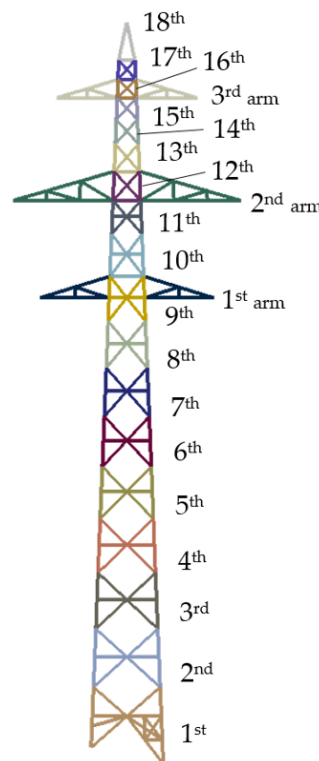
Figure 5.7: Structure subdivision into sections or levels for the wind load application.

Since the first method is too simplistic for an appropriately accurate load estimation, and the third requires additional effort without assuring a realistic result, the second method was therefore chosen and the tower was divided into 18 levels and 3 arm sections.

The load was applied on the structure nodes: 4 each level and 8 each arm.

The wind load on the cable has been applied as body-force, since truss elements in Abaqus do not support distributed loads:

$$f_w(z) = \frac{F_w}{A_{wire,section} \cdot l_{wire}} \tag{5.1}$$

When instead analyzing the single tower, the wind load for every cable is then applied to the arm tip, where the insulator is connected (Figure 5.8).
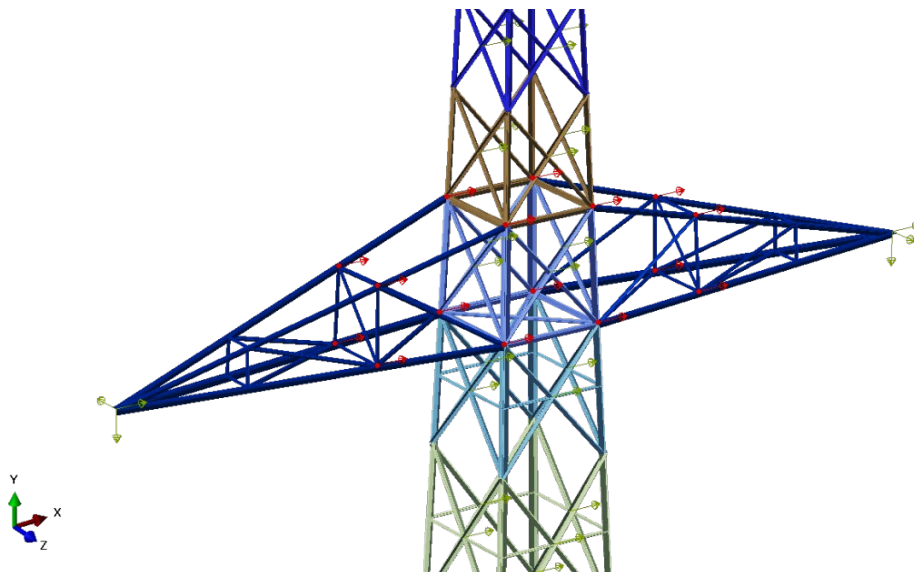
Figure 5.8: Load application on the structure: in yellow on the levels and on the conductors, in red on the arms.

In the following codes, only wind load is considered, without any overload or safety factor applied.

5.2.1. RS 734.31

The swiss norm *RS 734.31* [42], also called "*LeV*" for German-speaking part ("*LeitungsVerordnung*") or "*OLEI*" for French-speaking part (*Ordonnance sur les lignes électriques*), was written and published in 1994 and is the one used by all the Swiss companies to design lines and structures within Switzerland.

It consists of a series of static load cases to verify the structure under working conditions (mainly weather: temperature, ice, wind, rain,…).

An example of load case is the following:

Parameter	Value / consideration
Temperature	0°C
Ice overload	No
Wind on wires	Yes
Wind on structure	Yes
Wind direction	Transversal
VERTICAL Forces	100% of the resultant vertical forces due to earth wire 100% of the resultant vertical forces due to conductors (all) 100% of the resultant vertical forces due to insulators 100% of the resultant vertical forces due to the structure
TRANSVERSAL/LONGITUDINAL Forces	100% of the resultant horizontal (transversal / longitudinal) forces

Figure 5.9: Example of *load case 3.1, RS 734.31* [42].

According to *Appendix 15*, the wind pressure depends on the maximum height of the structure:

Height of the structure H [m]	Wind pressure on the wires [Pa]	Wind pressure on lattice towers with angles [Pa]
H < 30	500	1000
30 < H < 80	650	1200
H > 80 [(1)]	850	1600

Figure 5.10: Wind pressure, *Appendix 15, RS 734.31* [42].

As the structure height is 68 m, the wind pressure q_b is therefore taken as 1200 Pa for the structure and 650 Pa for the wires.

For design purposes, the wind pressure is usually applied on the wires with a reduction factor (between 0.76 and 1) dependent on the span. Since the studied case is not a regular event, the full pressure value was considered.

The wind is applied to the structure without any profile (constant through the height), on the section projected area using the same shielding factor:

$$F_i = q_b \cdot (1 + \alpha_i) \cdot A_{p_i} \tag{5.2}$$

5.2.2. SIA 261/1

Swiss standards on actions on structures, derived from the *Eurocodes. Chapter 6, SIA 261/1* [13] on wind action is based on a dynamic pressure, characterized by a height profile dependent on type of terrain roughness:

$$q_p(z) = c_h(z) \cdot q_b \tag{5.3}$$

$$c_h(z) = 1.6 \cdot \left(\left(\frac{z}{z_0} \right)^{\alpha_r} + 0.375 \right)^2 \tag{5.4}$$

z_0 and α_r depend on the terrain type, according to *Table 4, SIA 261/1*:

Categoria del terreno	Esempi	z_g [m]	α_r
II	riva lacustre	300	0,16
IIa	grande pianura	380	0,19
III	località, zona rurale	450	0,23
IV	zone urbane estese	526	0,30

Figure 5.11: *Table 4, SIA 261/1* [13].
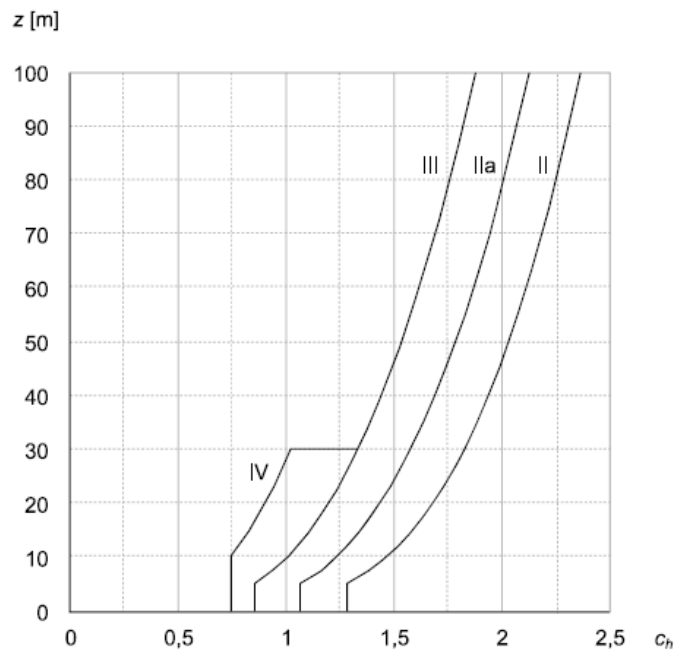
Figure 5.12: Resulting wind profile coefficients *SIA 261/1* [13].

Even though it refers to flat land wind profile, *curve II* has been adopted, as the others refer to proximity with buildings or obstacles.

The base pressure q_b value can be derived from the measured values in the area of the event. However, no measurement system was active during the night of the collapse.

SIA provides fortunately maps of wind pressure magnitude in Switzerland:
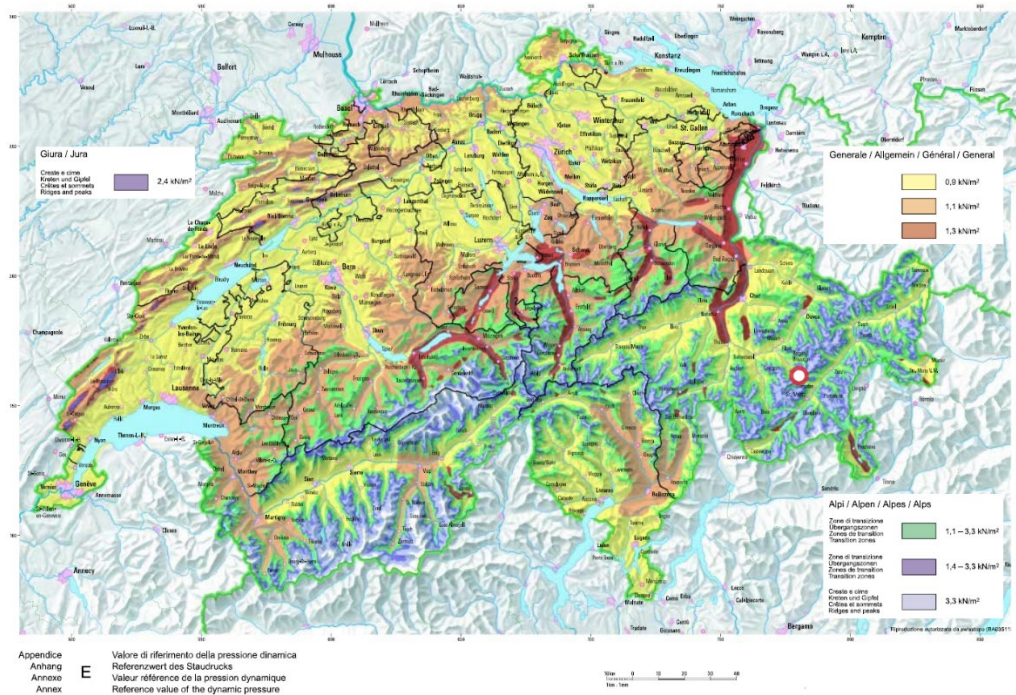
Figure 5.13: *SIA 261/1, appendix E* wind pressure map, *Albula Passhighlighted* [13].
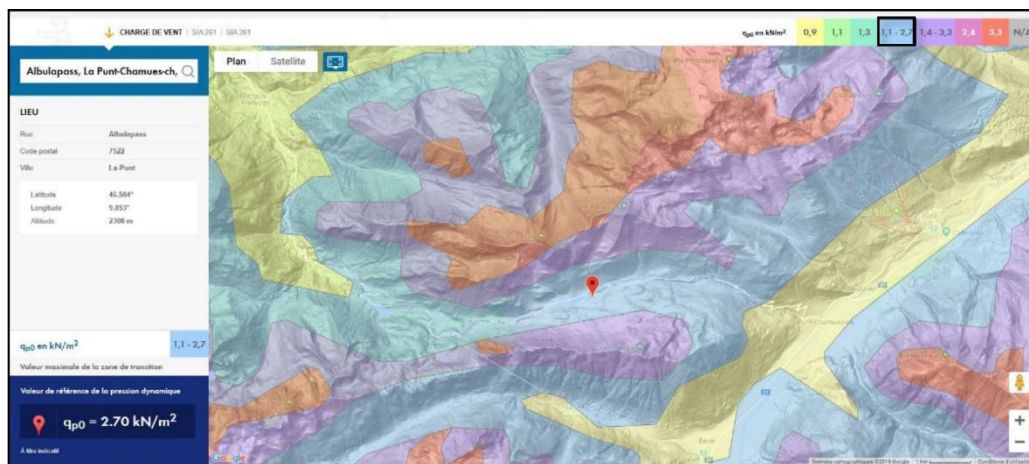
Figure 5.14: *SIA* weather maps on their website, *Albula Pass* [12].

Wind pressure values of 1.1-2.7 kPa are taken according to *SIA* weather map website, as it better represent the area; q_b=1.1 kPa is taken as a conservative estimate.

The force can be applied either via application on each single member, accounting for inclination and wind direction, or via application on the face projected area (*Table 75, SIA 261/1*).
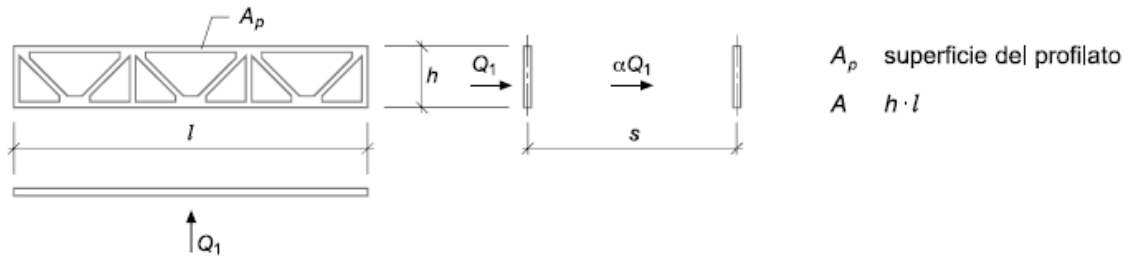
Figure 5.15: Force application scheme, *SIA 261/1* [13].

Coefficienti di forza globali							
superficie di riferimento = A_p							
$A_p : A$	0,01	0,1	0,15	0,2	0,3...0,8	0,95	1,0
c_{f1}	2,0	1,9	1,8	1,7	1,6	1,8	2,0
Coefficiente di riduzione per la snellezza c_{red}							
$A_p : A$			0,25	0,5	0,9	0,95	1,0
$l : h = 5$			0,96	0,91	0,87	0,77	0,6
$l : h = 20$			0,98	0,97	0,94	0,89	0,75
$l : h = 50$			0,99	0,98	0,97	0,95	0,9
$l : h = \infty$			1,0	1,0	1,0	1,0	1,0
Coefficiente di schermatura α							
$A_p : A$		0,1	0,2	0,3	0,4	0,5	0,6...1,0
$s : h = 0,5$		0,93	0,75	0,56	0,38	0,19	0
$s : h = 1$		0,99	0,81	0,65	0,48	0,32	0,15
$s : h = 2$		1,0	0,87	0,73	0,59	0,44	0,3
$s : h = 4$		1,0	0,9	0,78	0,65	0,52	0,4
$s : h = 6$		1,0	0,93	0,83	0,72	0,61	0,5

Figure 5.16: *Table 75, SIA 261/1* [13].

As the average ratios $\frac{l}{h} \approx \frac{s}{h} \approx 1$, a slenderness factor of 1 had been used. The shielding factor was taken as a function of $\frac{A_p}{h \cdot l}$.

The total force on the profile is then obtained from the following formula:

$$F_i = c_{f1_i} \cdot c_{red_i} \cdot q_{p_i} \cdot (1 + \alpha_i) \cdot A_{p_i} \tag{5.5}$$

As for the conductors, according to *Appendix C, Table 74*, they are considered as rough cylinders, with force coefficients from 1.1 to 1.3, depending on the wind pressure.

$d\sqrt{q_p}$	Coefficienti di forza globali c_f			
	superficie di riferimento = $d \cdot l$ (d = diametro, l = lunghezza, entrambi in m)			
≤ 0,3	1,2	1,2	1,2	1,3
> 0,3	0,5	0,7	0,9	1,1
○↕d	○ fili e aste lisci, tubi	○ fili e aste poco ruvidi	⊛ cavi conduttori o portanti a fili fini	⊛ cavi conduttori o portanti a fili robusti

Figure 5.17: *Table 74, SIA 261/1* [13].

The conductor force is then obtained through the following formula, where l_{cond} is the wire length and d_{cond} the diameter:

$$F_{cond} = c_{f,cond} \cdot q_p(z_{cond}) \cdot l_{cond} \cdot d_{cond} \tag{5.6}$$

5.2.3. Eurocode 1991-1.4

Eurocode 1991-1.4 [44] is specific for wind action, based on the use of a peak velocity pressure, accounting for mean static plus dynamic stochastic component.

The first step (*Section 4, Eurocode 1991-1.4* [44]) is to find a characteristic 10-minutes mean wind velocity 10mt above-ground, that can be derived from the wind pressure characteristic of the geographical area.

These values can be derived from SIA wind pressure maps via the formula:

$$v_{b0} = \sqrt{\frac{2 \cdot q_{b0}}{\rho}} \tag{5.7}$$

With the air density $\rho = 1.25 \ kg/m3$.

The base wind velocity is then calculated as:

$$v_b = v_{b0} \cdot c_{direction} \cdot c_{season} \cdot c_{probability} \tag{5.8}$$

$c_{direction}$ and c_{season} are direction and seasonal wind stochastic variabilities, that can be assumed equal to 1, if no information on those aspects is given.

$$c_{probability} = \left(\frac{1 - K \cdot \ln(-\ln(1 - p))}{1 - K \cdot \ln(-\ln(0.98))} \right) \tag{5.9}$$

Where probability for annual exceedance p is set as 0.02, shape parameter K is recommended of 0.2.

The base wind has then to be multiplied for the terrain roughness factors and the orography coefficient to obtain the mean wind velocity:

$$v_m(z) = v_{b0} \cdot c_r(z) \cdot c_o \tag{5.10}$$

The first coefficient is calculated as a function of height, depending on the terrain type from *Table 4.1, EN50341* (similarly to what done in *SIA 261/1*) *Terrain type II* is chosen, as there are no obstacles in the vicinity:

$$c_r(z) = k_r \cdot ln\left(\frac{z}{k_0} \right) \tag{5.11}$$

Terrain category		z_0 [m]	k_r
0	Sea or coastal area exposed to the open sea	0,003	0,155
I	Lakes or flat and horizontal area with negligible vegetation and without obstacles	0,01	0,169
II	Area with low vegetation such as grass and isolated obstacles (trees, buildings) with separations of at least 20 times obstacle heights	0,05	0,189
III	Area with regular cover of vegetation or buildings or with isolated obstacles with a separation of maximum 20 times obstacle heights (such as villages, suburban terrain, permanent forest)	0,3	0,214
IV	Area in which at least 15 % of the surface is covered with buildings which average height exceeds 15 m	1	0,233

Figure 5.18: *Table 4.1, EC 1991-1.4* [44].

The orography coefficient accounts for the increase in wind velocity over inclined ground profile:
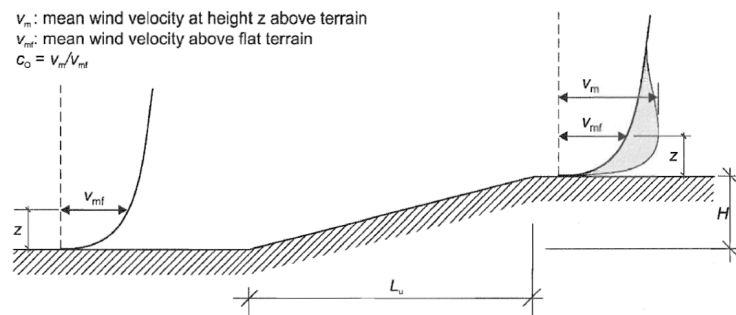
Figure 5.19: *Figure A1, EC 1991-1.4* [44].

The numerical calculation is a bit convoluted and, as the mountainous profile is complex and not treated in the standard (pass, an inclined valley in between two mountainsides, with some towers on an escarpment), would not prove accurate for the purpose anyway, hence the orography coefficient c_o is taken equal to 1.

The oscillatory wind component is considered via a turbulence intensity factor

$$I_v(z) = \frac{\sigma_v}{v_m(z)}$$ (5.12)

$$\sigma_v = k_r \cdot v_b$$ (5.13)

With σ_v as wind velocity standard deviation, considered constant with height.

The overall peak velocity pressure (accounting for the maximum dynamic wind velocity component) is then calculated according to the following formula:

$$q_p(z) = \left(1 + 7 \cdot I_v(z)\right) \cdot \frac{1}{2} \cdot \rho \cdot v_m(z) = c_e(z) \cdot q_b$$ (5.14)

This is extremely conservative: increasing of 7 standard deviations means to account for 99.99…% of the components in a normal distribution (the wind characteristic can be considered as such) so this rule might not apply.

The resulting c_e factor:
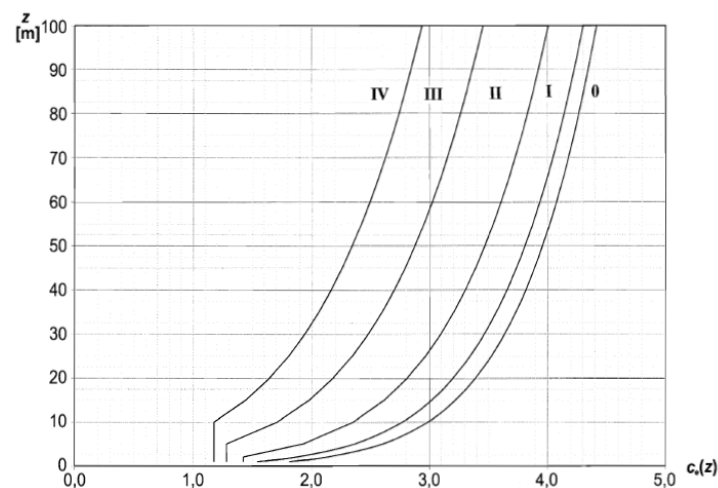
Figure 5.20: *Figure 4.2, EC 1991-1.4* [44].

The peak velocity pressure compared with *SIA* and *RS 734.31* distributions, is shown in Figure 5.21:
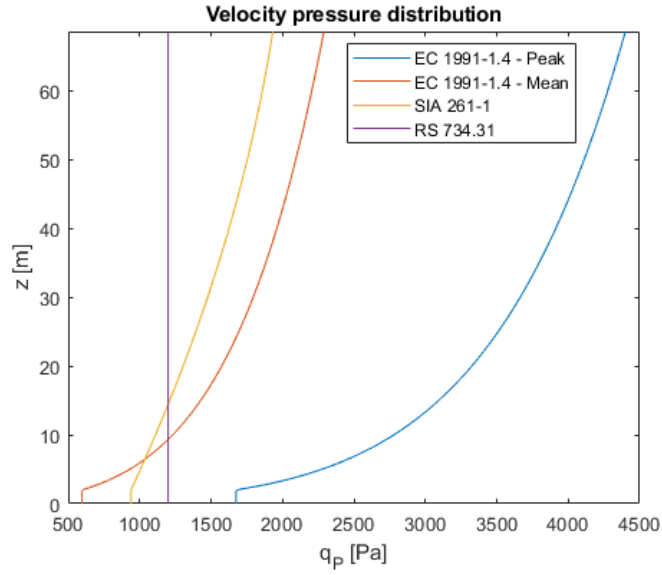
Figure 5.21: Comparison of different design standards' pressure distributions.

It is clear that the mean velocity pressure distribution without the dynamic component is more realistic and in line with the previously analyzed codes, thus it is going to be used in the study, thus:

$$q_p(z) = \frac{1}{2} \cdot \rho \cdot v_m(z) \tag{5.15}$$

The force on the surfaces is given by the following equation (*Section 5.3*):

$$F_i = c_s \cdot c_d \cdot c_{f,i} \cdot q_{p,i} \cdot A_{p,i} \tag{5.16}$$

Where $c_s \cdot c_d$ is the structural factor, c_f the force coefficient and A_p the projected area.

The structural factor includes the aeroelastic effects, accounting for the structure response to the peak loading. As this factor, based on calculations on the structure dynamics, does not have a large overall effect (±2%) and the loading is considered quasi-static, it is considered as 1.

The force coefficient is a combination of the force coefficient without end-flow (vortex formation due to profile shape, that causes additional drag) and an end-flow factor:

$$c_f = c_{f0} \cdot \varphi_\lambda \tag{5.17}$$

The force coefficient can be derived from interpolation of *Figure 7.34, EC 1991-1.4* and *7.35, EC 1991-1.4*:
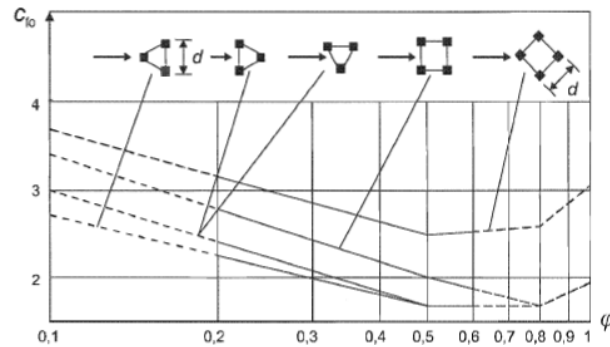
Figure 5.22: *Figure 7.34, EC 1991-1.4* [44].
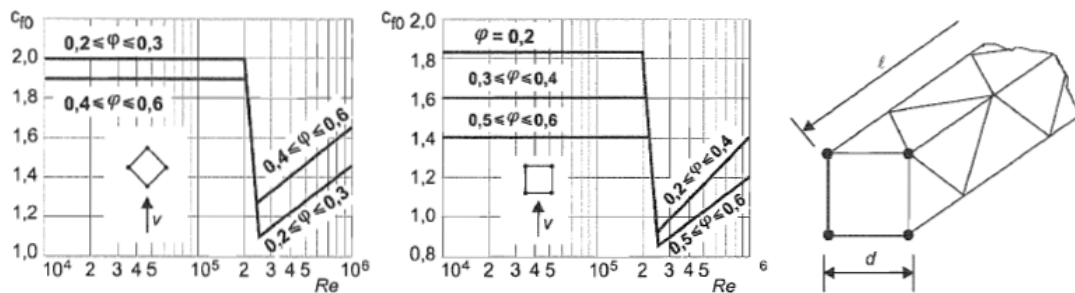
Figure 5.23: *Figure 7.35, EC 1991-1.4* [44].

Where the Reynold's number:

$$Re = \frac{d \cdot v_m(z)}{\nu}$$

(5.18)

In which *d, l* are the section reference lengths (Figure 5.23), ν the kinematic viscosity of the air (15·10-6 m²/s). The section solidity is the ratio between the projected and the section area:

$$\varphi = \frac{A_p}{d \cdot l}$$

(5.19)

The end flow coefficient can be derived from interpolation of *Figure 7.36, EC 1991-1.4*:
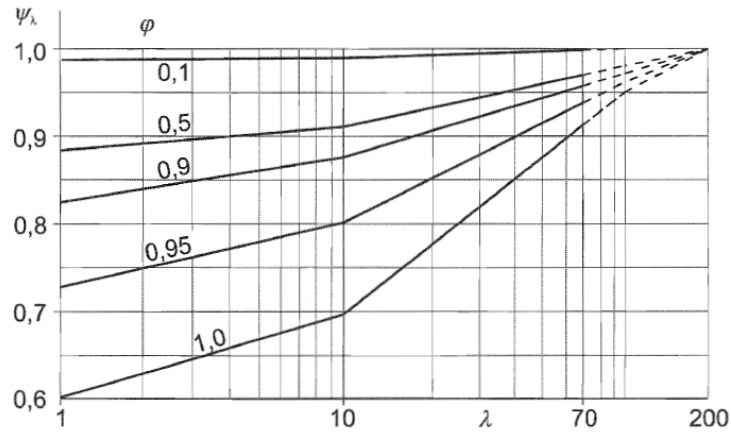
Figure 5.24: *Figure 7.34, EC 1991-1.4* [44].

Where the section slenderness for lattice structures is:

$$\lambda_{str} = \begin{cases} 0.7 \cdot \dfrac{l}{d} \\ 70 \quad if \ \ 0.7 \cdot \dfrac{l}{d} > 70 \end{cases} \tag{5.20}$$

The resulting formula for calculations is the following:

$$F_w(z) = c_{f,cond} \cdot q_p(z) \cdot A_{p,cond} \tag{5.21}$$

The wires can be considered very rough cylinders of diameter d_{cond} (*Section 7.9, EC 1991-1.4*):

$$c_{f,cond} = c_{f,cond} \cdot \varphi_{\lambda,cond} \cdot \kappa \tag{5.22}$$

Where the wire force coefficient can be found in *Figure 7.28, EC 1991-1.4* and the end flow coefficient in *Figure 7.34, EC 1991-1.4*, related to a slenderness coefficient:

$$\lambda_{cond} = \begin{cases} 0.7 \cdot \dfrac{l_{cond}}{d_{cond}} \\ 70 \quad if \ \ 0.7 \cdot \dfrac{l_{cond}}{d_{cond}} > 70 \end{cases} \tag{5.23}$$

Where k is the equivalent roughness.
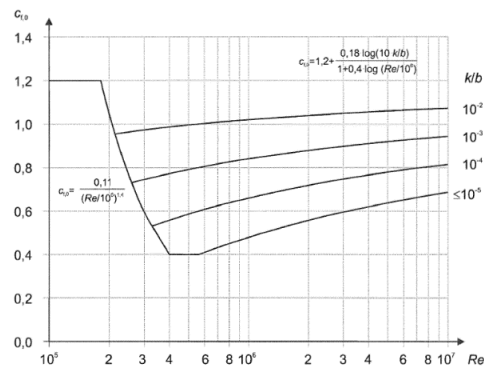
Figure 5.25: *Figure 7.28, EC 1991-1.4* force coefficient depending on Reynolds number [44].

Being coupled wires, an extra factor $\kappa=1.1$ is being considered if they are wind-aligned:

Figure 5.26: *Table 7.14, EC 1991-1.4* [44].

5.2.4. Eurocode 1993-3.1

Eurocode 1993-3.1 [4] expands on the general rules of *1991-1.4* [44], focusing on lattice towers.

The force coefficient is better estimated in *Annex B*:

$$c_f = c_{f0} \cdot K_\theta \tag{5.24}$$

K_θ is the wind incidence factor and, for angle sections, it is equal to:

$$K_\theta = 1 + K_1 \cdot K_2 \cdot \sin^2(2 \cdot \vartheta) \tag{5.25}$$

$$K_1 = 0.55 \tag{5.26}$$

$$K_2 = \begin{cases} 0.2 & if \; \varphi = 0 \div 0.2 \;\; or \; \varphi = 0.8 \div 1 \\ \varphi & if \; \varphi = 0.2 \div 0.5 \\ 1 - \varphi & if \; \varphi = 0.5 \div 0.8 \end{cases} \tag{5.27}$$

And ϑ is the angle of incidence with respect to the face normal.

The force coefficient is given by the following formula (for square base structures):

$$c_{f0} = 3.9 \cdot (1 - 1.5 \cdot \varphi + \varphi^2) \tag{5.28}$$

The total coefficient at a given angle of attack, however, is given by the combination of the ones of the structure faces:

$$c_f = c_{f1} \cdot \cos^2(\vartheta) + c_{f2} \cdot \sin^2(\vartheta) \tag{5.29}$$

$$c_{f1} = (1 + \eta_1) \cdot c_{f0} \cdot K_\theta \tag{5.30}$$

$$c_{f2} = (1 + \eta_2) \cdot c_{f0} \cdot K_{\theta+90^o} \tag{5.31}$$
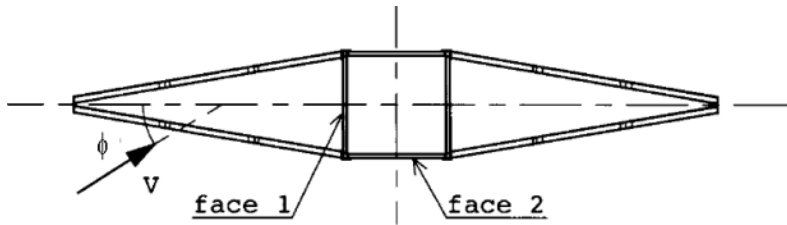
Figure 5.27: Load application in *EC 1993-3.1* [4].

Where η_1 and η_2 are the shielding factors from the faces on the opposite side (behind face 1 and face 2), function of the solidity:

$$\eta_r = (1 - \varphi)^{1.89} \tag{5.32}$$
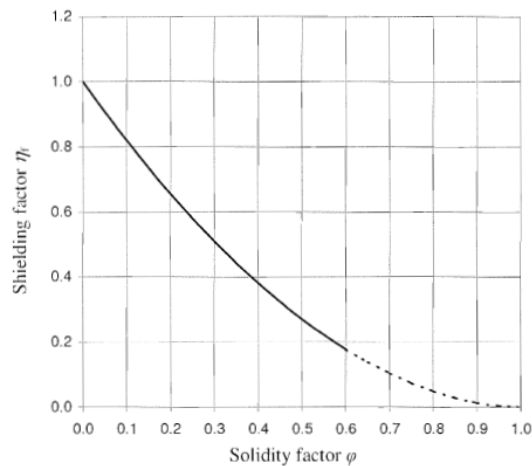
Figure 5.28: *Figure B2.4, EC 1993-3.1* [4].

As for the wires, a simple force coefficient c_f is used, according to *Table B2.1, EC 1993-3.1*, to be applied with the pressure distribution calculated in *EC 1991-1.4*:

(c)	Fine stranded cable, e.g. steel core aluminium round conductor, locked coil ropes, spiral steel strand with more than seven wires	Ice free: $\leq 6 \times 10^4$ $\geq 10^5$	1,2 0,9	
		Iced: $\leq 1 \times 10^5$ $\geq 2 \times 10^5$		1,25 1,0

Figure 5.29: *Table B2.1, EC 1993-3.1* [4].

5.2.5. EN50341

In a similar fashion to *Eurocode 1993-3.1* [4], *EN50341* [45] expands on the general rules of *1991-1.4* [44].

The first point touched is related to the air density value, here corrected for temperature and elevation in *Table 4.2, EN50341*:

Temperature T'	Altitude H			
°C	0 m	600 m	1 200 m	1 800 m
- 30	1,18	1,10	1,02	0,95
- 20	1,13	1,05	0,97	0,91
- 5	1,08	1,00	0,93	0,87
5	1,04	0,96	0,90	0,84
15	1,00	0,93	0,86	0,80
30	0,96	0,89	0,83	0,77

NOTE   The values in this table are derived from $\rho'/\rho = \dfrac{288}{T'} e^{-1,2 \cdot 10^{-4} H}$

where
ρ' is the air density corresponding to an absolute temperature, T' at an altitude, H,
H is the reference altitude in m for determination of air density,
T' is the absolute temperature in degrees Kelvin at an altitude, H.

Figure 5.30: *Table 4.2, EN50341* [45].

According to the formula, being the average altitude of the line 2300mt (it spans between 2200 and 2400 mt) and the temperature considered -20 C, the resulting air density is of 0.857 Kg/m3.

The main calculation formula is very reminiscent of the ones used before in *EC 1993-3.1*:

$$c_f \cdot A_p = c_{f1} \cdot A_{p1} * \cos^2(\vartheta) + c_{f2} \cdot A_{p2} \cdot \sin^2(\vartheta)$$
(5.33)

$$c_{f0} = 3.96 \cdot (1 - 1.5 \cdot \varphi + \varphi^2)$$
(5.34)

$$K_\theta = 1 + 0.2 \cdot \sin^2(2 \cdot \vartheta)$$
(5.35)

$$c_{f1} = c_{f01} \cdot K_\theta$$
(5.36)

$$c_{f2} = c_{f02} \cdot K_{\theta+90^o}$$
(5.37)

A special case are the cross arms, which in this case are only a function of the sole frontal area:

$$c_f \cdot A_p = c_{f0} \cdot A_{p,2} \cdot (0.4 \cdot \cos(\vartheta) + \sin(\vartheta))$$
(5.38)

$$c_{f0} = 3.96 \cdot (1 - 1.5 \cdot \varphi + \varphi^2)$$
(5.39)

With the frontal projection the one perpendicular to the wind:
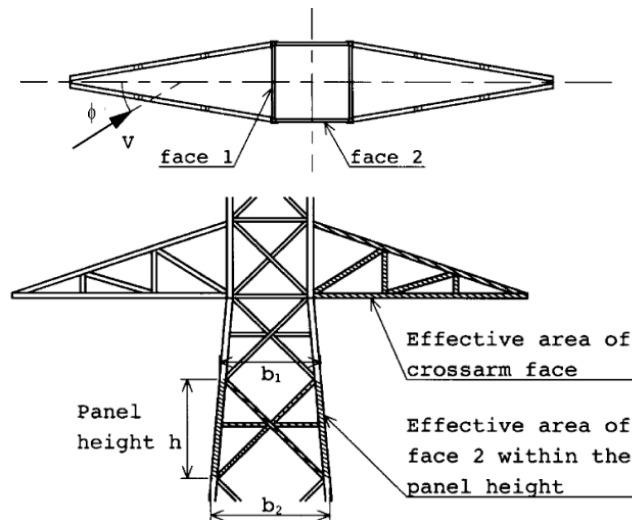
Figure 5.31: Arm effective area according to *EN50341* [45].

The resulting force from the wires, the support with equal line spans on both sides, following a straight trajectory (no turning in the line), as in the studied case, only a transversal force is applied, perpendicular to the line direction:
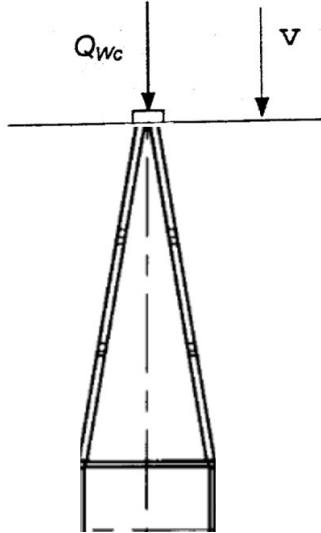
Figure 5.32: Wire force direction *EN50341* [45].

$$Q_{wc} = c_c \cdot G_c \cdot \cos^2(\vartheta) \cdot q_p(z) \cdot l_{cond} \cdot d_{cond} \qquad (5.40)$$

Where G_c is the structural factor, which can be found in *Table 4.4c, EN50341*:

z_0 [m]	L_m [m]	Reference height h for conductor [m]										
		10	15	20	25	30	35	40	45	50	55	≥ 60
0,05	100	0,70	0,73	0,74	0,76	0,77	0,78	0,79	0,79	0,80	0,80	0,81
	200	0,63	0,66	0,68	0,70	0,71	0,72	0,73	0,74	0,74	0,75	0,75
	300	0,60	0,63	0,65	0,67	0,68	0,69	0,70	0,70	0,71	0,72	0,72
	400	0,58	0,61	0,63	0,64	0,66	0,66	0,67	0,68	0,69	0,69	0,70
	500	0,57	0,59	0,61	0,63	0,64	0,65	0,66	0,66	0,67	0,68	0,68
	600	0,56	0,58	0,60	0,61	0,63	0,64	0,64	0,65	0,66	0,66	0,67
	700	0,55	0,57	0,59	0,61	0,62	0,63	0,63	0,64	0,65	0,65	0,66
	800	0,54	0,57	0,58	0,60	0,61	0,62	0,63	0,63	0,64	0,64	0,65

Figure 5.33: *Table 4.4c, EN50341* [45].

The considered height is the one of the center of mass of the wire. Since the cable position range from a height of 25 to 55 mt and the span is of around 370m, the structural coefficient is taken as 0.685 for all of them.

The drag factor c_c is the one from *Table B2.1, EC 1993-3.1* (Figure 5.29).

5.2.6. Experimentally derived wind load model

Another calculation method has been developed starting from experimental force coefficient values, in order to potentially obtain a more realistic load estimation.

Individual members are considered separately and the force on each is then summed up at every level, to simplify the force application within the *FE* software and to be quickly compared with results from the standards.

Experimental values from S. Prud'homme et al. [46] have been adopted for the structural elements. In their study, the drag and lift coefficients of angle profiles were measured, and the effects of turbulence, Reynold's number, profile shape (thickness and edge sharpness) were analyzed.

The experimental values are given in terms of drag and lift coefficients, based on the projected or the nominal area ("normalized" values):

$$C_D = \frac{F_D}{\frac{1}{2} \cdot \rho \cdot U} \tag{5.41}$$

$$C_L = \frac{F_L}{\frac{1}{2} \cdot \rho \cdot U} \tag{5.42}$$
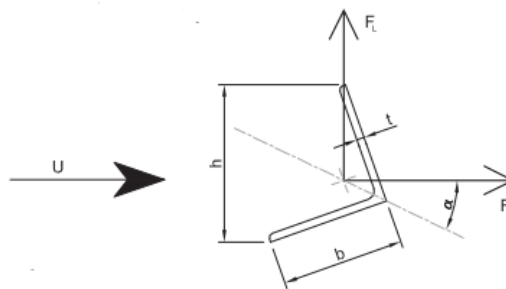
Figure 5.34: Wind speed and forces directions, according to Simon Prud'homme et al [46].

The chosen dataset are the normalized values of drag and lift coefficients from *experiment S52x3R*.

According to the experiments, the Reynolds number and the profile shape might give different coefficient values, but for the sake of simplicity, those effects are not taken into account in the present study.

The data has been interpolated via *pchip* interpolation (piecewise shape-preserving piecewise cubic interpolation, reduces overshoot in non-sinusoidal functions, something between a regular spline and linear interpolation):
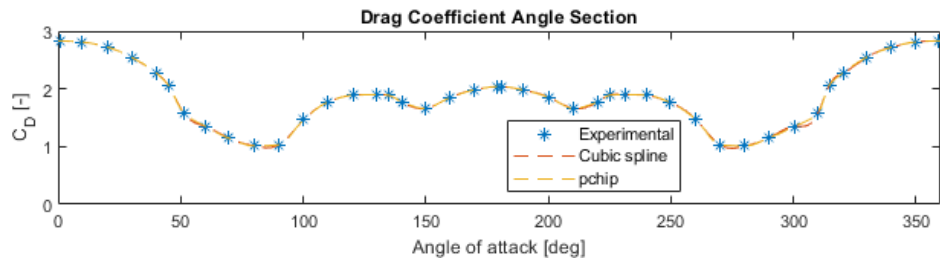
Figure 5.35: Drag coefficient interpolation from experimental data [46].
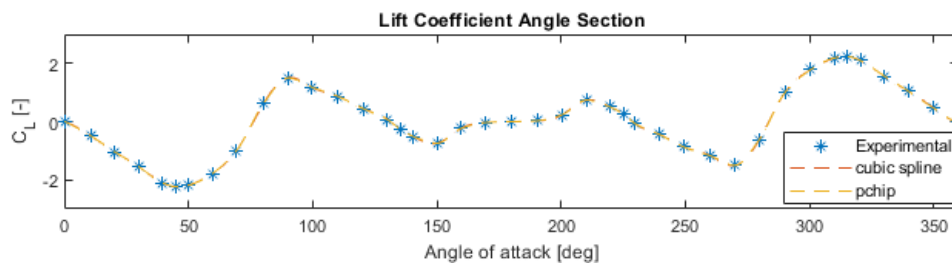
Figure 5.36: Lift coefficient interpolation from experimental data [46].

A shielding factor of 0.85 has been applied on the elements of the non-wind-facing side.

Deriving the force direction and magnitude for every member is a complex trigonometric problem:
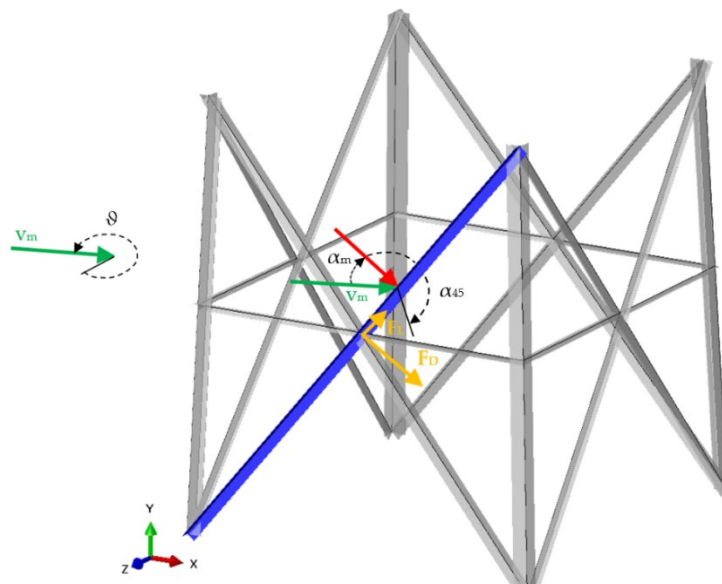
Figure 5.37: Force application on each member of the structure.

$$F_D = C_D(\alpha_{45}) \cdot A_{nom} \cdot q_p(z_m) \cdot \cos^2(\alpha_m) \qquad (5.43)$$

$$F_L = C_L(\alpha_{45}) \cdot A_{nom} \cdot q_p(z_m) \cdot \cos^2(\alpha_m) \qquad (5.44)$$

Where α_{45} is the angle with the plane normal to the member, and α_{45} the one with the reference face in the plane.

The drag from the velocity component parallel to the element is neglected, thus the resulting drag and lift forces lie on the normal plane of the member.

The conductor forces are based on the experimental values from J. C. Stroman et al. [47] experimental works, in which he measured the drag coefficient of different cable models.

Test specimen 142-15026-2 [47] was chosen as reference, since the conductor type (steel core with aluminum strands) resembles the studied case the most.
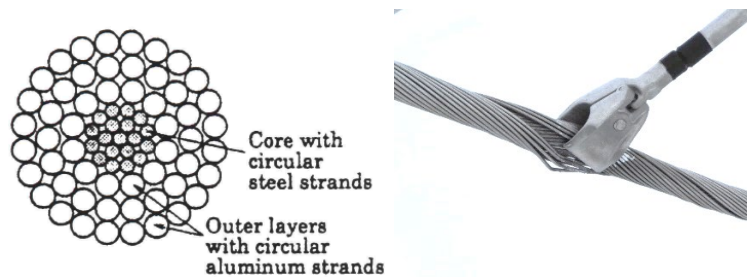
Figure 5.38: Cable section type (source *Swissgrid)* [47].

A coefficient of 1.05 is taken as mean value, as a Reynolds number higher than 10^5 is expected:
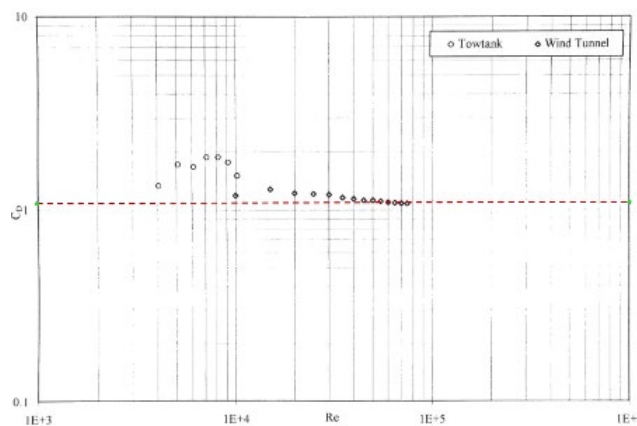
Figure 5.39: Drag coefficient of *Test specimen 142-15026-2* [47] varying Reynold's number.

Since the cables are coupled, a factor of 1.15 is added to the total force, according to *SIA 261/1*.

The cable span between towers n22 and n23 was chosen as reference, as it is representative of the segment between tower n22 and n26, close to the average dimensions.

The wires deformed shape (due to gravity) is subdivided into smaller elements, and on each, the same method is applied and the forces are then summed in each direction.
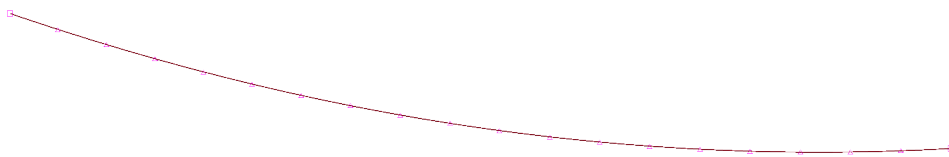
Figure 5.40: Cable profile used, subdivided into smaller elements.

Although more precise than a simple formula, it does not account for the deformation due to wind.
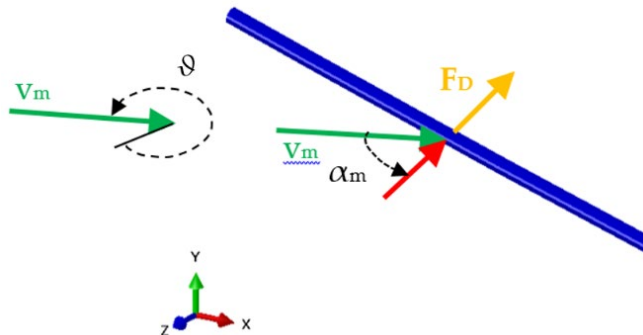
Figure 5.40: Drag force direction.

$$F_D = C_D \cdot A_{nom} \cdot q_p(z_w) \cdot \cos^2(\alpha_m) \tag{5.45}$$

In this case, the drag from the velocity component parallel to the element is also neglected, thus the resulting drag force lays on the normal plane of the member.

5.2.7. Models comparison and considerations

A comparison between wind models can be useful to understand the conservativeness of the assumptions made.

Tower n23 has been taken as a reference, since it is going to be the focus of further analysis. The base data in Table 5.4 has been chosen in order to equalize the initial assumptions to have a more fair comparison.

Standard	Base pressure for the structure [Pa]	Wind profile model	Base pressure for the cables [Pa]
RS 734.31	1250	RS 734.31	650
SIA 261/1	1100	SIA 261/1	650
EC 1991-1.4	1100	EC 1991-1.4	650
EC 1993-3.1	1100	EC 1991-1.4	650
EN50341	1100	EC 1991-1.4	650
Experimentally derived model	1100	SIA 261/1	650

Table 5.4: Standards base pressure values.

The forces have been computed in *MatLab* [43] with changing wind approaching angle, shown in a polar plots in Figure 5.41.

In terms of total forces on the structure, the forces are the highest at 45°, and the Eurocodes (*EN50341* [45], *EC 1991-1.4* [43] and *EC 1993-3.1* [4]) are definitely more conservative.

The forces from the experimentally derived model have a magnitude in between *EC 1993-3.1* and *EC 1994-1.4*, with a maximum obtained between 0° and 25°.

The forces at the conductors are very similar in terms of magnitude per approaching angle, going from the maximum at 0°, to zero at 90° (the only exception being the experimentally derived one).

(a) Total force on the structure.

(b) Total force on the cables.

(c) Total force (structure + cables).
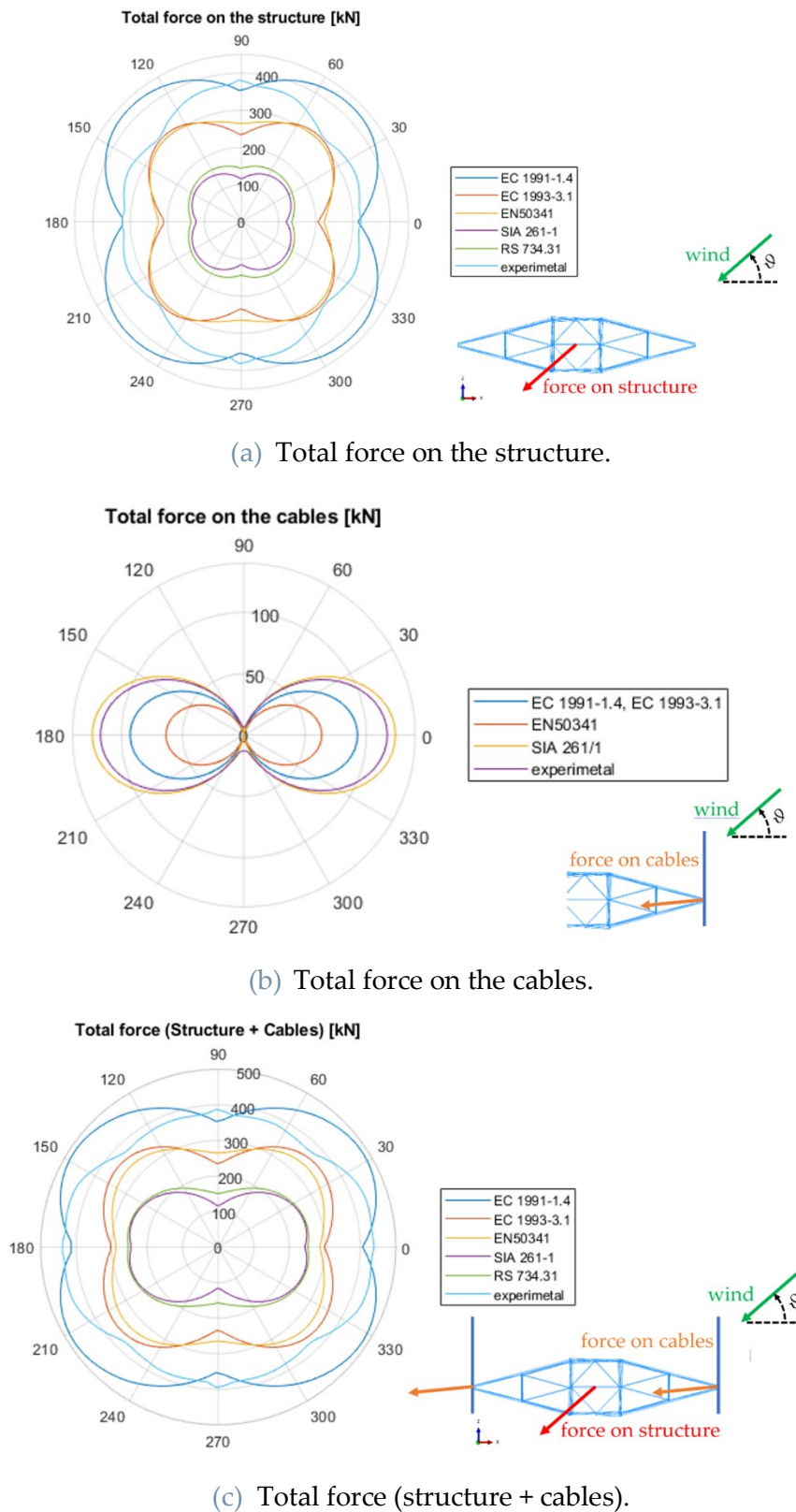
Figure 5.41: Total forces according to different standards, shown in a polar plot with respect to the angle of attack to the structure.
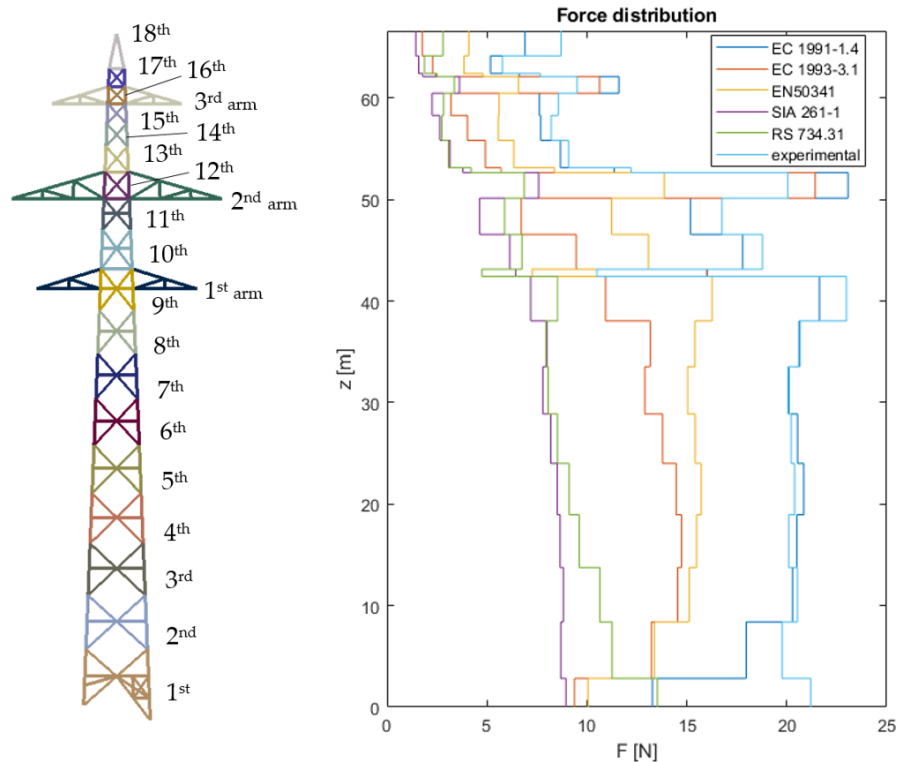
Figure 5.42: Forces per level height, with purely transverse wind (0˚).

The total values of forces for purely transverse wind (0˚) are the following:

Standard	Total force on the structure [kN]	Total force on the cables [kN]	Total forces [kN]
RS 734.31	134.91	123.83	257.06
SIA 261/1	119.95	123.83	242.70
EC 1991-1.4	313.51	92.87	406.38
EC 1993-3.1	205.75	92.87	298.60
EN50341	222.54	63.61	286.16
Experimentally derived model	321.75	117.14	438.90

Table 5.5: Total forces according to different standards, purely transverse wind.

In general, the experimentally derived method has proven not to be less conservative than the others.

Since the purpose of the study is to verify if the collapse was possible under specific weather conditions, to keep the load assumption conservative (in the sense of a failure analysis), the wind load according to *SIA 261/1* has been selected.

As for the load on the cables, the assumption of 650 Pa on the wires (in accordance with *RS 734.31*) was a little too optimistic, thus, the experimental model has been adopted.

Another reason to use these two values is that *IED* [10] have as well employed *SIA 261/1* in their calculations as well, thus being a good cross-reference.

5.3. Load model validation

As it is not possible to extract data from real experiments, for obvious budget constraints, the only way is to cross-validate the models built in different platforms: *PLS-Cadd* and *TOWER* models from *IED*, analytical solutions and *Abaqus FE* results.

The main load cases to be verified are the ones under gravitational load and under transverse wind.

5.3.1. Analytical model

A simple analytical verification is to assume the line is longitudinally balanced under gravitational load.

At each insulator, the horizontal forces have to be the same in the two attached spans (Figure 5.43). Moreover, the sum of the vertical component at the two sides has to equal the weight of the wire (Figure 5.44). Knowing the deformed shape of the wires, it is possible to obtain the weight and each angle at the wire ends:

$$tower\ equilibrium \quad T_{H1} = T_{H2} \tag{5.46}$$

$$cable\ equilibrium \quad \begin{cases} \rho_{wire} \cdot l_{wire} \cdot A_{wire,section} = T_{V1} + T_{V2} & \text{(5.47a)} \\ T_{H1} = T_{H2} & \text{(5.47b)} \end{cases}$$

Tension at wire ends and vertical forces on the tower can be used for reference.
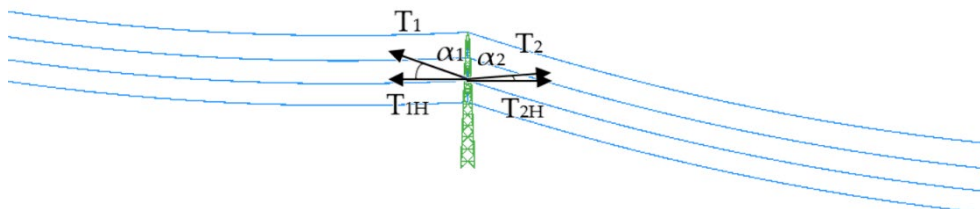
Figure 5.43: Equilibrium at each tower.
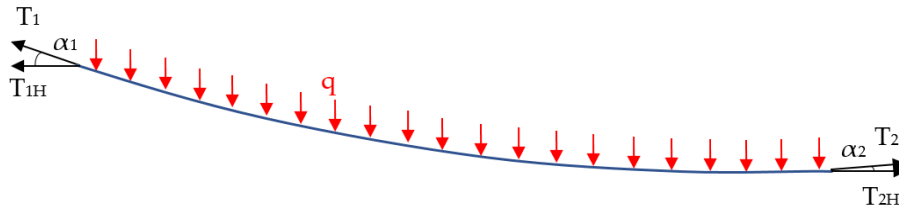
Figure 5.44: Equilibrium at each cable.

5.3.2. Only gravitational load

The results are reported below:

Tower	Tran. Load [kN]	Long. Load [kN]	Vert. Load [kN]	Tension 1 [kN]	Tension 2 [kN]
21	0.0	0.0	9.6	31.4	30.2
22	0.0	0.0	19.6	31.1	31.0
23	0.0	0.0	13.6	31.1	29.9
24	0.0	0.0	13.9	30.4	29.3
25	0.0	0.0	13.3	30.6	29.4

Table 5.6: Conductor cable forces according to analytical solution.

Tower	Tran. Load [kN]	Long. Load [kN]	Vert. Load [kN]
22	0.0	0.7	20.5
23	0.0	0.3	12.8
24	0.0	0.6	13.1
25	0.0	-0.2	12.4

Table 5.7: Conductor cable forces according to *PLS-Cadd* [10].

Tower	Tran. Load [kN]	Long. Load [kN]	Vert. Load [kN]	ΔFv to analytical [%]	Tension 1 [kN]	Tension 2 [kN]
21	0.0	0.4	9.0	-6.3%	29.1	29.5
22	0.0	-0.2	19.8	1.0%	30.6	29.7
23	0.0	0.1	13.4	-1.5%	30.3	28.8
24	0.0	0.3	13.7	-1.4%	29.6	28.2
25	0.0	0.0	13.0	-2.3%	29.8	28.4

Table 5.8: Conductor cable forces according to *Abaqus FEA*.

Having longitudinal mismatch on the order of just a few hundred Newtons, against a tension of tens of thousands, the line can be considered balanced.

5.3.3. Under wind load

As there was no reference cable deformed shape under wind loading, the comparison is only between the two finite element models:

Tower	Tran. Load [kN]	Long. Load [kN]	Vert. Load [kN]
22	16.4	0.3	27.4
23	18.9	-0.4	13.1
24	20.2	0.0	12.8
25	19.6	-1.7	11.8

Table 5.9: Conductor cable forces according to *PLS-Cadd* [10].

Tower	Tran. Load [kN]	Long. Load [kN]	ΔF_T to [10] [%]	Vert. Load [kN]	Tension 1 [kN]	Tension 2 [kN]
21	18.4	1.3	-	7.0	51.7	49.2
22	17.2	-1.1	4.9%	25.3	52.6	50.1
23	19.6	-0.3	3.7%	13.6	52.9	50.4
24	18.7	0.0	-6.4%	13.6	52.7	50.2
25	20.3	-0.7	3.6%	12.6	53.5	50.9

Table 5.10: Conductor cable forces according to *Abaqus FEA*.

The results match with 6% of error, there might be some minor difference in the two model cable shape. As it is not possible to have certainty on which model is built with larger error, or the real cable shape at the moment of the collapse, the line model can be considered verified.

5.4. Tower FE model

The purpose of this model is to estimate the ultimate load capacity of the structure under the analyzed load cases, thus being able to reproduce the complete structural characteristic.

The tower *FE* Model in Abaqus has been built up starting from the technical drawings provided by the *SwissGrid*.

As the masts in the collapsed line were built with minor differences, tower number n23 (the second from the top of the escarpment) was chosen, the one that contains the most recurring elements from all the others, the tallest, with the largest wind facing area (thus the largest force applied and resulting momentum at the basement), and the only one with strongly uneven legs length.

As a result of the previous analysis in Chapter 4, there are two feasible options in modeling large structures: *Beam* or *Shell+Beam* elements.

The *1D beam* configuration is however not free of complications: stress concentration in the area of *beam* element intersection halts the convergence of the solution, mainly due to the complexity of load sharing between elements connected to the same node in which a plastic hinge is forming, and the non-uniqueness of the bifurcation mode in this specific scenario.
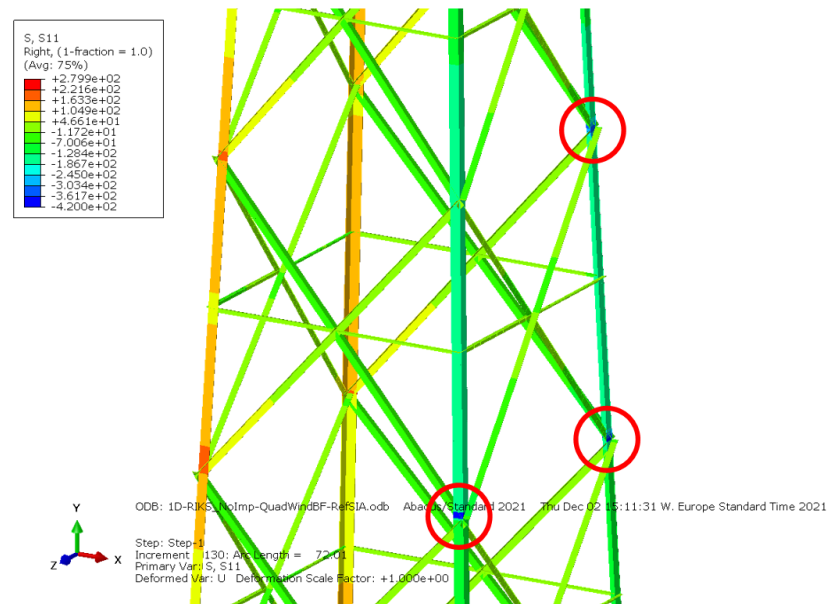
Figure 5.45: Local yield at intersections (plastic hinge), that can reduce convergence.

This kind of issue was not present in the models analyzed before, as the buckling modes superimposed on the entirety of the structure provided a more guided failure mode. In such large model, the principal buckling modes are localized in a few key areas, while in load-displacement analysis multiple concurring failure spots can appear all over the structure.

The problem cannot be easily resolved via mesh refinement, as it increases the number of elements undergoing plastic deformation at the intersection, worsening the problem. Improvements in solution stabilization can be made:

- decreasing the number of elements in the member (up to a single element), sacrificing solution accuracy.
- dissipative effects introduction into "*Static, General*" procedure, as it assures the reach of a converging solution, however in exchange of reduced solution accuracy. The other way is to use *"Dynamic, Implicit"* or *"General, RIKS"*, as these effects are already built into the solver by default, without compromises.
- slightly change the material model, to avoid instantaneously large displacement when yield limit is reached, by adding slight inclination to the curve.

In order to be conservative according to failure analysis, the *Shell+Beam* model with rigid connections was chosen, as it has consistently overestimated the results in Chapter 4.

The hybrid model is built with main legs made with *shell* elements, and diagonals and horizontal braces made with quadratic *beam* elements. The upper part (above the lower arms) is simply made of *beam* elements, as it has been proven not to be as critical.

Moreover, it appears to be a more promising trade-off, improving on the local instability being able to simulate accurately what happens at the diagonals attachment points.
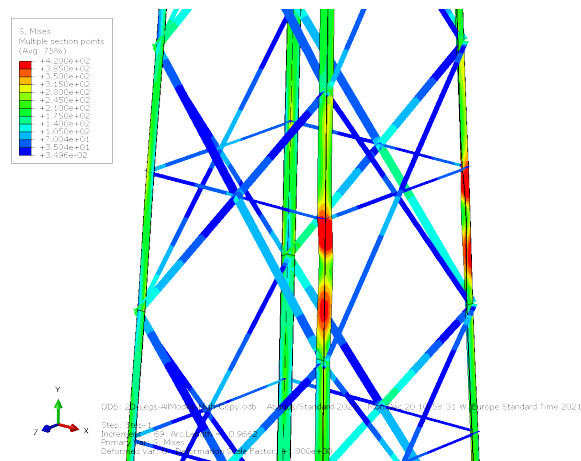
Figure 5.46: No local yield at intersections if it is modeled with *Shell* elements.

Note that neither of the two presented models contains load eccentricity, as the *beam* elements lay in the same plane as the two flanges of the leg's angle section. This effect might play a role in the structural capacity.
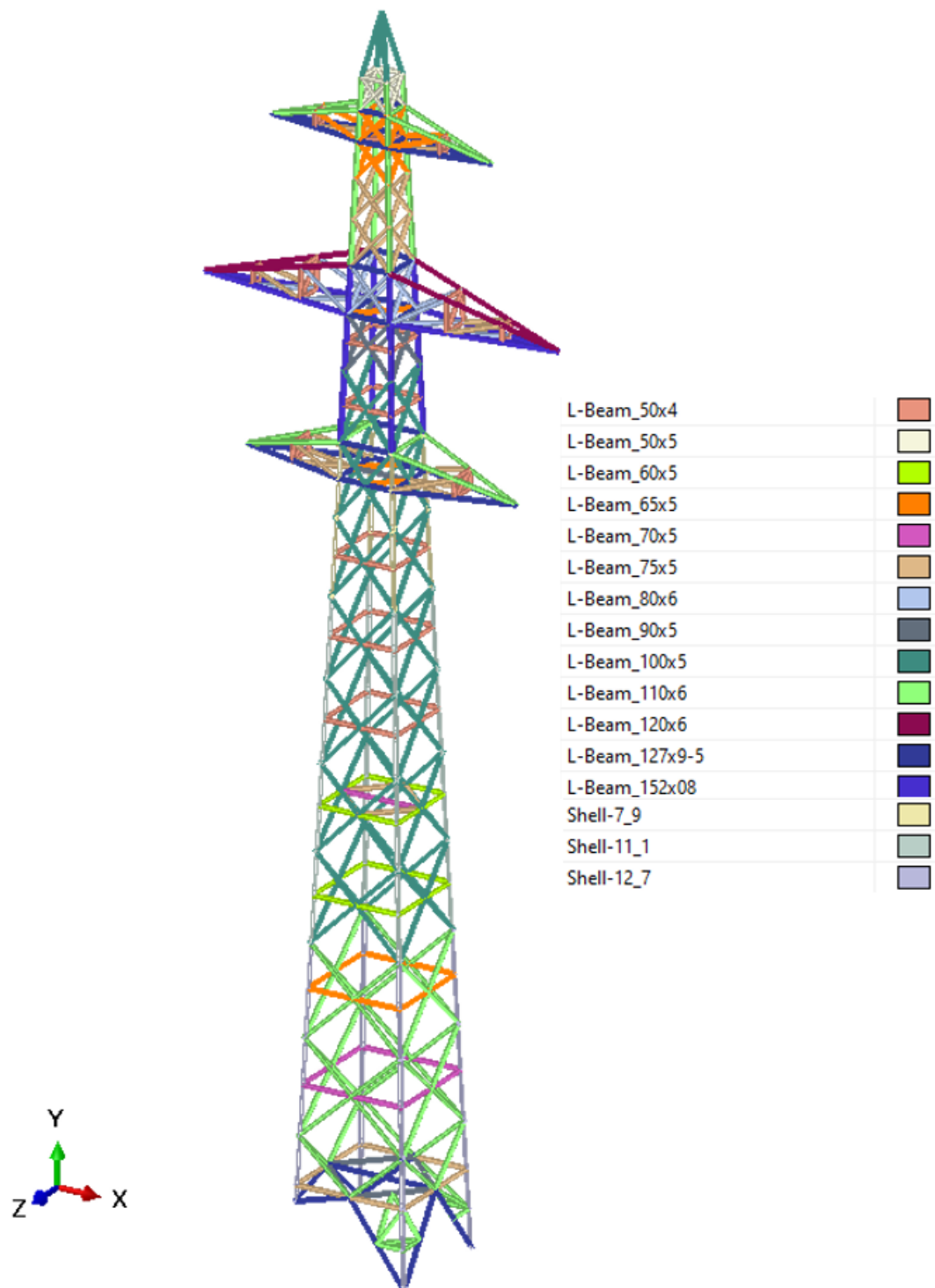
Figure 5.47: Hybrid *shell* and *beam* elements model.

5.5.   Linear Buckling Analysis (LBA)

The initial *LBA* on the tower is performed in order to localize potential failure points on the structure, identify the most critical failure direction and provide buckling imperfections.

As it is a quicker and more practical procedure, it is suited for finding which wind direction is the most unfavorable for the structure, even though it does not provide the ultimate load of the structure, but only the onset of instability.

This can be achieved by creating a series of load cases in MatLab and via setting up an Abaqus Macro function that iteratively copies the model and changes the force direction and magnitude.

Gravity and vertical cable load are applied as a dead load in a pre-loading step, and the wind load is then used as a perturbation (both on the structure and the connectors).

The result from this analysis is displayed in the following polar plots, depending on the wind approaching angle:
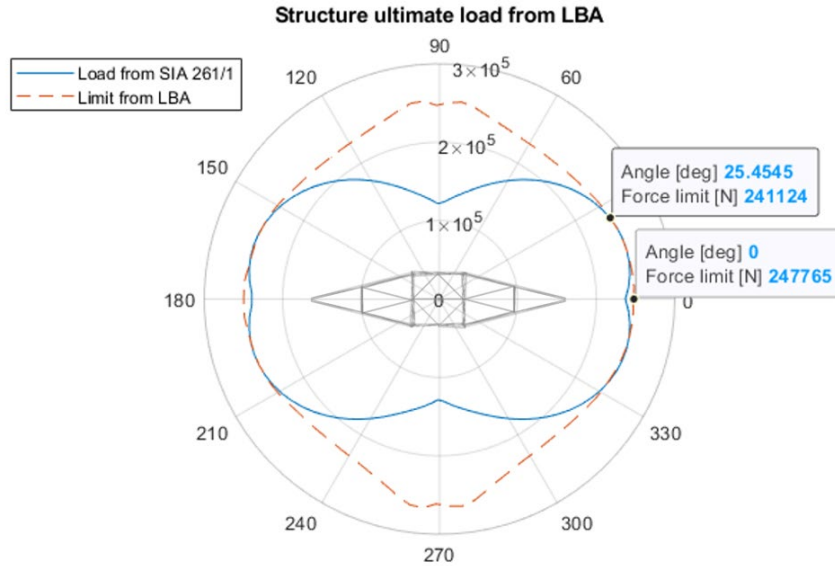
Figure 5.48: Instability load as from *LBA*, in terms of total load, against *SIA 261/1* loadcase.

Another way to look at the results is to see them in terms of structure utilization:

$$Utilization\ (\vartheta) = \frac{F_{SIA\ 261/1}(\vartheta)}{F_{ultimate,LBA}(\vartheta)} \tag{5.34}$$
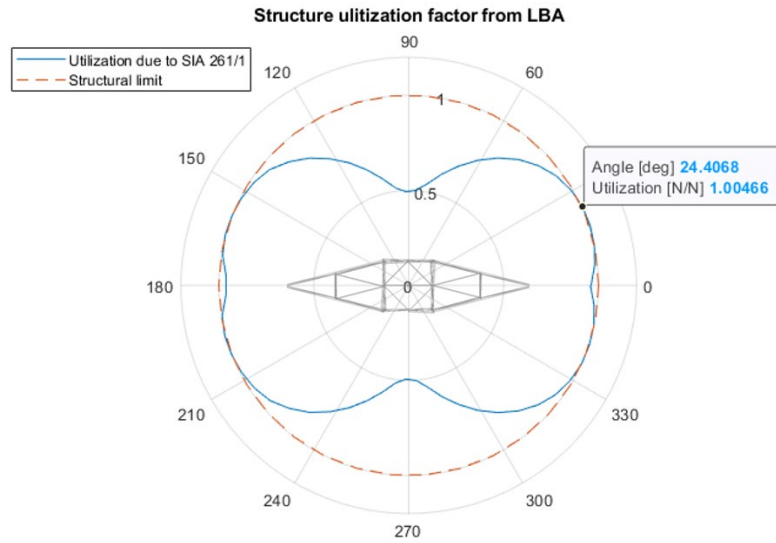
Figure 5.49: Instability load as from *LBA*, in terms of utilization factor, against *SIA 261/1* load case utilization.

Few observations can be drawn from this analysis:

- although the basement legs in tower n23 are different in length, there is negligible ultimate load variation asymmetry.

- the unfavorable wind direction is between 10° and 25° to the transverse direction, in which the wind forcing is equal to the *LBA* instability load.

- the failure mode is always focused between the 7th and 8th levels of the tower:

(a) Mode 1, 0°

(b) Mode 2, 0°
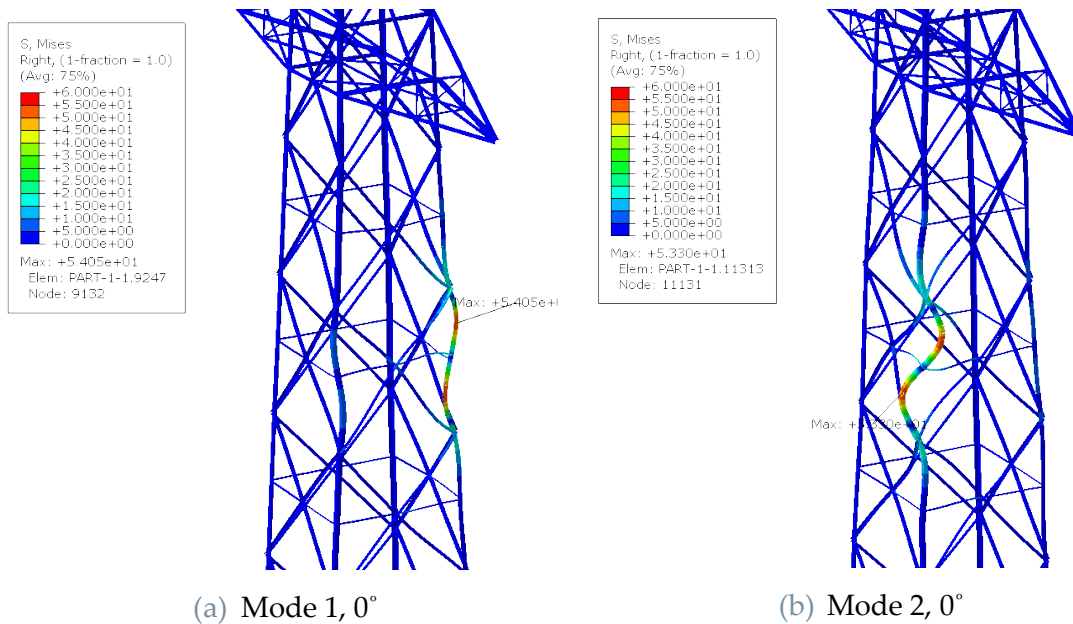
Figure 5.50: Result of *LBA*, transverse wind forcing (0°), scale factor=500.

(a) Mode 1, 24° (b) Mode 1, 96°
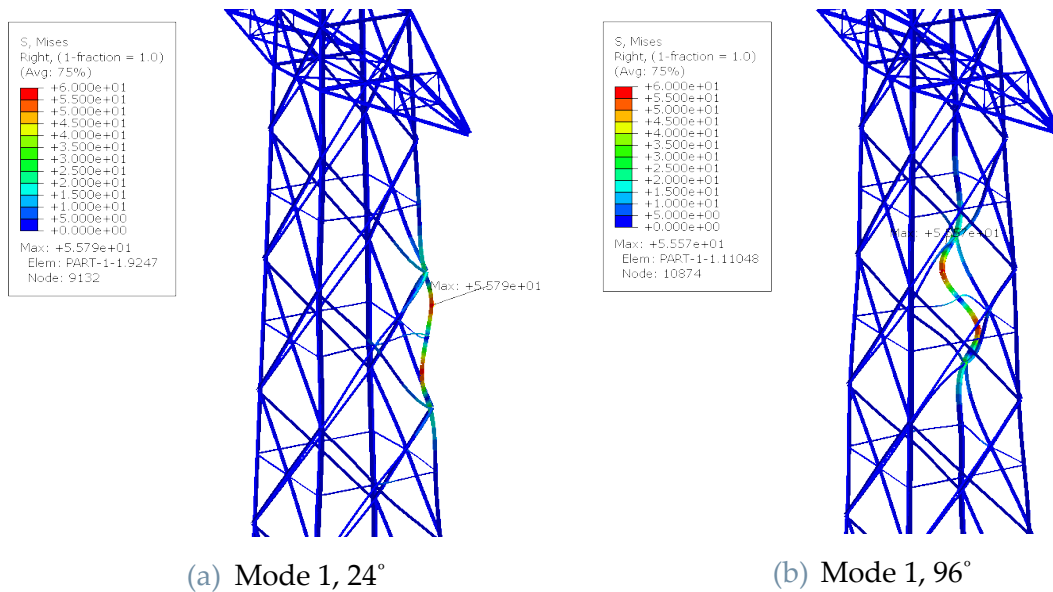
Figure 5.51: Result of *LBA*, wind acting at 24° and 96°, scale factor=500.

If further eigenvalues are analyzed, another possible failue mode localized on the second level can be seen:

(a) Mode 3, 0° (b) Mode 4, 0°
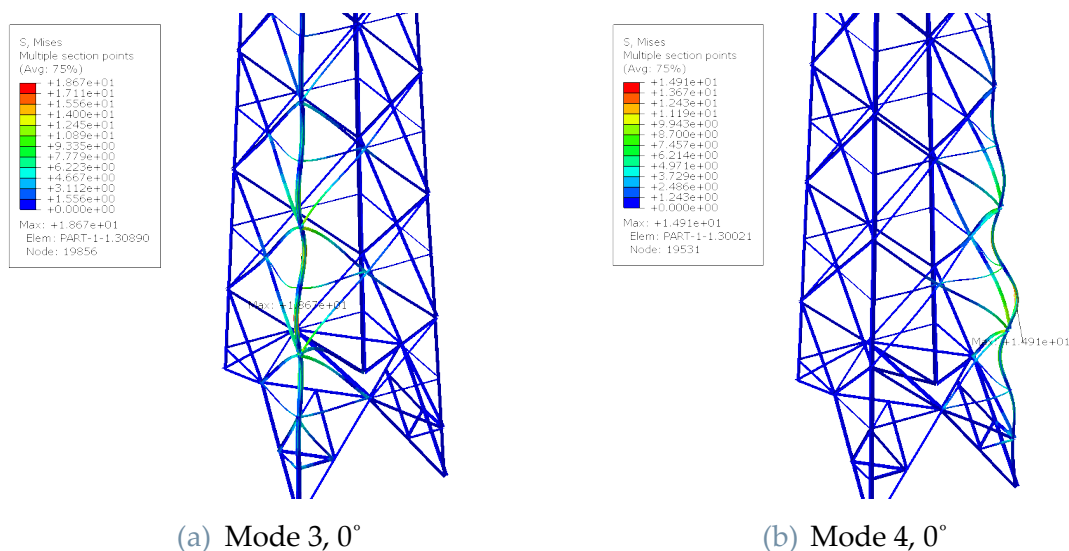
Figure 5.52: Result of *LBA*, transverse wind forcing (0°), scale factor=500.

However, the eigenvalue for these modes is higher, around 2.14 (equivalent to a total force of 502.68 kN).

Other two load cases have been analyzed, under purely transverse wind conditions (0°), in order to see what load is the more unfavorable on the structure:

1. wind on structure (119.9 kN) as dead load (cable load as perturbation);

2. wind on the cables (117.1 kN) as dead load (structure load as perturbation).

In both these cases the failure mode is also localized in the same spot (7th level) and the total ultimate load is quite close:

Case	Perturbation	Perturbation Magnitude [kN]	1st Eigenvalue from LBA (Max/Applied)	Max Total Load [kN]
ref	Total load	237.1	1.04	247.76
1	Only connector load	117.1	1.14	253.39
2	Only wind on structure	119.9	1.08	246.59

Table 5.11: Maximum load according to *LBA*.

The ultimate load capacity does not change drastically between the analyzed cases, but the wind load on the structure appears to be slightly more critical in the sense of an *LBA*.

SIA 261/1 load of 237.1 kN has been taken as a reference also fur further analyses.

5.6. Load capacity and model imperfection sensitivity

G. Piskoty et al. [48] and J. Wang et al. [18], which studied the effects of superimposed buckling imperfections the collapse of a roof and a steel lattice tower due to structural instabilities, as well as the analysis developed in the previous Chapters 2 and 3, pointed out that the sensitivity to imperfections can significantly affect the ultimate load capacity of the structure.

Section 5.3.3, Eurocode 1993-3.1 [4], specifies a formula for standard imperfections to be adopted during analysis:

$$e_0 = \alpha_m \cdot L/500 \tag{5.48}$$

$$\alpha_m = \sqrt{0.5 \cdot \left(1 + \frac{1}{m}\right)} \tag{5.49}$$

In which m is the number of members of the bracing system, in the analyzed case m=668, thus $\alpha_m = 0.7076$ and $e_0 = L/706.5$.

This imperfection amplitude is used for all the following imperfections.

The ultimate load is estimated using a *RIKS* procedure, in which gravity and vertical cable load are applied as a dead load in a pre-loading step, and the lateral wind load is then scaled according to the load-displacement curve path.

5.6.1. Superimposed buckling imperfections

In order to specifically trigger a single failure mode, as the buckling mode deformation is localized (applying the multiple ones simultaneously would not show a combination), the buckling modes previously found in the *LBA* are superimposed:

1) Buckling modes 1 and 2 (7th level), amplitude 3.06mm ($e_0 = L/706.5$ L=2.17m);

2) Buckling modes 3 and 4 (2nd level), amplitude 3.8mm ($e_0 = L/706.5$, L=2.17m);

3) Buckling modes 3 and 4 (2nd level), amplitude 8.96mm ($e_0 = L/300$, L=2.69m);

5.6.2. Missing structural elements

IED [10] pointed out that the lack of structural capacity of some reinforced elements might be crucial to the structural capacity.

S. D. Eslamlou et al. [49], as well, analyzed the impact of element removal on the tower capacity.

The following configurations were analyzed:

CASE1:
missing of 2 braces at 5th level;

CASE2:
missing of 5 braces at 5th level;

CASE3:
missing of 2 braces at 1st level;

CASE4:
missing of 8 braces at 1st level.
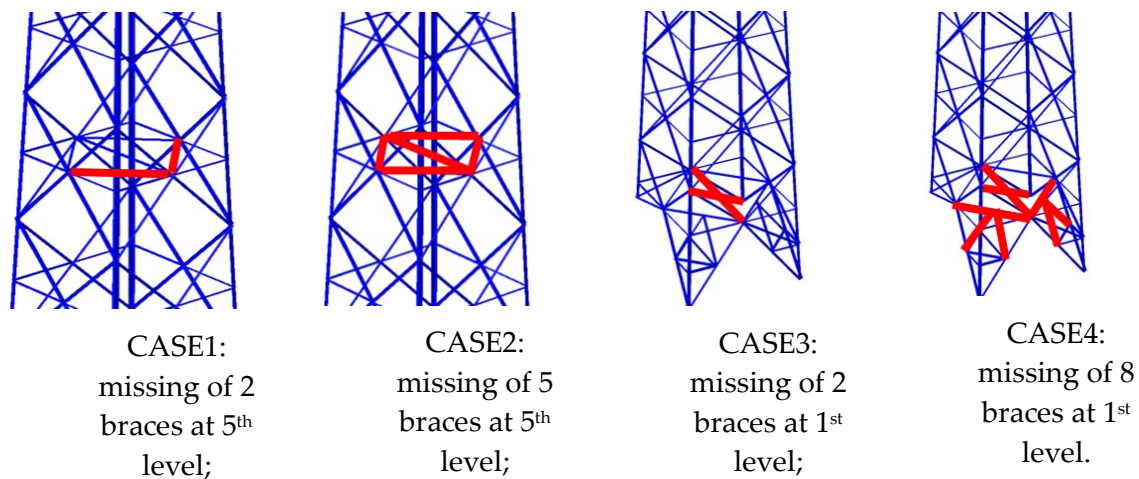
Figure 5.53: Removal of structural elements displayed.

RIKS analysis requires buckling modes 1, 2, 3 and 4 to be superimposed (magnitude of 1.6mm, $e_0 \approx L/1400$), in order to guide the failure, improving convergence.

5.6.3. Support displacement

This type of imperfection can be quite harmful to the structural integrity, as proved by W. M. Wang et al. [16] and M. Jian et al. [50], who respectively analyzed, via numerical methods, the effect of displacement at tower basement supports.

The displacement value range used in the mentioned articles is on the order of tens of centimeters, due to ground foundations movement over time.

In the case of the studied failure, the foundations were made of stiff concrete, carefully replaced after the 1987 event. A small magnitude in the order of a few centimeters can still however be present and being overlooked.

Figure 5.54: Foundations of mast n25, unaffected by the collapse (source *Swissgrid*).

Three hazardous cases have been analyzed and compared to the pristine structure:

CASE1: single support displacement, vertical and lateral of 15mm;

CASE2: two supports move downward and sideways of 15mm;

CASE3: the two supports move inward and down by 15mm.
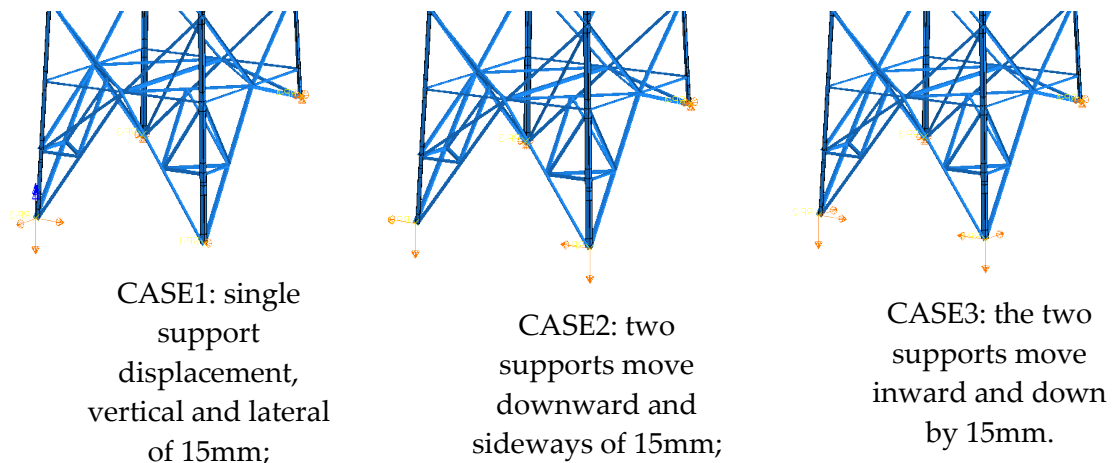
Figure 5.55: Support movement cases displayed.

As in the previous case, buckling modes 1, 2, 3 and 4 (Figure 5.50 and 5.52) were superimposed with a magnitude of 1.6mm.

The stress state after application of the displacement can be considerably high, reaching, in the worst case, a peak of around 190 MPa in some elements (Figure 5.56).
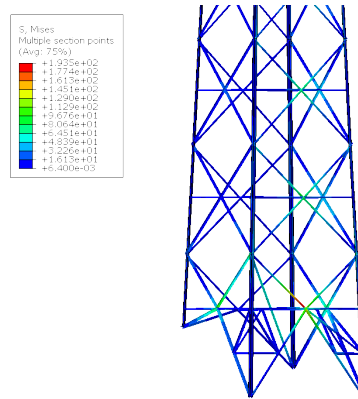
Figure 5.56: Stress state after CASE 3, scale factor of 5.

5.6.4. Conductor load unbalance

The possible longitudinal load unbalance of the line can potentially cause a torsional
moment on the line or an increase of the load:
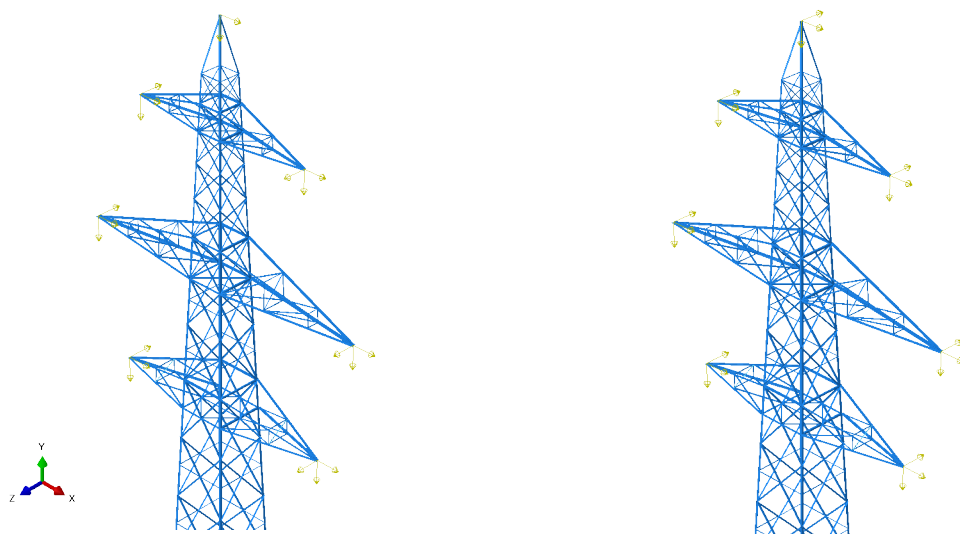
(a) CASE1 and CASE2: Torsional effect in
y: 2 kN in opposite directions at each
connector, for a total torsional moment
of 100 kNm; CASE 2 without 5th level
reinforcements.

(b) CASE3: Bending effect in x: 2 kN
in the same direction at each
connector, for a total longitudinal
force of 16 kN.

Figure 5.57: Torsional and bending effects due to longitudinal load unbalance.

Buckling modes with a magnitude of 1.6mm were applied as in the previous case.

5.6.5. Imperfection sensitivity analysis results

The results of the imperfection sensibility are summarized in the following Table
5.12, as absolute and relative (with respect to *SIA 261/1* load of 237.1 kN) magnitude.

Case	Load in transverse dir. [kN]	Load capacity (applied/ref.) [%]	Position of the failure [level n.]
Buckling case 1	313.9	132%	7th
Buckling case 2	292.9	123%	2nd
Buckling case 3	244.0	103%	2nd
Missing el. case 1	321.3	135%	7th
Missing el. case 2	320.9	135%	7th
Missing el. case 3	292.9	123%	2nd
Missing el. case 4	288.2	122%	2nd
Support displ. case 1	246.8	104%	2nd
Support displ. case 2	282.4	119%	2nd
Support displ. case 3	314.9	133%	7th
Unbalanced case 1	324.0	137%	7th
Unbalanced case 2	323.7	136%	7th
Unbalanced case 3	278.0	117%	2nd

Table 5.12: Maximum load according to *LD* analysis. The reference is *SIA 261/1* value in Table 5.5 (237.2 kN of total force).
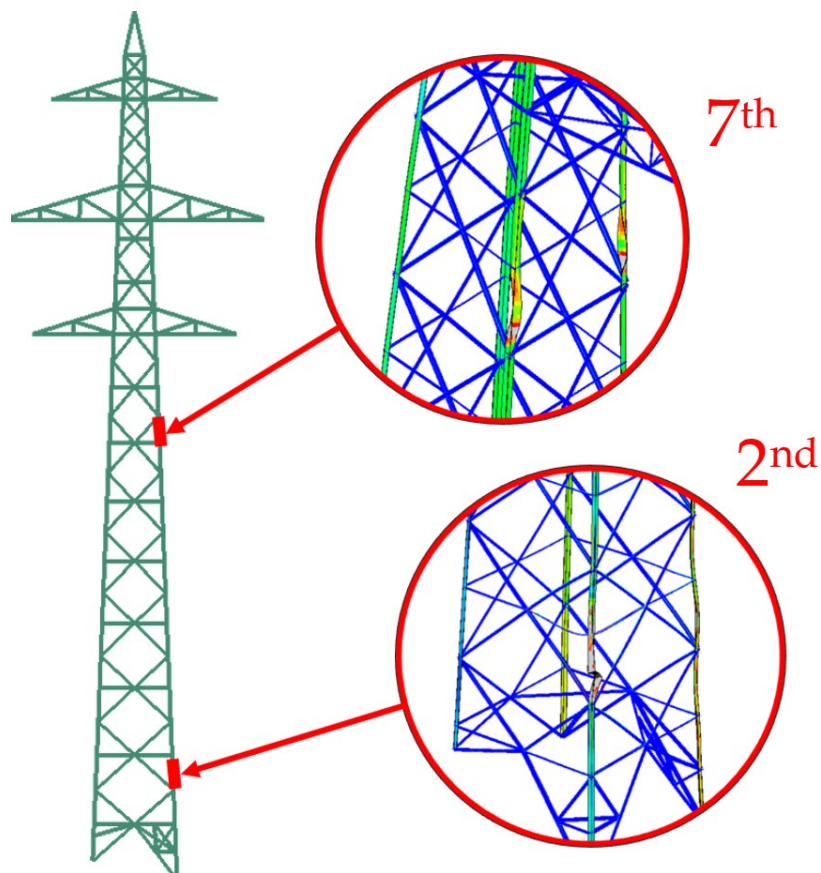
Figure 5.58: Recurring failure positions highlighted.

It is possible to draw the following conclusions:

- The failure consistently occurs in the 7th or 2nd level. As imperfections are introduced in the 7th level, the ultimate load ranges from 1.32 to 1.37 times the reference load. The load capacity at 2nd level appears to be even more sensitive to imperfections, ranging from 1.03 to 1.23 times the reference. Particularly unfavorable is the displacement at the support of one single leg.

- The lack of structural reinforcements does not appear to cause any variation to the load capacity of the tower, even if coupled to other imperfections (unbalanced, case 2).

- The failure is inelastic buckling driven, only a small portion of the section is plasticized when the ultimate load is reached.

5.7. Post-buckling analysis

The tower post-buckling behavior, according to the *RIKS* procedure (reference Figure 5.59), is not monotonic, as the load is not aligned to the buckling elements.

This means that the *Arch-Length* method does not have a single bifurcation path anymore for the remaining elements of the section, resulting in solution divergence.
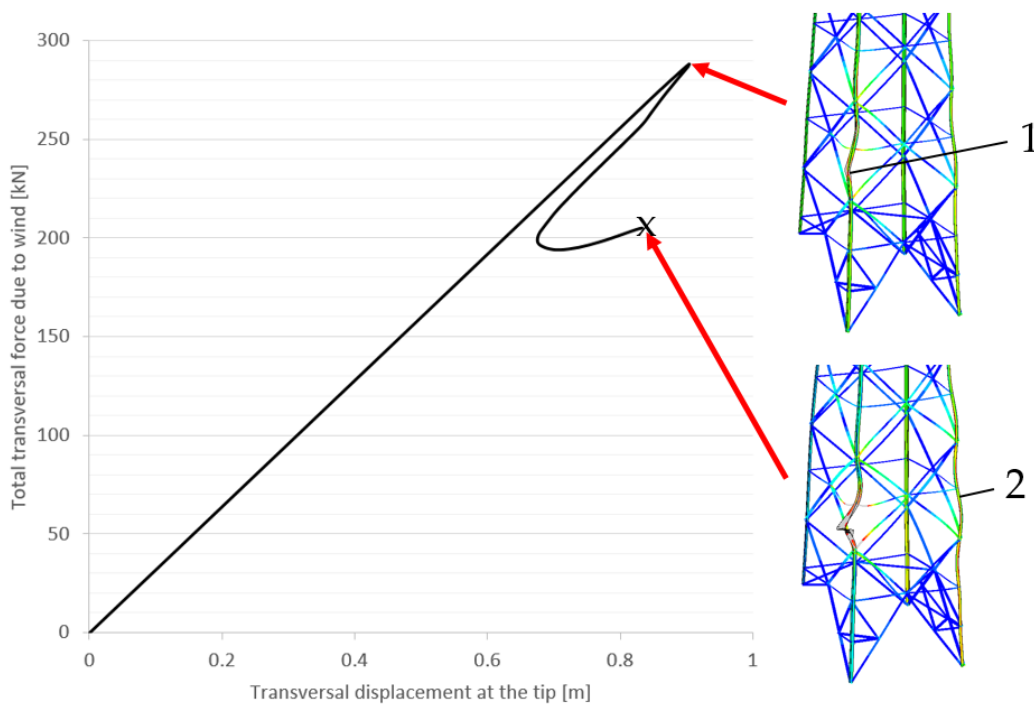
Figure 5.59: Load - displacement curve from Missing el. case 4 as an example. It is possible to notice the two legs buckling sequence. Note that in the real case the two would fail almost simultaneously, as the force applied to the structure does not decrease.

Therefore, to obtain a more stable estimation of the remaining capacity after the first elements had failed, a pushover analysis has been carried out in a model in which the 7th level these elements are removed.

The tower is able to sustain itself under its own weight, but, as expected, the wind load-bearing capacity falls from 313.1 kN (reference *Buckling case 1*, Table 5.12) to 39.4 kN (around 87.4% reduction), thus the sudden collapse of the structure.

If the buckled elements are instead removed from the 2nd level, the tower is not able to withstand even its own weight.

It is possible to say that:

- The tower loses almost all the load-bearing capacity when the first elements fail.

- In the post-buckling phase, the failure sequence remains localized, leaving the rest of the tower pretty much intact and unaffected.
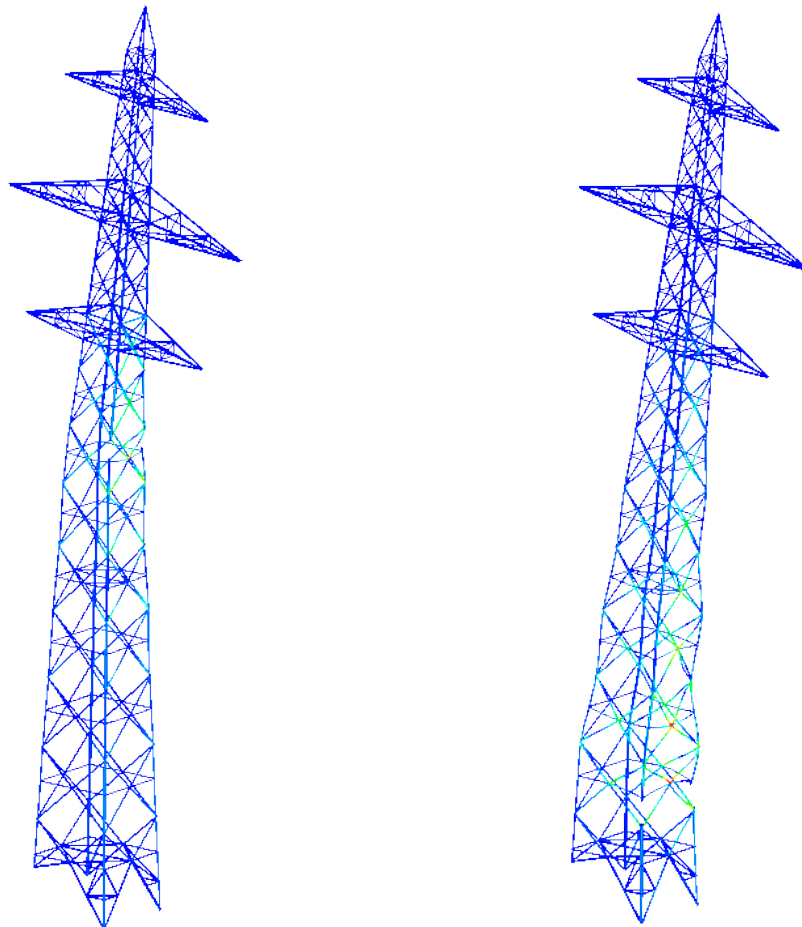
(a) Missing elements at 7th level   (b) Missing elements at 2nd level

Figure 5.60: Post-buckling deformations, scale factor 10.
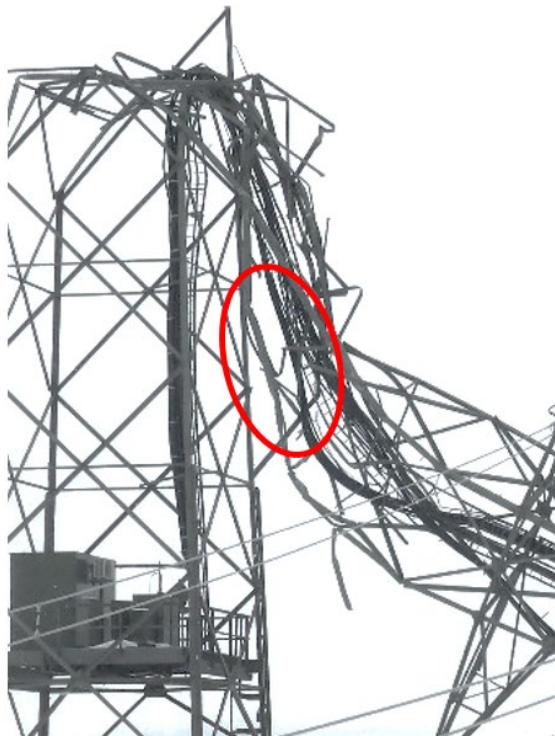
(a) Failure at midheight, tower n22, 7th level highlighted.
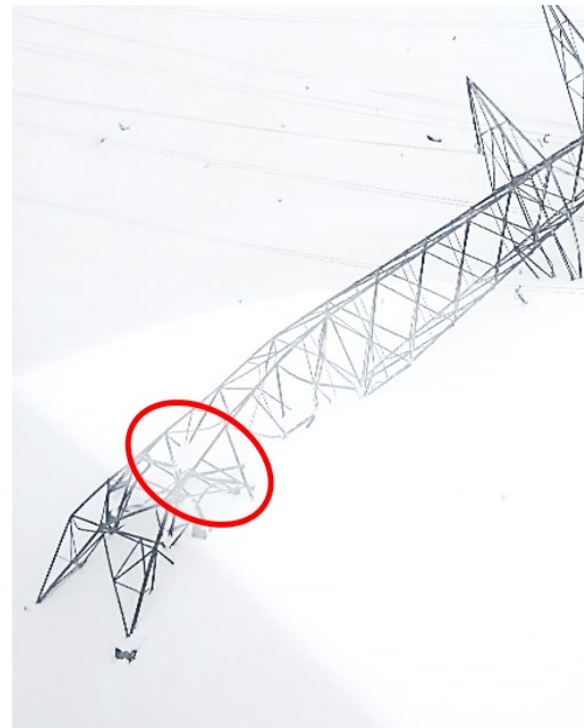
(b) Failure at the base, tower n23, 2nd level highlighted.

Figure 5.61: Towers as found after the event. Notice the failure propagates downwards in the case of tower n22, as well as in tower n23, hindering the capacity of the tower, which suddenly collapses.

5.8. Brief analysis of tower n22

Up to this point, tower n23 was the one considered for the analysis, as it well represent the other n24 and n25 in terms of load case and shape.

Although having a similar geometry as well, n22 has an additional vertical force on the conductor connectors, that might make a difference:

Tower	Tran. Load (kN)	Long. Load (kN)	Vert. Load (kN)
n22	17.2	-1.1	25.3
n23	19.6	-0.3	13.6

Table 5.13: Comparison of cable forces under wind load according to *Abaqus FEA*.

Note that the wind load applied to tower n22 is lower than in n23, because the structure is around 5m shorter and the neighboring cable span a total of 572m against 693m (18% longer for tower n23).

Tower	Wind force on cables (kN)	Wind force on structure (kN)	Total wind force (kN)
n22	105.26	110.88	216.14
n23	119.95	117.14	237.09

Table 5.14: Reference load according to *SIA 261/1*.

Moreover, being the one identified as the origin of the collapse from most of the parties involved in the study ([10]), it is interesting to see how the margin compares with tower n23.

Mind that the modeled tower n22 lacks important reinforcements and auxiliaries structures (antennas and radio equipment) present in the real counterpart, which might increase the wind loading and the load capacity.

The results of the initial *LBA* are quite close to the ones of the other towers, both in terms of eigenvalue and eigenmode, as the failure occurs at the 7th level in the same manner and with a similar margin from the perturbation value. However, the other Eigenmodes were not located at the 2nd level, but rather at the 10th (Figure 5.62):

Tower	Failure position [n. level]	Eigenvalue from *LBA* [max/applied]	Max. total load [kN]
n22	7th	1.025	221.5
n22	10th	1.744	376.9
n23	7th	1.045	247.7
n23	2nd	2.135	502.2

Table 5.15: Results from *LBA*, with perturbation loads from *SIA 261/1*.
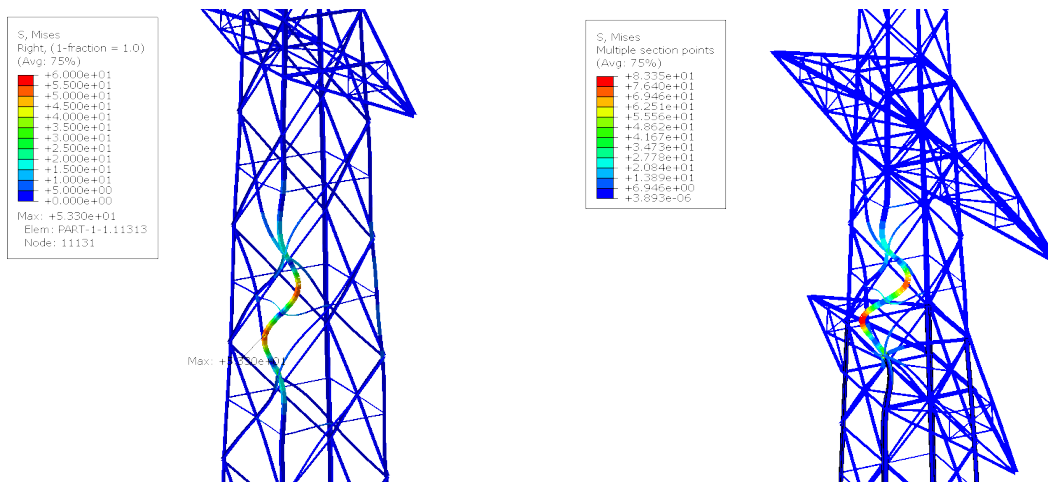
(a) Mode 1, failure at 7th level

(b) Mode 3, failure at 10th level

Figure 5.62: Result of *LBA* for tower n22, transverse wind forcing (0°), scale factor=500.

A *RIKS* analysis has been performed, with introduced first mode buckling imperfection of $e_0 = L/706.5$ ("*Buckling case 1*" analyzed before), and subsequently a post-buckling analysis at the 7th level. The results are compared in terms of absolute and relative values with the ones from tower n23 in Table 5.16. Tower n22 and n23 relative values refer to *SIA 261/1* loads of 216.1 and 237.1 kN respectively (Table 5.14).

Case	Tower	Load in transverse dir. [kN]	Ultimate limit (applied/ref.) [%]	Failure position [level n.]
Buckling case 1	**n22**	274.3	127%	7th
Buckling case 1	**n23**	313.9	132%	7th
Buckling case 2	**n23**	292.9	123%	2nd

Table 5.16: Ultimate wind load from *LD* analysis, reference loads according to *SIA 261/1*.

Case	Tower	Load in transverse dir. [kN]	Load capacity reduction (post-buckling vs buckling)
Post-buckling at 7th	**n22**	15.9	-94.3%
Post-buckling at 7th	**n23**	39.4	-87.4%

Table 5.17: Ultimate load in post-buckling analysis.

In terms of total wind load applied, the transverse load-bearing capacity of tower n22 is 10.6% lower in *LBA* and 12.2% in *LD* analysis than of tower n23, mostly attributed to the extra vertical cable load.

If the relative margin is referenced instead, the relative loads are within a 3% difference in both analysis types (for the same failure mode), which is to be expected as transmission line towers are purposely designed with similar safety margins.

The fact that the structures fail in the same position in both cases, hints that could be the point with the lowest structural surplus.

5.9. Comparison with IED report

IED in [10] have analyzed the structure in terms of single-member "*utilization factor*", based on member design limits (buckling, section yielding onset, member ends and bolted joints capacity).

The elements with the largest utilization were initially localized in the lower part of tower n22 (Figure 0.15). Just a few diagonals at the 4th or 5th level had utilization over 100%. Therefore, their collapse hypothesis considered these elements to be the first

to fail, which led to an increase of utilization in the main legs at the 4th level (from a base of 50%, up to 204%), causing the structure to crumble (Figure 5.63).

However, this hypothesis does not account for possible damage during collapse to members underneath the first failing level, which had supposedly remained perfectly intact.
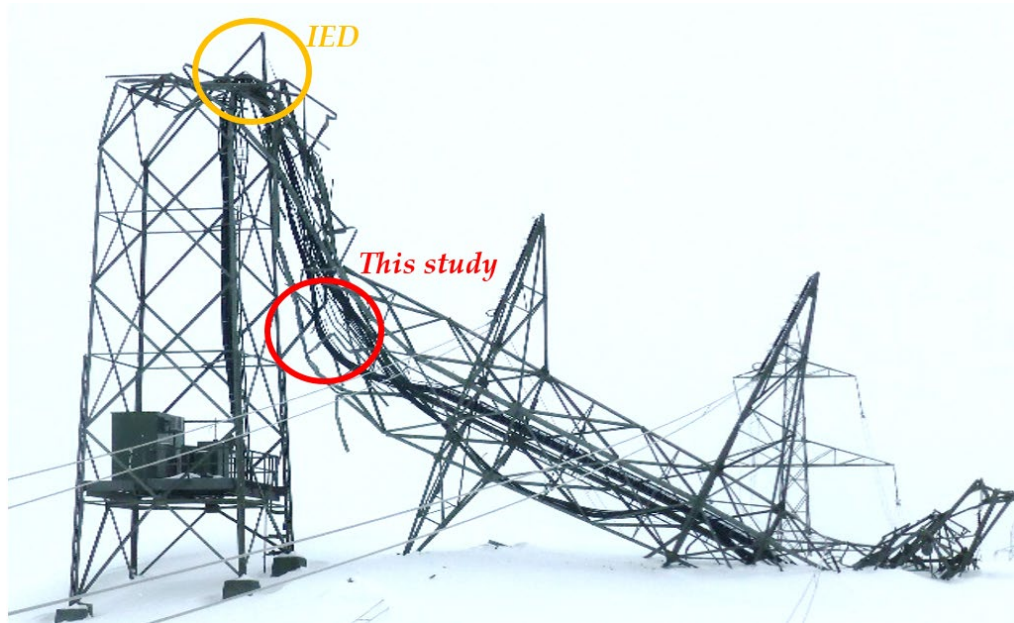
Figure 5.63: Failure positions in tower n22 highlighted, according to *IED* [10] (yellow) and this study (red).

The resulting margin with respect to the design values (*SIA 261/1*) is close to the one calculated by the *LBA* and *RIKS* analysis (Figure 5.64), for both towers n22 and n23. However, the members with the largest utilization are not located in the same area!
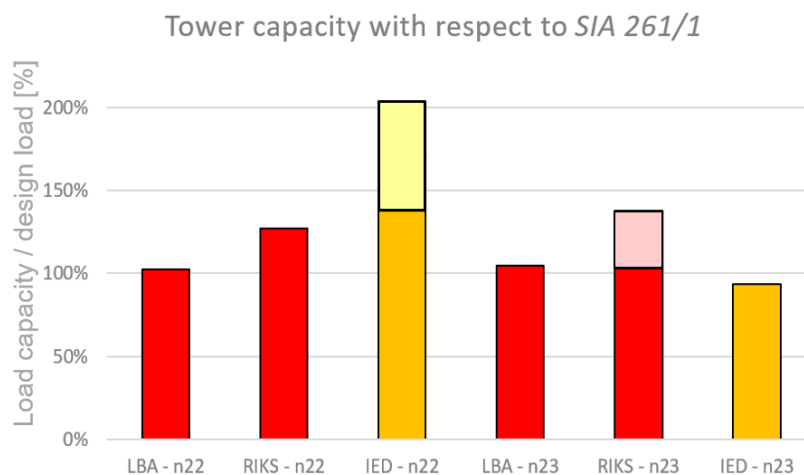
Figure 5.64: Towers load capacity, according to *IED* [10] (yellow) and this study (red). Lower and upper estimates are shown for tower n22 (*IED*) and n23 (reference Table 5.12).

5.10. Conclusive discussion on the results

Viable wind load models have been compared and a load case for the line has been estimated. The two towers of the line have been subjected to a *pushover* analysis to determine their load-bearing capacity and safety margin in that condition.

It is possible to say that:

- The towers have limited capacity margin (maximum of 37%) with respect to the reference load case *SIA 261/1*, which proved that the towers were close to their limit. A failure due to wind only can be plausible.

- Both towers have no safety margins if compared with *Eurocode* standards (which have considerably higher total load than the *SIA 261/1,* since they account for an additional dynamic component).

- The results from *LBA* and *RIKS* analyses are close to the utilization factors calculated by *IED* for the same load case ([10]). Their failure position, however, was located more towards the base of the towers, in contrast to the state the structures were found after the event. Moreover, as it was demonstrated in Chapter 1 and 2, design standards do not always match the member capacity nor the stability limit, as the stress state in lattice structure members is extremely end-restrains dependent.

- The structure is very sensitive to specific imperfection modes, such as buckling or support displacement. The applied imperfections, however, do not change the main failure modes, which are located in the same two spots of the 2nd and 7th levels in both towers n22 and n23. Particularly unfavorable is the displacement at the support of one single leg, while the missing structural reinforcements do not affect the load capacity.

- The load capacity calculated by the *RIKS* analysis is around 30% higher than the values from *LBA*. Section yielding or redundant members might increase the capacity over the stability limit.

- The failure is inelastic buckling driven: only a small portion of the section is plasticized when the ultimate load is reached.

- The tower loses almost all the load-bearing capacity when the first elements fail.

- In the post-buckling phase, the failure sequence remains localized, leaving the rest of the tower pretty much intact. The remaining damage found on the real towers could be attributed to the fall damage and contact with the ground.

6 Chapter six: Cascade of the transmission line

The other main objective of the study is to prove that a cascade is plausible, and to reproduce it, trying to estimate which of the towers has the highest probability of causing a cascade on the line.

The topic is not well documented in the literature, as the majority of the studies focus on the causes of a single tower failure.

Under the same load case as Chapter 5 (wind perfectly transverse to the line), to maintain a certain continuity, the feasibility of two possible line failure modes was investigated:

1) Cascade effect: line collapse due to dynamic load on the neighboring towers' through the conductors, measuring the overload at cable connectors on the rest of the line.
2) Collapse sequence: the other towers collapse in a second moment with respect to the first, due to reduction in load-bearing capacity caused by conductor force unbalance with a tower on the ground.

Collapse of the single towers and the cascade sequence have been simulated.

6.1. Line FE model

To simulate the failure of the elements, the model was subdivided in core levels and linked with connector elements, to which failure load can be assigned.

Each connector has set the failure load of the above level (Figure 6.1).

The contact of towers and cables with the ground was modeled as normal exponential spring, allowing small compenetration, and without any transverse action (frictionless), greatly improving simulation stability. The resulting downside is the loss of any sort of physical accuracy starting from the moment the tower or the cables touch the ground. However, the behavior after the contact is very dynamic and not very meaningful anyhow.

Another simplification lays in the fact that it was not possible to introduce any stiffness nor damping of the connector models, as it is complex to estimate with accuracy. Thus, when one fails, the other will behave as a simple spring

The simulations have been carried out using "*Dynamic, Implicit*" procedure, as it offer quicker computation if the simulation time is large, at expense of risking to miss low-frequency dynamics.

This trade-off was accepted since the quasi-static preloading steps to reach an equilibrium state under gravity and wind, last around 600s (10 min). During initial loading, the system, as it contains many free degrees of freedom, can easily undergo dynamic effects, such as cable galloping vibrations (longitudinally in the line).

The other limiting factor to this approach is the restriction from importing data, such as coordinates, out of connector elements, thus limiting the quick static preloading transferring to *Dynamic, Explicit* simulations across *Abaqus models* using "*restart*" or in "*initial condition*" functions.

6.1.1. Connector failure criteria
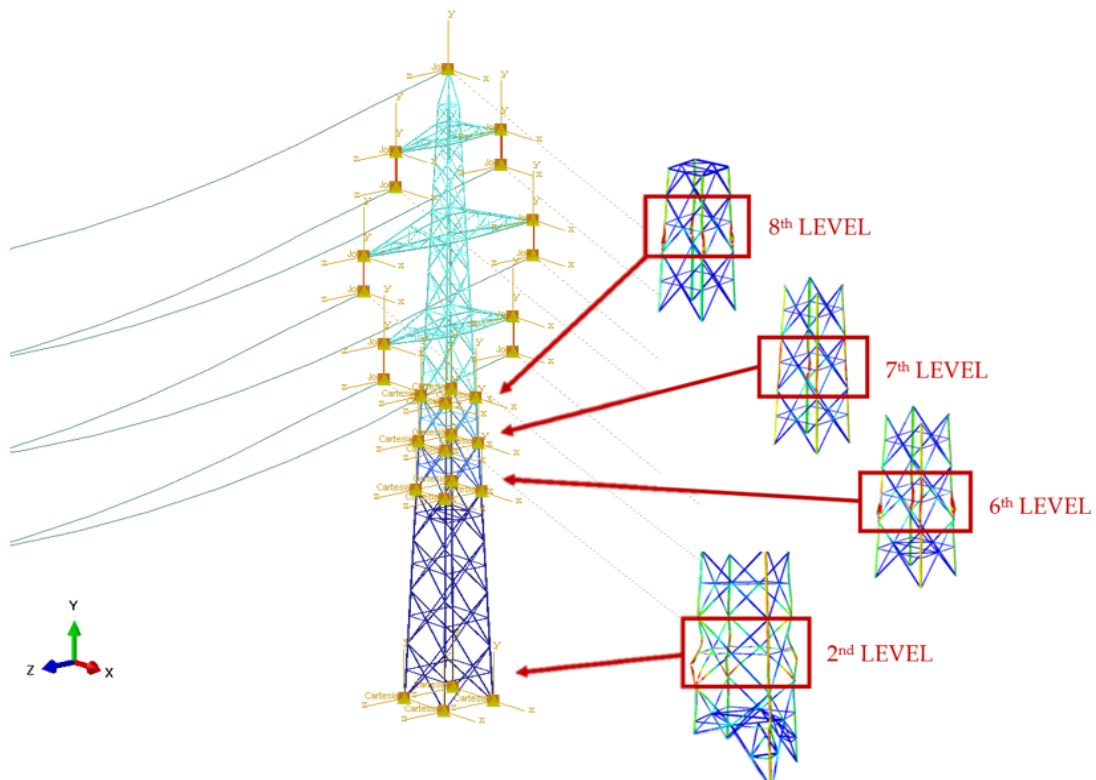
Figure 6.1: Tower n22 dissected into selected sections.

In *Abaqus 2021* the criteria for connector failure is a uniaxial force or momentum limit. However, the loading on the assembly components during collapse can become complex and multiaxial.

Several configurations were tested, also accounting for section yielding criteria under shear and bending moment. However, the failure appears to be purely buckling driven, even during the post-collapse, without noticeable difference whether or not these other criteria were implemented.

The connectors were modeled as *pinned* joints, coupling only the translational degrees of freedoms, as the bending bearing capacity of the members is nullified moment after the collapse.

The limit for the conductor connector and insulator is set at 110 kN, only under pure tension (according to their specifications), although this has never been reached.

The compressive limit is then found via substructure behavior simulation: the key levels, alongside the one above and one underneath in order to provide boundary conditions, are subjected to displacement-controlled compression.

A buckling imperfection of $e_0 = L/706$ was introduced to each level.
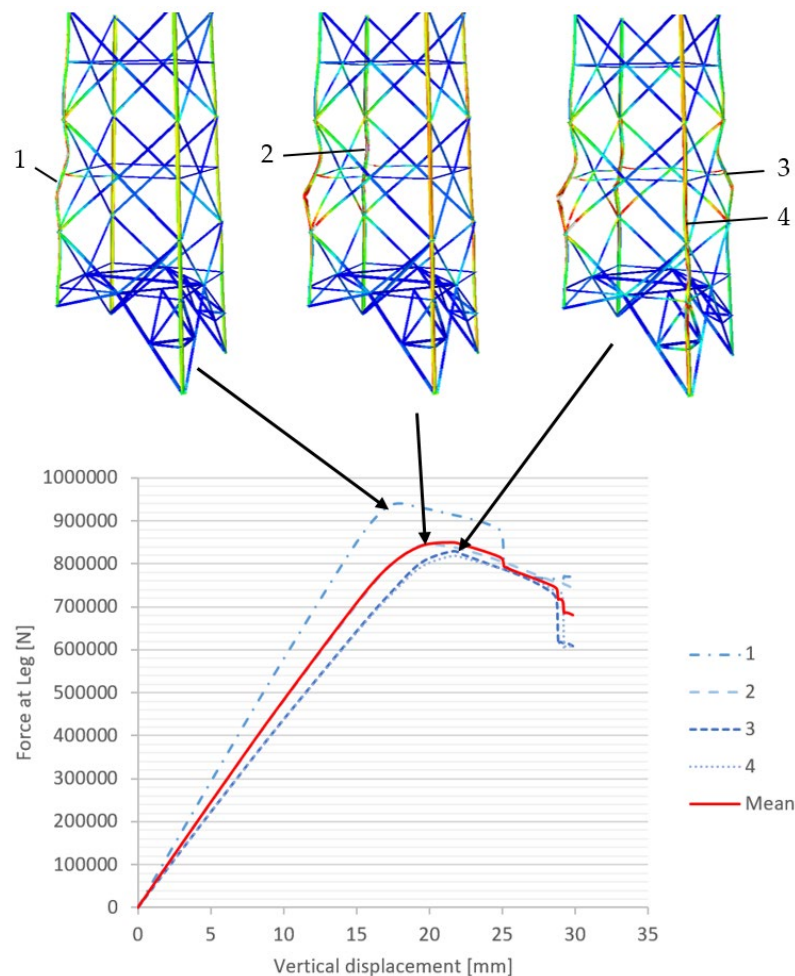
Figure 6.2: Load-Displacement curve of the 2nd level, tower n23.

The collapse at every leg happens almost simultaneously and the ultimate load estimation is straightforward, except for the 2nd level in tower n23, in which the buckling of each leg happens in a sequence, due to different leg length (Figure 6.2). In this very case, the chosen ultimate load has been assumed as the ultimate one for leg 1, and as the mean one for legs 2, 3, 4, to be a more conservative estimation in the sense of the failure analysis.

The limit under pure tension is set as the yield limit of the section.

The limit loads for each section are summarized in the following table:

Level	Failure load in compression [kN]	Failure load in tension [kN]
8th	580.6	982.4
7th	1006.1	1365.5
6th	1006.9	1365.5
2nd – tower n23	850.3 – 936.3	1553.8
2nd – tower n22	1227.9	1553.8
2nd – tower n24, n25	1252.2	1553.8

Table 6.1: Connector failure criteria at each level.

Note that tower n22 had undergone first levels reinforcement (addition of "butterfly profiles") to allow mounting of radio equipment and antennae, which was taken into consideration in the capacity study. Hence, the 2nd level might be sturdier than estimated.

Figure 6.3: Tower n22, reinforcements made at the basement level (yellow) and at the diagonals (red) [11].

6.1.2. Model validation

Each simplified tower is loaded until connector failure, and the failure position and ultimate wind load are compared to the one of the single tower model, to assure continuity between the two methods:

Model	Failure position [level n.]	Ultimate load tower model [kN]	Ultimate load line model [kN]	Error [%]
Tower n22	7th	274.3	313.3	+14.2%
Tower n23	2nd	292.9	272.4	-6.8%

Table 6.2: Failure load in the two towers, single tower and line models compared.

Even though they were built from the same premises, the two models show different behavior in comparison to the tower model. This hints that there might have been a more complex loading than pure compression of the member.

However, the ultimate values found in this manner are still within the range of load capacities estimated in the more complete single tower model. Hence, as this model has not been used for ultimate load estimation, a larger tolerance can be adopted and it can be considered acceptable.

6.2. Cascade hypothesis: effect of tower dynamic collapse

A falling tower can bring to the ground its neighboring towers along with it.

The loading that passes through the cables is dissipated through the whole line, thus, it is important to look at the forces at the insulator connector points (arm tips of the tower) during the fall.

An example, tower n23 falling is analyzed. The earth wire connector was omitted as it was broken, perhaps during the event.

Shortly after the tower starts to fall (0), the towers n22 and n24 are subjected to an immediate load release in the transverse and vertical direction (around 1s in the timeline), as the two neighboring cable segments are released.

The fall of the tower is slowed by the cable inertia, proof of which is in the positive transverse and vertical force on tower n23 (I). The release of the horizontal balancing cable load is evident in the towers n22 and n24, pulled in the opposite longitudinal directions by the other standing spans (to towers n21 and n25 respectively).

| I. Long. load release in neighboring towers | II. Tower n23 touches the ground | III. Cable *"whip effect"*. |
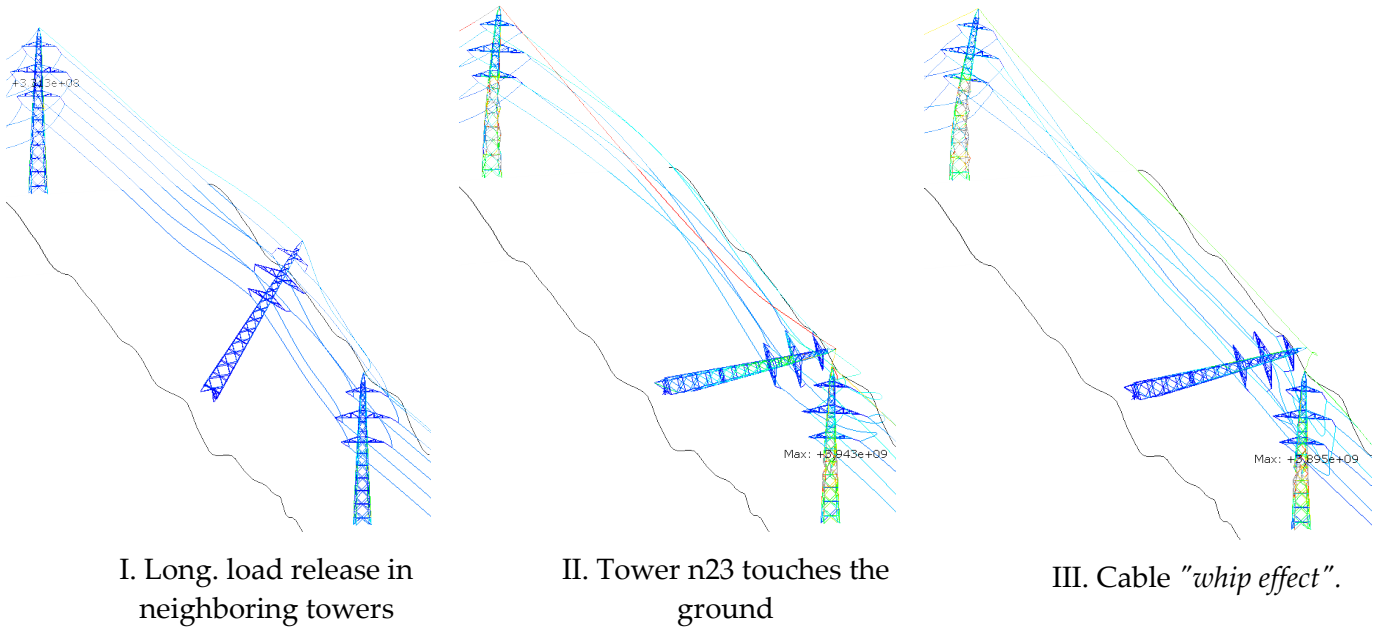
Figure 6.4: Collapse of tower n23.
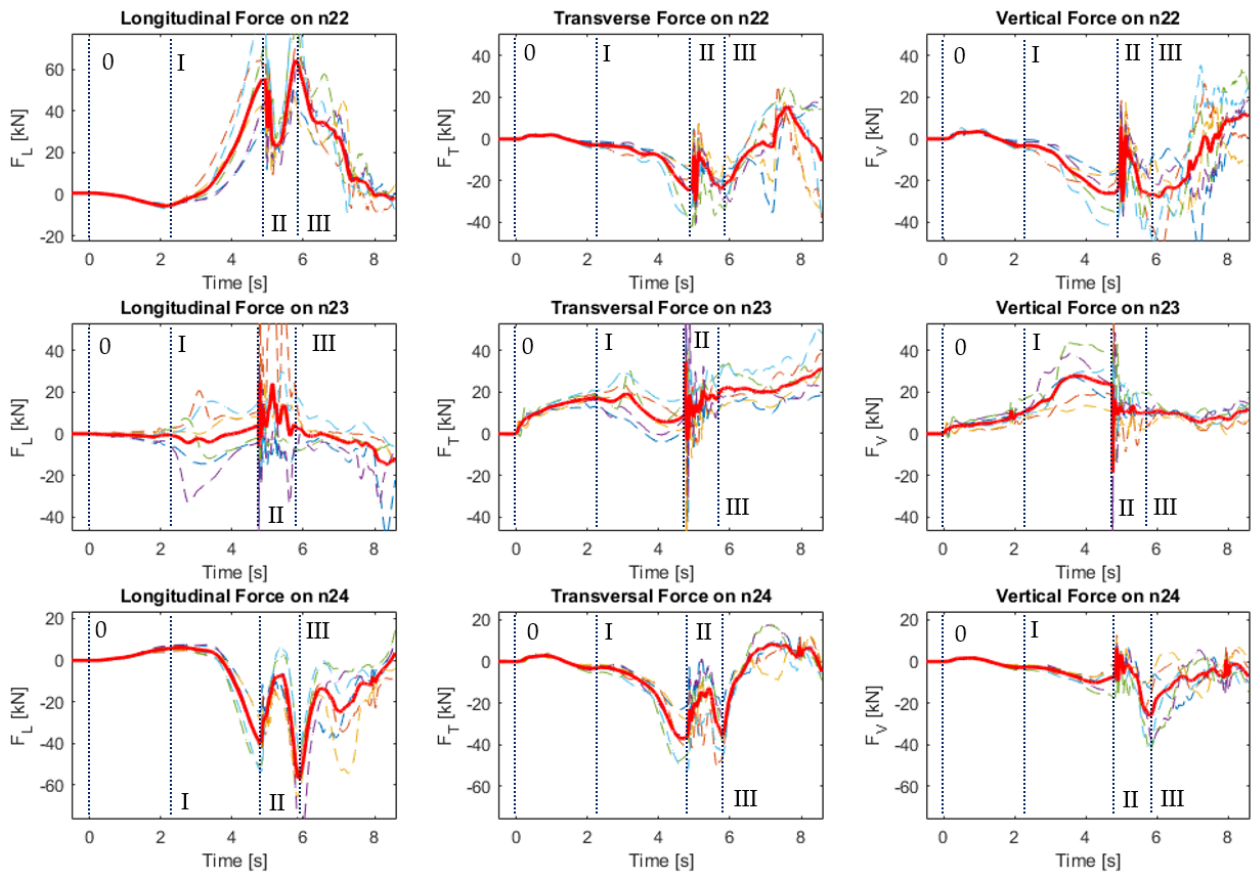
Figure 6.5: Tower n23 collapsing, insulator forces on towers n22, n23 and n24 normalized with the reference component before the collapse. Dashed, the single insulator force, in red the mean between the tower's insulators.

The tower n23 starts to pull the neighboring towers and, as tower n23 touches the ground (II), the load is released, only to come back with a sort of "whip" effect of the interaction between cables and the ground (III). A similar waveform can be seen in the studies of F. Alminhana et al. [15]: the force initially drops as soon as the cable connector is broken, just to raise to maximum moments after.

There is a delay of around 0.15 to 0.3 s (depending on which tower or which cable is considered) from what happens to tower n23, to the moment the effect is "felt" by the other two.

This behavior is similar in the collapse of every of the other towers, especially the one in tower n23 and n24 collapse (Figure 6.6).
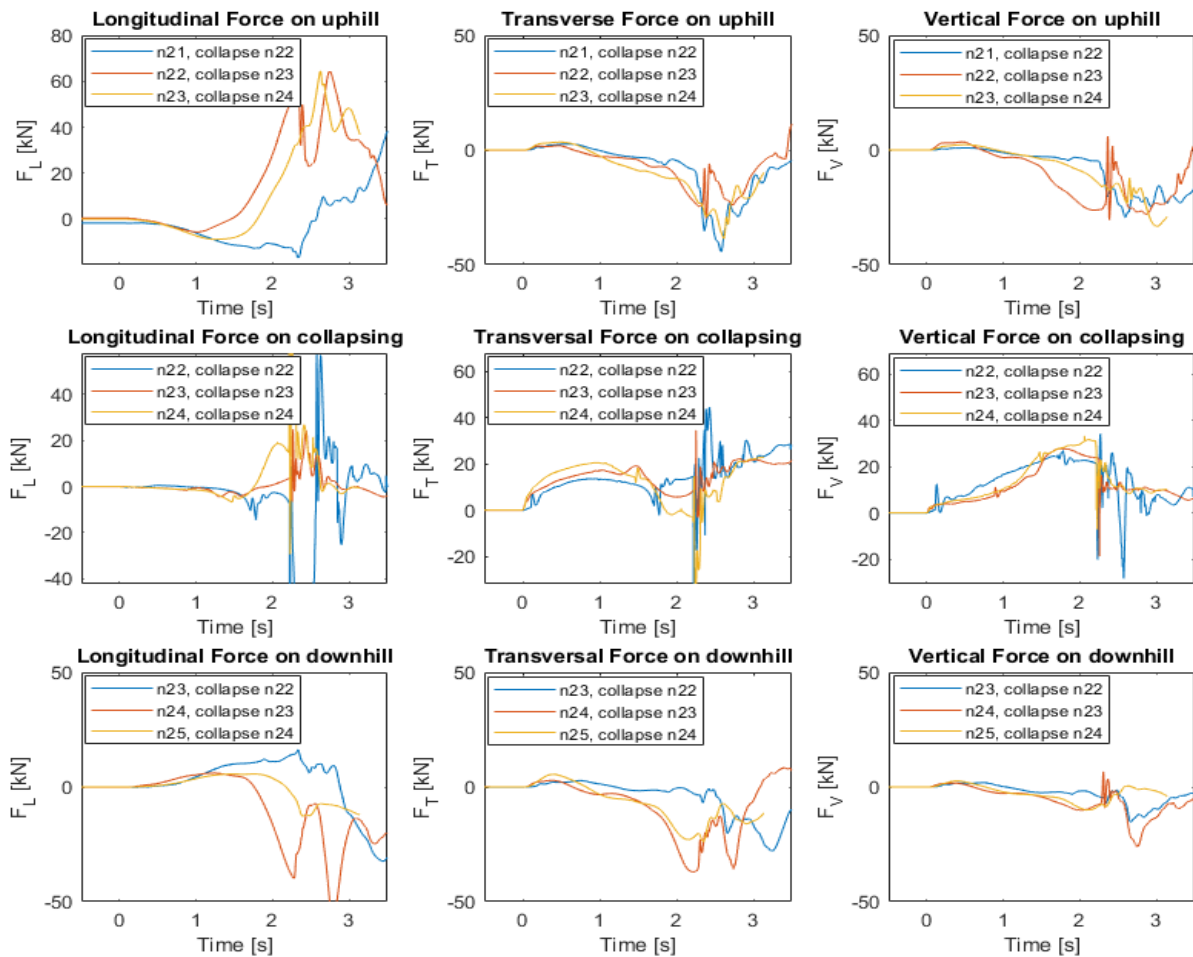
Figure 6.6: Comparison of towers n22, n23 and n24 collapsing, insulator mean forces normalized with the reference component before collapse, and time normalized at the instant tower n22 touches the ground.

The mismatch in the collapse time and response delay in the neighboring towers can both be attributed to the different shape and length of the cable spans. The

marked difference in the collapse of tower n22, might lay in the fact that it collapses
at midheight and it is located the most elevated in the line segment.

Collapsing tower n.	Time to contact with terrain [s]	Neighboring tower n.	$\Delta F_{Longitudinal.}$ [kN]	$\Delta F_{Transverse}$ [kN]	$\Delta F_{Vertical}$ [kN]
Tower n22	2.21	*Uphill: Tower n21*	-101.4	211.8	176.4
		Downhill: Tower n23	88.2	118.2	42.6
Tower n23	2.75	*Uphill: Tower n22*	333.6	146.8	157.1
		Downhill: Tower n24	-233.9	220.2	60.4
Tower n24	2.46	*Uphill: Tower n23*	367.1	165.0	105.5
		Downhill: Tower n25	-76.2	132.0	57.2

Table 6.3: Additional loads due to neighboring tower collapsing (sum of the six
components), reference to the design load in Table 5.5 (*SIA 261/1*).

The load increase with respect to the reference is enough to make the neighboring
towers fall, no matter the failure mode or which tower collapses first.

The tower most likely to cause a cascade effect is tower n23, as it is causes a large
overload on its neighbors. If tower n22 were the first to collapse, it would have
introduced a large loading on tower n21 as well, possibly causing its collapse as
well.

6.2.1. Check on the connector cables and the insulators

As none of them has failed during the event, they have been modeled without
failure criteria. However, some damage to the cables and insulator was visible, but
it had been associated with the fall (secondary damage).

The limits are posed in the form of limit tension on the elements. According to *LeV
1994*, the maximum capacity of the cable has to be set at 2/3 of the ultimate strength:

Property	Insulator	AAAC-600mm^2 (transmission)	Steel-95mm^2 (earthwire)
Ultimate tension [kN]	107.1	177.1	123.5
Maximum allowed LeV 1994 [kN]	-	118.1	82.3

Table 6.4: List of limits for the single cable.

During the collapse of tower n23, the tension at the element was measured on the
two neighboring towers and the results are the following:
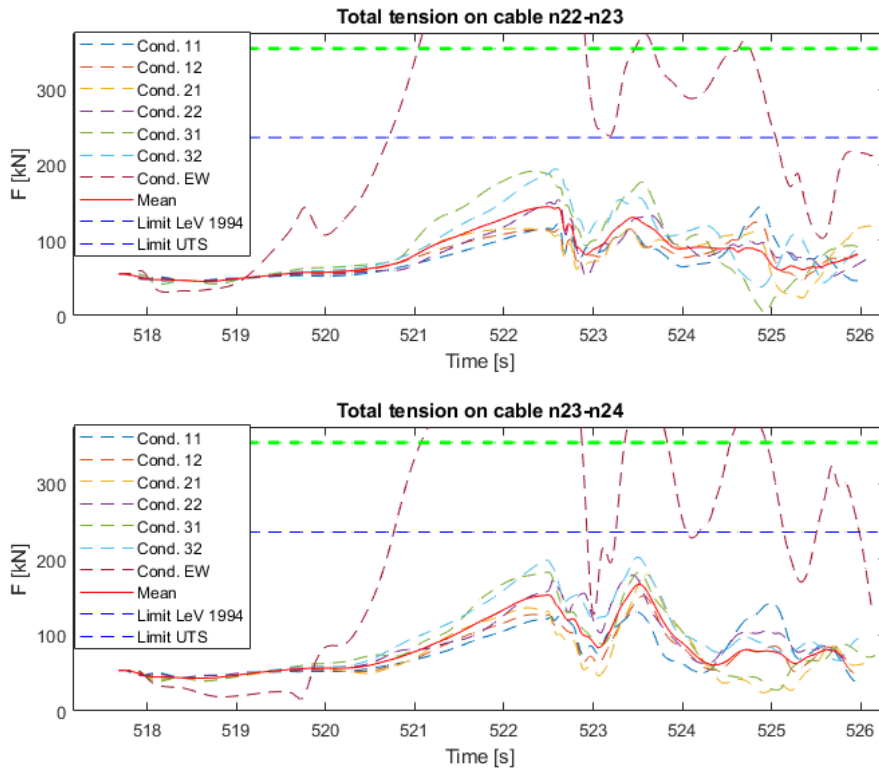
Figure 6.7: Cable spans to tower n22 and to tower n24. The limits are set double
than to the datasheet and *LeV 1994* [42] (Table 6.4), as the wires are coupled.
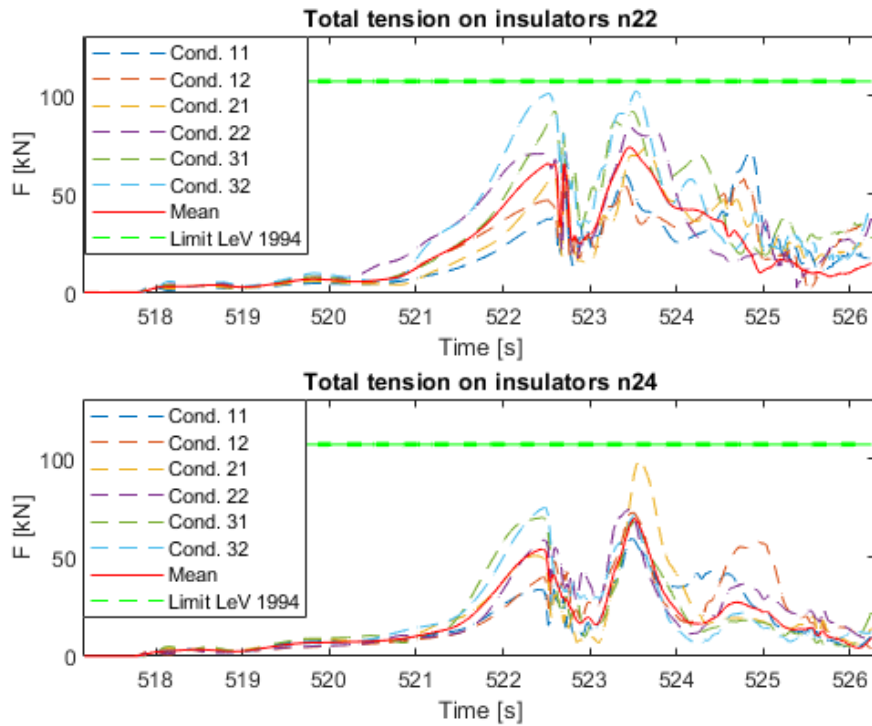
Figure 6.8: Insulators in tower n22 and tower n24. The limits are set according to
the datasheet [41].

The earth wires are under extreme tension, and they are sure to break. The early detachment from tower n23 tip might have prevented it from happening.

Cables and insulators in all positions are under tension that approaches the limit (the mean peaks between 61% and 72% of the limit), especially the ones at the top of the towers (31 and 32). The threshold, however, is set for the coupled wires, hence, it is plausible that some damage to the single one occurred during the event.

Figure 6.9: Damaged cable in tower n22, positions 12 (back) and n22 (front), which were close to limit load (Figure 6.7).

Figure 6.10: Broken insulator, tower n22, position 32, the closest to the limit (Figure 6.8).

6.2.2. Full cascade simulation

As previously discussed, one of the towers most likely to have caused the cascade effect is n23, thus a collapse simulation of the whole line with connector failure criteria, was performed.

All the towers were loaded up to 80% of their reference load *(SIA 261/1)*, and only the structural wind load of tower n23 was increased until its collapse in a subsequent step.

The collapse of tower n23 (0) creates an oscillatory wave that travels through the line (period of around 1.2s), in the transverse direction (not galloping), which was visible in the towers furthest from the event (n21, n25 and n26).

Towers n22 and n24 fail at the closest leg to n23 (I and II), in wind direction, before the peak in longitudinal force is reached. The towers' legs not facing the wind will

fail in sequence due to buckling, as they are the closest to their ultimate capacity in that specific mode (the mechanism is explained in Figure 6.13).

Tower n25 fails shortly after (III).

Note that when n23 touches the ground (IV), the disturbance travels through the cables, reaching all the other towers while still falling.

| I. Tower n23 collapse. | II. Tower n22 and n24 collapse. | III. Tower n25 collapse |
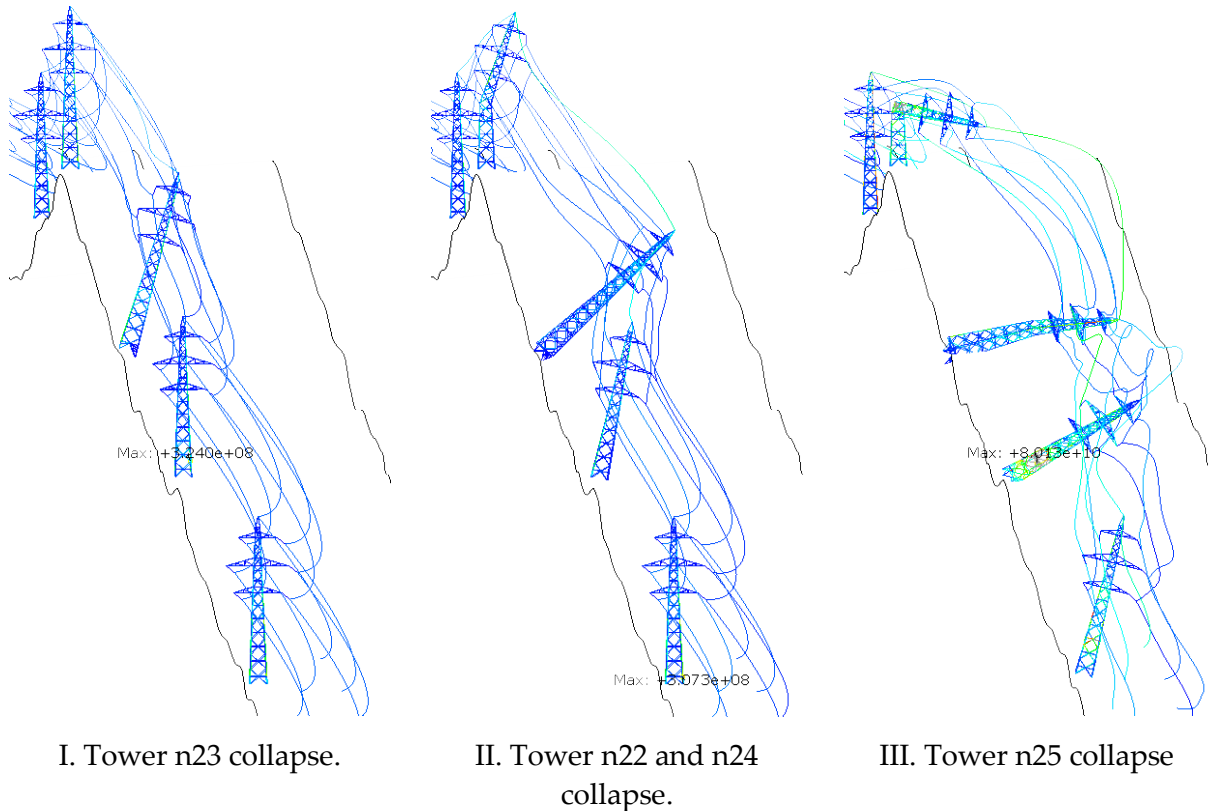
Figure 6.11: Key steps in cascade initiated from tower n23.
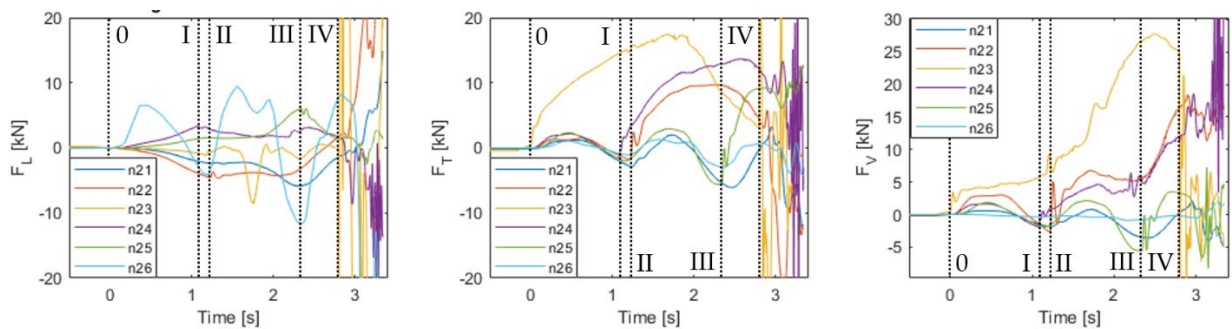
Figure 6.12: Insulator mean forces during the cascade starting from tower n23, normalized with the reference component before collapse.
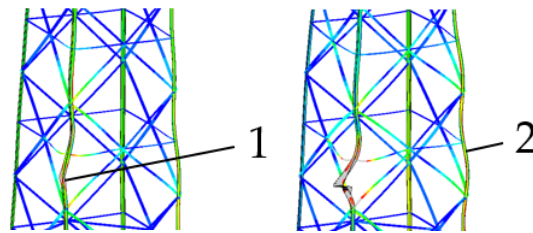
Figure 6.13: Collapse mode in the towers: the leg facing the collapse neighbor fails first (1), followed by the other in the perpendicular direction (2).

The overall collapse event lasts only a few seconds (around 4.2s, when tower n25 hits the ground). There might be some variations depending on the initial load assumptions, ultimate capacity or failure of the cables.

Tower n21 undergoes much lower loading in transverse or vertical direction compared to the others, which might be the reason why it remained intact during the collapse.

The comparison out of the dynamic simulation has been compared to the pictures taken on-site in Figure 6.14, 6.15 and 6.16: although the large model simplifications (structure made of few connected *beam* subassemblies, incapable of yielding), thus constraining the possible deformations the towers can undergo, a fair similarity with the real case is shown. Examples are in Figure 6.14, in which the model does not allow the extensive damage to the neighboring area to the two failed levels (6th and 7th), as the ones below were rigidly intact; or in Figure 6.20, in which the section twisting due to the contact to the ground is not shown.
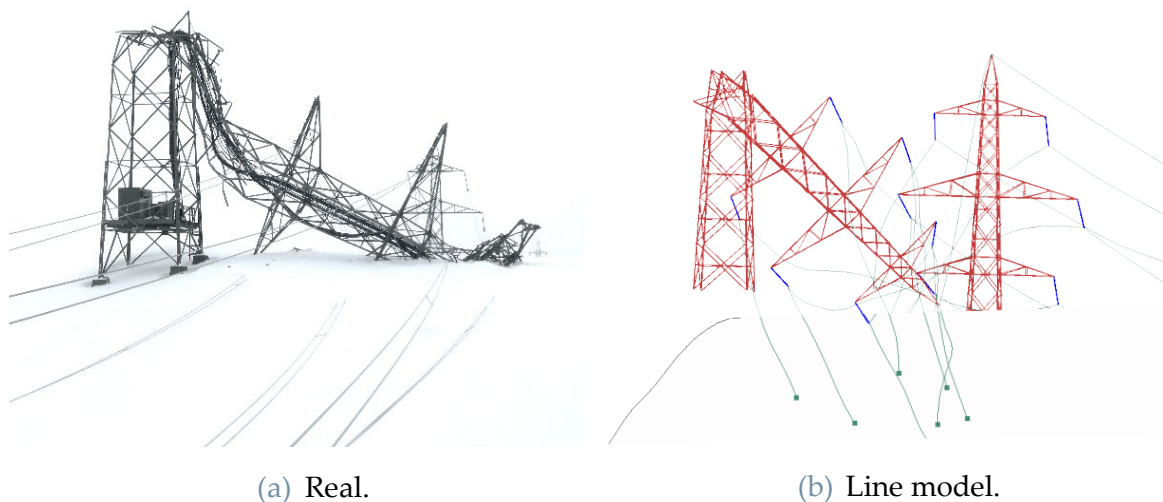
(a) Real.
(b) Line model.

Figure 6.14: On-site pictures after the collapse (source *Swissgrid)*, compared to line *FE* model results, tower n22.
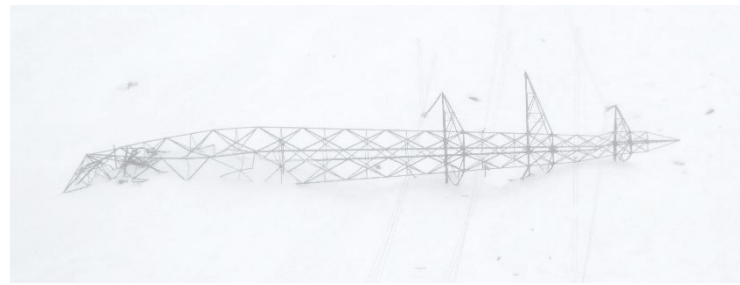
(a) Real.
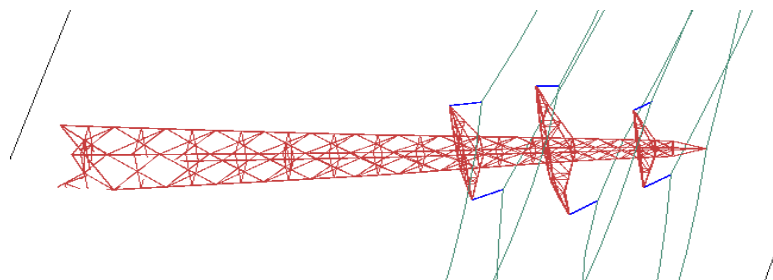
(b) Line model.

Figure 6.15: On-site pictures after the collapse (source *Swissgrid*), compared to line FE model results, tower n23.

(a) Real.
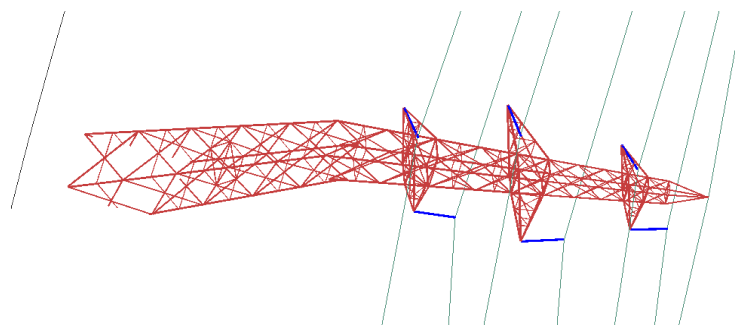
(b) Line model.

Figure 6.16: On-site pictures after the collapse (source *Swissgrid*), compared to line *FE* model results, tower n24.

6.3. Sequence hypothesis: post-collapse analysis

In this case, the collapse is not simultaneous and the towers fall at a separate time during the event, after the fall dynamics has finished and upon the next wind magnitude increase (like a gust). A missing tower in the line might in fact cause unbalance to its neighbors, which can reduce the load-bearing capacity under wind load.

The cable loading when the towers n22, n23 and n24 were quasi-statically brought on the ground have been analyzed in order to measure the load unbalance in a non-simultaneous event, with and without wind.

As the cable load is huge on the tower/s uphill to the first collapsed (much larger than both towers and cables ultimate loads), only the following three cases are considered:

(a) Collapse of the sole tower n22.

(b) Collapse of tower n22 propagated to n23, or n23 to n22.

(c) Collapse of tower n22, n23 or n24, propagated to others.
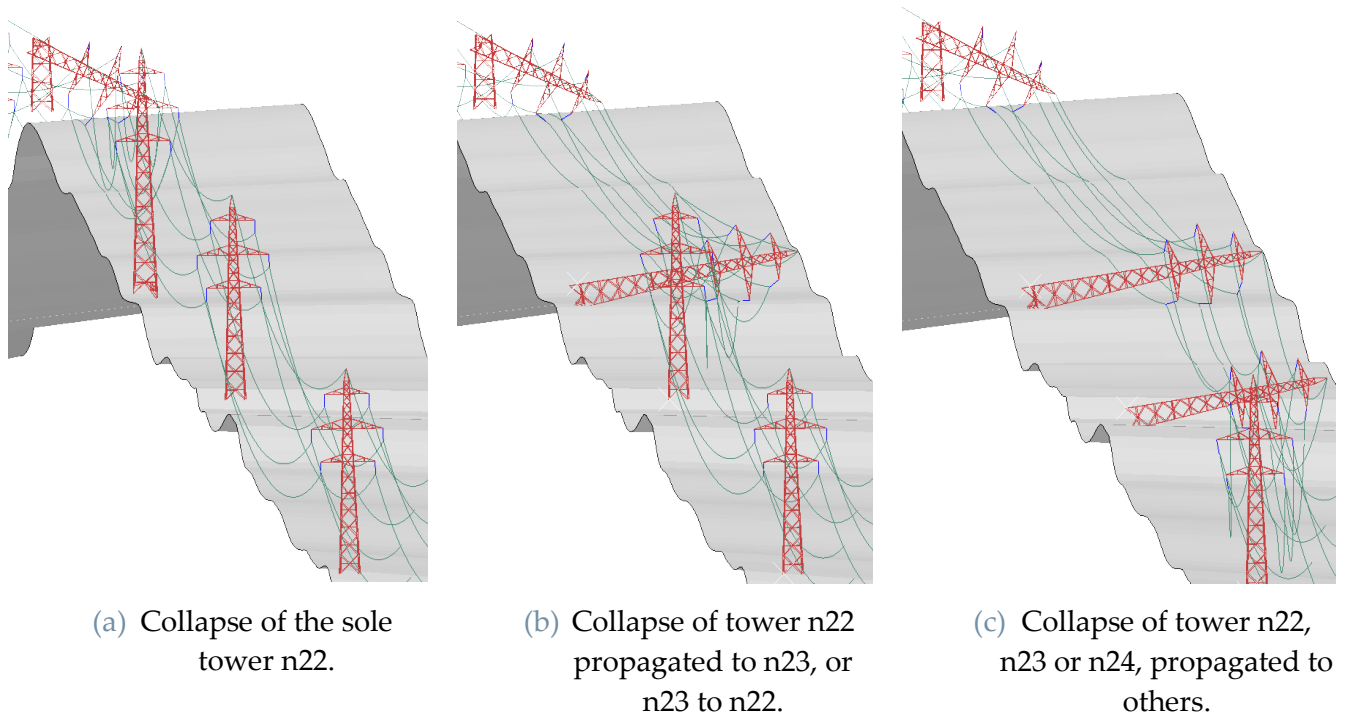
Figure 6.17: Line section (n22 to n25) with some previously failed towers.

The resulting load unbalances are then measured at the insulators of the downhill-most tower that has not yet collapsed (Table 6.5).

Tower n22 experiences in general a lower load with respect to the other towers, both from static and dynamic point of view.

Tower n.	Load case	Longitudinal total load [kN]	Transversal total load [kN]	ΔTransv. [%]	Vertical total load [kN]	ΔVert. [%]
Tower n21	Only gravity	31.9	13.2	-	-80.8	+44%
	With wind	52.1	135.9	+20%	-92.5	+64%
Tower n23	Only gravity	28.5	9.2	-	-108.0	+35%
	With wind	37.5	151.5	+25%	-128.6	+61%
Tower n24	Only gravity	173.6	62.4	-	-123.9	+55%
	With wind	183.2	244.9	+112%	-146.0	+83%
Tower n25	Only gravity	13.5	17.6	-	-100.9	+26%
	With wind	6.8	79.2	-37%	-106.7	+33%

Table 6.5: Additional load due to uphill tower/s on the ground: n21 and n23 unbalance when n22 is on the ground (Figure 6.17a), n24 due to n22 and n23 on the ground (Figure 6.17b), n25 with n22, n23 and n24 on the ground (Figure 6.17c).

In general, the missing towers increase the vertical load that the neighbors have to carry, up to 83%, as well as in longitudinal direction (previously perfectly balanced).

Tower n25 is the least affected by the missing sustain of the other towers, probably being close to the tensioning pylon, and due to the terrain profile, as all the cables are laying on the ground (Figure 6.17c). Towers n24 and n23 are subjected to a high rise in transversal and in longitudinal load. The two would most certainly fail in lower wind conditions than the analyzed so far.

6.4.   Conclusive discussion on the results

The cascade and sequence hypotheses have been investigated and the load unbalances on the neighboring towers have been analyzed.

A cascade effect has proven to be feasible in the analyzed conditions, but it was not possible to identify the source. Collapse simulations similar to Section 6.2, starting from other towers, have been performed, all resulting in a complete failure of the four towers (Figure 6.18). All the line collapse modes remain plausible and lead to a similar outcome.

Moreover, as discussed at the end of the previous Chapter 5, the towers all have similar margins with respect to the reference wind load case, thus none of them can be pointed with certainty as the least resistance of the lot. The large spread in ultimate capacity depending on the applied geometric imperfection modes hints that the failure might have occurred due to an unfavorable wind magnitude on the weakest tower.

(d) Collapse starting from tower n22.

(e) Collapse starting from n24.

(f) Collapse starting from n25.
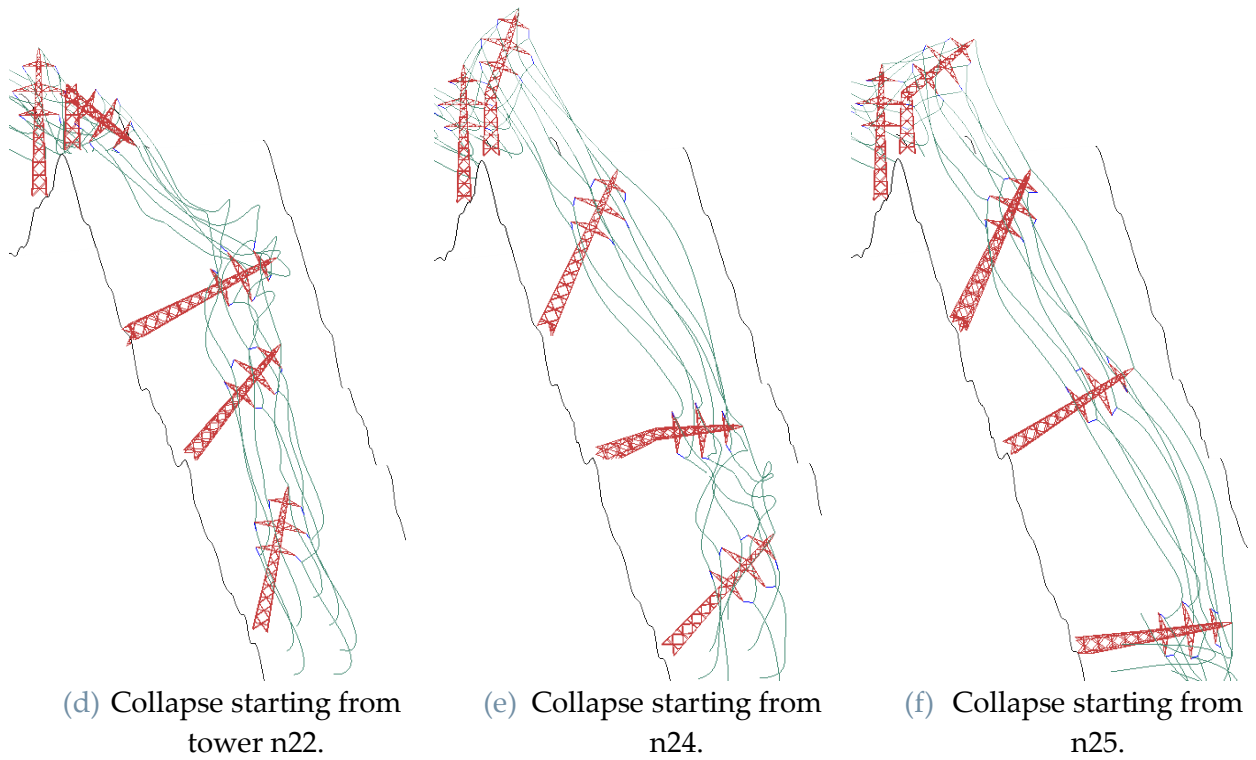
Figure 6.18: Collapse dynamics if the cascade had started from other towers.

7   Chapter seven: Brief discussion about dynamic analysis

The analysis performed in Chapter 5 and 6 have analyzed only the quasi-static effect of the wind loading. Load amplification as a consequence of resonance instability, or fatigue under the dynamic wind components, can potentially reduce structural margin with respect to the static design value.

Many studies in the field of wind-induced collapse analysis, remark the importance of a wind response analysis, both in time and frequency domain and different aspects of transmission lines response to wind excitations are treated by several authors. The main points of view are going to be discussed in Section 7.1.

The applicability to the current study and possible limitations are discussed in Section 7.2.

7.1.   State-of-the-art on dynamic analysis

7.1.1.   Fluid-Structure interaction analysis

H. Keyhan et al. [51] performed a *Fluid-Structure Interaction (FSI)* analysis on transmission line conductor system, in order to obtain a correct loading on the conductors during their transversal vibration under turbulent wind.

The conductors, being the part of the line that undergoes the largest displacement (thus the largest aeroelastic interaction with the wind), participated in a two-dimensional *FSI* analysis: at each dynamic simulation time step, a two-dimensional *Computational Fluid Dynamic (CFD)* analysis is performed, and the integral surface pressure on the cable section is used as an external load in the following step. The section is maintained in place by a lateral stiffness model, based on the *3D* cable. The load is then introduced in the *3D* model in different span positions.

The results show up to 26% lower loading with respect to the coefficient-based method used by design standards such as *IEC 60826*, which transfers to up to 37% lower tension in the conductors for the analyzed models.

7.1.2. Nonlinear response

Q. Li et al. [52] used an *Ansys FE* model to analyze the nonlinear response of a power transmission line system to turbulent wind time-history. The wind load was applied according to the Chinese standards and then dynamically varied according to Kaimal power spectral density.

It was possible to assess that the displacement due to line vibration was greater (up to almost five times larger) if more towers of the line were considered.

7.1.3. Dynamic wind modeling

A. Dua et al. [53] compared the dynamic response of a transmission line to turbulent wind, to the static load given by *Eurocode EN50341* [45], via nonlinear dynamic *FEA* in *SAP2000*, accounting for large displacements (geometrical nonlinearity).

The average wind profile and forces were taken as in *EN50341*, neglecting the dynamic part. They produced a turbulent wind time history via *Weighted Amplitude Wave Superposition* (*WAWS*) based on Von-Karman spectral density for the wind in the longitudinal direction, Kaimal in the transverse direction, Bush-Panofsky in the vertical direction. The effective force applied to elements larger than the turbulent eddies (such as the conductor cables) can be up to 45% higher.

They proved that the static loads from the codes were underestimating the peak response by a factor of 12% in terms of cable tension and around 31% in terms of peak displacement. The difference between a model of the sole cables and one in which cables and towers are considered is 4.6% in peak tension and 15% in displacement.

7.1.4. Material model

L. Tian et al. [54] performed *FEA* in *Abaqus 6.10* on a 60m-tall steel lattice communication tower collapse under stochastic wind load. They employed Tian-Ma-Qu material model to simulate the post-yield material behavior and the Bauschinger effect (material nonlinearities).

The bucking in the main legs due to structure vibrations was the reason for the failure in most of the simulations.

7.2. Applicability and limitations

In *Abaqus CAE 2021*, free excitation modes can be estimated from a *"Linear perturbation, Frequency"* procedure, which works similarly to an *LBA*, by finding the

stiffness matrix instability modes in frequency domain. A best practice is to analyze the cable and the tower systems both separately and combined, to assess possible overlapping resonance frequencies.

However, the study would need some sort of validation (that might be provided by studies like X. Liu et al. [39], which propose an analytical solution to cable vibration) but the accuracy would be limited, as the *"Linear perturbation, Frequency"* is based on linear elastic material properties and small displacement hypothesis. Moreover, to address properly the response to wind excitation, the model has to be excited in the right magnitude and frequency, and to contain geometrical and material nonlinearities.

A complete nonlinear forced-response analysis can be performed in time domain, by transforming the wind dynamic spectrum into a function of time and varying a constant static load (as in [52, 53]). However, the limitations are mainly due to the lack of more precise data to perform an accurate analysis of this type:

- Unknown wind characteristic: wind speed and direction, as well as its spatial distribution across the line-span, are not available. As in [53], they can be estimated from well-known models, but a *CFD* analysis on the mountainous profile could potentially locate the real wind distribution, as well as localized wind gusts that can cause excitation on specific components of the line. However, it might prove too computationally expensive and the wind pressure boundary conditions, as well as the simulation scale, might not be accurate enough to give a reliable outcome.
- A realistic response to wind loading would include a study of the aero elasticity (coupled vibrations of the structure and of the wind). A full *Fluid-Structure Interaction (FSI)* procedure as in [51] could be performed, but it has also to account for effects such as wake / vortex shedding - structure interaction. However, it might prove again too computationally expensive and the starting wind conditions should be correctly estimated.
- A more complex material model need to be used, with would require more experimental parameters in order to perform an accurate analysis ([54]). As discussed in [54], the main failure mode in slender structure might still be buckling governed (caused by peak load or by peak response), thus the importance of fatigue analysis is limited.

8   Chapter eight: Conclusions

The study proposes modeling methods for lattice towers under wind loading and affected by structural instability, with the final purpose of being applied to a failure analysis. Some modeling strategies are discussed in Chapter 1 to 4 and the failure analysis case is treated in Chapter 5 and 6. In Chapter 7, possible further analysis methods and limitations are proposed.

8.1.   Main points

The final objective of the analysis was to employ and review new modeling techniques in failure analysis and compare the results with the work of other consultancies.

To address the point, different modeling techniques are proposed, in the form of element types adoption, joint modeling and different analysis procedures usage. The analysis proved to be inconclusive in terms of finding the origin of the collapse, but the critical structural elements have been correctly identified.

The dynamics of the event has been simulated starting from different assumptions and the results hint that a cascade effect is highly probable, no matter what tower fails first.

More specifically, the key questions that the study posed are answered as follows.

   1.   *Which is the best way to perform FEA for structural instabilities?*

The main difficulties in modeling for structural instabilities are:

- *Boundary conditions:* the correct simulation of boundary conditions is key to accurate modeling. The buckling mode and ultimate load highly depend on the element end-restrains by definition.

- *Imperfections:* different modes can influence buckling direction and ultimate load. The mode magnitude and direction are critical parameters and might be a source of discrepancies with experimental data.

There is no generalized *"optimal"* approach to the problem: a tradeoff between model accuracy and complexity (proportional to computational cost) has to be

achieved. In single braces or low complexity assemblies, the best result is achieved with *3D* elements (Chapter 4), able to better simulate the complete joint friction interaction or the section yielding. When analyzing a larger structure, *Beam* or *Shell* elements should be used. Connector elements can limit the downsides.

2. *How would joint flexibility influence the FEA?*

In structures in which member buckling is a predominant failure mode, joint flexibility affects both the single *beam* and lattice structure ultimate load capacity. Joint slippage can influence the displacement at ultimate load and might as well reduce the load-bearing capacity.

The pinned joint connection, often employed in the design phase, is not a correct representation and leads to underestimation of member capacity, and to incorrect failure mode prediction.

The modeling with elements fixed to each other can be a more realistic representation in some cases, but it is based on the assumption of infinite moment transmission through the joints.

The modeling via stiffness functions or coefficients can be a good solution, but it requires a large number of parameters based on several *3D* sub-models simulations.

3. *Which modeling approaches are applicable to the modeling of large lattice structures with a multitude of joints?*

A completely *3D* model is usually not a possibility for such a large lattice structure, as it required the accurate positioning of such a large number of parts and bolts and can be computationally expensive. Even with only *Shell* elements, the extrusion process is inefficient and a large amount of elements is anyway created.

1D elements are much quicker to set up and can represent a structure with lower computational effort. However, they cannot properly display *torsional-flexural buckling* modes.

Hybrid *Shell+Beam* models can be a nice improvement, but they are not suited for the design phase, where an ultimate load underestimation is preferred. Nevertheless, they could be used for *Failure Mode, Effects, and Criticality Analysis (FMECA)*, in which the correct reproduction of failure causes and effects is required.

Models that integrate joint flexibility can be a good tradeoff between complexity and accuracy in physical behavior. However, it requires consistent effort for *3D* joint

sub-model creation, stiffness function modeling, connector built up and validation, thus losing convenience if these steps have to be carried out for a large amount of times. Partially building the lattice structure with connector models (for example focusing on the most critical area only), or using *pinned* joints for single-bolt connections, might be a good tradeoff for very complex structures.

> 4. *What is the load-bearing capacity of the high-voltage transmission towers in AlbulaPass and their sensitivity to imperfections? How is it far from the static design load?*

The towers n22 and n23 were analyzed. Their margin to collapse with respect to the same reference load model *SIA 261/1* was around 30% in both structures (Table 5.16), thus a collapse due to the wind only can be assumed plausible. As the considered load cases were taken from a conservative assumption (in the failure analysis sense), the structure would most certainly not be able to withstand larger loads, such as the ones considered in the *Eurocodes*.

However, it is not possible to point out the tower closest to failure, as the high sensitivity on the applied imperfections makes the ultimate load capacity range from 104% to 137% the design value (Table 5.12): any difference in margin smaller than this range could not be an undebatable proof. Relatively tiny imperfections could be overlooked in an investigation on-site, or misinterpreted as secondary damage.

The estimated load-bearing capacities from *RIKS* analysis were around 30% higher than *LBA* for both tower n22 and n23 (Figure 5.64). This indicates that the structure is able to overcome loads higher than the linear elastic instability limit, probably due to member plastic reserve.

The results from *LBA* and *RIKS* analyses are close to the utilization factors calculated by *IED* for the same load case (Figure 5.64). Their results, however, were calculated using a design-standard-based *"member utilization factor"*, thus the failure position was located more towards the base of the towers, in contrast to the state the structures were found after the event. Moreover, as it was demonstrated in Chapter 1 and 2, design standards do not always match the member capacity nor the stability limit, as the stress state in lattice structure members is extremely end-restrains dependent.

5. *How can a cascade sequence occur in the power transmission line and, possibly, where it is more likely to have started?*

The dynamic simulations in Chapter 6 proved that a cascade effect has proven to be plausible, but it was not possible to identify the source.

Moreover, all the towers (except for maybe n25) are greatly compromised in terms of load-bearing capacity if the ones uphill are on the ground (sequence effect).

The fact that the loading on tower n21 was minimum when tower n22 was not the first to collapse may exclude at least one tower. The 1986 event, in which tower n22 was not involved at all, might hint that the others were at larger risk.

8.2.   Outlook and future research

The main limitations of the study are given by the lack of comprehensive data and by time restrictions.

Weather data or wind measurements are required to improve the load assumptions, but good estimates are difficult to achieve (Chapter 7).

The model accuracy could not be further assessed: validation procedures for the sub-structures (Chapter 4) and transmission line (Chapter 5 and 6) were not available, as testing on large lattice structures is expensive and not economically viable for this failure analysis.

A larger time span could allow to investigate further in the failure analysis case:

- Other wind directions and could have been investigated;

- A dynamic wind loading could have been investigated (however, with the limitations discussed in Chapter 7), with a possibility of *"Dynamic, Explicit"* collapse simulation of the single tower with measured cable loads in order to reproduce the progressive failure of the elements;

- How much the load unbalances resulting from a collapse sequence (Section 6.3) can actually hinder the towers load capacity;

- Further investigation on the 1986 event, trying to understand why tower n22 had resisted the cascade.

Bibliogaphy

[1]   R. J. Campbell and S. Lowry, "Weather-related power outages and electric system resiliency," 2012: Congressional Research Service, Library of Congress Washington, DC.

[2]   P. Hoffman and W. Bryan, "Comparing the impacts of Northeast hurricanes on energy infrastructure. US Department of Energy, Washington DC, USA," ed, 2013.

[3]   S.-j. Fang, S. Roy, and J. Kramer, "Transmission structures," *Structural engineering handbook,* 1999.

[4]   *EN 1993-3-1 (2006) (English): Eurocode 3: Design of steel structures - Part 3-1: Towers, masts and chimneys – Towers and masts.*

[5]   *ABAQUS 2021 Analysis User's Manual*. Simulia, Providence, RI (USA). 2021.

[6]   "Report on the damaging event Albula 2018," AF-Consult Switzerland AG, 4500_en-SPJ-20190326-1, 2019.

[7]   "Material tests on samples from the failed masts No. 22-25 (tensile tests and notched impact bending tests)," Empa, 5214,020,451, 2019.

[8]   "Mobile investigations on steel masts," IWT, 17013689, 21.12.2016 2016.

[9]   "Screw testing of lines Filisur - La Punt," IWT, 17013888, 20.01.2017 2017.

[10]   "On the computational investigations on masts 22-25 of the Filisur-La Punt line, Collapse of 380kV towers, Albula Pass, Expert's report - Conditions and sequence of failure for masts no. 22-23-24-25.," IED Groupe SA, 2019.

[11]   C. Affolter, "Damage analysis for the claim "Albula 2018", 4 steel masts of the 380 kV line La Punt – Filisur," EMPA, 5214,021,838, 12.7.2019 2019.

[12]   U. f. d. a. UFAM. "Carta dei terreni di fondazione secondo la norma SIA 261." https://opendata.swiss/it/dataset/karte-der-seismischen-baugrundklassen-nach-der-baunorm-sia-261 (accessed 23/03/22.

[13]   *SIA 261/1:2003, Actions on Structures – Supplementary Specifications, Herausgeber Schweizerischer Ingenieur- und Architektenverein Postfach, CH-8039 Zürich.*

[14]   F. Albermani, S. Kitipornchai, and R. W. K. Chan, "Failure analysis of transmission towers," *Engineering Failure Analysis,* vol. 16, no. 6, pp. 1922-1928, 2009, doi: 10.1016/j.engfailanal.2008.10.001.

[15]   F. Alminhana, M. Mason, and F. Albermani, "A compact nonlinear dynamic analysis technique for transmission line cascades," *Eng. Struct.,* vol. 158, pp. 164-174, 2018, doi: 10.1016/j.engstruct.2017.12.039.

[16]   W. Wang, H. Li, and L. Tian, "Progressive collapse analysis of transmission tower-line system under earthquake," *Advanced Steel Construction,* vol. 9, no. 2, pp. 161-172, 2013.

[17]   Y. Mohammadi Darestani, A. Shafieezadeh, and K. Cha, "Effect of modelling complexities on extreme wind hazard performance of steel lattice transmission towers," *Structure and Infrastructure Engineering,* vol. 16, no. 6, pp. 898-915, 2019, doi: 10.1080/15732479.2019.1673783.

[18]   J. Wang, H.-N. Li, X. Fu, and Q. Li, "Geometric imperfections and ultimate capacity analysis of a steel lattice transmission tower," *J. Constr. Steel Res.,* vol. 183, 2021, doi: 10.1016/j.jcsr.2021.106734.

[19]   C. Affolter, G. Piskoty, L. Wullschleger, and B. Weisse, "Collapse of a high storage rack," *Engineering Failure Analysis,* vol. 16, no. 6, pp. 1846-1855, 2009, doi: 10.1016/j.engfailanal.2008.09.011.

[20]   N. Prasad Rao, G. M. S. Knight, N. Lakshmanan, and N. R. Iyer, "Investigation of transmission line tower failures," *Engineering Failure Analysis,* vol. 17, no. 5, pp. 1127-1141, 2010, doi: 10.1016/j.engfailanal.2010.01.008.

[21]   N. Prasad Rao, G. M. Samuel Knight, S. Seetharaman, N. Lakshmanan, and N. R. Iyer, "Failure Analysis of Transmission Line Towers," *Journal of Performance of Constructed Facilities,* vol. 25, no. 3, pp. 231-240, 2011, doi: 10.1061/(asce)cf.1943-5509.0000161.

[22]   N. Prasad Rao, G. M. Samuel Knight, S. J. Mohan, and N. Lakshmanan, "Studies on failure of transmission line towers in testing," *Eng. Struct.,* vol. 35, pp. 55-70, 2012, doi: 10.1016/j.engstruct.2011.10.017.

[23]   M. R. Eslami, J. Eslami, and M. Jacobs, *Buckling and postbuckling of beams, plates, and shells*. Springer, 2018.

[24]   S. P. Timoshenko and J. M. Gere, *Theory of Elastic Stability. 2.ed*. McGraw-Hill, 1961.

[25]   E. R. J. J. Ferdinand P. Beer, I. The McGraw-Hill Companies, 1221 Avenue of the Americas, New York, NY, Ed. *MECHANICS OF MATERIALS*, Sixth ed. ed. 2012.

[26]   N. S. Trahair, *Flexural-Torsional Buckling of Structures*. UK by E & FN Spon, an imprint of Chapman & Hall, 2-6 Boundary Row, London SEl 8HN, 1993.

[27]   W.-W. Yu, R. A. LaBoube, and H. Chen, *Cold-formed steel design*. John Wiley & Sons, 2019.

[28]   P. B. Dinis and D. Camotim, "A novel DSM-based approach for the rational design of fixed-ended and pin-ended short-to-intermediate thin-walled angle columns," *Thin-Walled Struct*, vol. 87, pp. 158-182, 2015, doi: 10.1016/j.tws.2014.10.013.

[29]   *EN 1993-1-1 (2005) (English): Eurocode 3: Design of steel structures - Part 1-1: General rules and rules for buildings.*

[30]   M. Kettler, G. Lichtl, and H. Unterweger, "Experimental tests on bolted steel angles in compression with varying end supports," *J. Constr. Steel Res.*, vol. 155, pp. 301-315, 2019, doi: 10.1016/j.jcsr.2018.12.030.

[31]   P. Uriz, F. C. Filippou, and S. A. Mahin, "Model for cyclic inelastic buckling of steel braces," *Journal of structural engineering*, vol. 134, no. 4, pp. 619-628, 2008.

[32]   M. Kettler, A. Taras, and H. Unterweger, "Member capacity of bolted steel angles in compression – Influence of realistic end supports," *J. Constr. Steel Res.*, vol. 130, pp. 22-35, 2017, doi: 10.1016/j.jcsr.2016.11.021.

[33]   *EN 1993-1-8 (2005) (English): Eurocode 3: Design of steel structures - Part 1-8: Design of joints.*

[34]   W. Q. Jiang, Z. Q. Wang, G. McClure, G. L. Wang, and J. D. Geng, "Accurate modeling of joint effects in lattice transmission towers," *Eng. Struct.*, vol. 33, no. 5, pp. 1817-1827, 2011, doi: 10.1016/j.engstruct.2011.02.022.

[35]   N. Ungkurppinan, "A STUDY OF JOINT SLIP IN GALVANIZED BOLTED ANGLE CONNECTIONS," Faculty of Graduate Studies of the University of Manitoba, 2000.

[36]   M. Kettler, H. Unterweger, and P. Zauchner, "Design model for bolted angle members in compression including joint stiffness," (in English), *J. Constr. Steel Res.*, Article vol. 184, 2021, Art no. 106778, doi: 10.1016/j.jcsr.2021.106778.

[37]   R. Ramalingam and S. Arul Jayachandran, "Computational framework for mimicking prototype failure testing of transmission line towers," *Eng. Struct.*, vol. 123, pp. 181-191, 2016, doi: 10.1016/j.engstruct.2016.05.021.

[38]   M. Fong, S.-H. Cho, and S.-L. Chan, "Design of angle trusses by codes and second-order analysis with experimental verification," *J. Constr. Steel Res.*, vol. 65, no. 12, pp. 2140-2147, 2009, doi: 10.1016/j.jcsr.2009.07.001.

[39]   X. Liu, Y. Hu, and M. Cai, "Free vibration analysis of transmission lines based on the dynamic stiffness method," *R Soc Open Sci,* vol. 6, no. 3, p. 181354, Mar 2019, doi: 10.1098/rsos.181354.

[40]   R. Anshika. "Mechanical Design of Transmission Lines | Electrical Engineering."engineeringenotes.com. https://www.engineeringenotes.com/electrical-engineering/transmission-lines/mechanical-design-of-transmission-lines-electrical-engineering/29019 (accessed 24/03/22).

[41]   M. R. V. Bollotte, "New 380kV pylons installed at Albula Pass, Expert's report – Mechanical analysis of the new pylons n°22-23-24-25 " IED Groupe SA, 02613.80.012, 13.08.2019.

[42]   *RS 734.31 - Verordnung über elektrische Leitungen (1994), Schweizerischen Bundesrat.*

[43]   MATLAB, *version 9.9 (R2020b).* The MathWorks Inc., Natick, Massachusetts, 2020.

[44]   *EN 1991-1-4 (2005) (English): Eurocode 1: Actions on structures - Part 1-4: General actions - Wind actions.*

[45]   *EN 50341-1, Overhead electrical lines exceeding AC 1 kV Part 1: General requirements Common specifications, Cenelec, 2012, ICS 29.240.20.*

[46]   S. Prud'homme, F. Legeron, A. Laneville, and M. K. Tran, "Wind forces on single and shielded angle members in lattice structures," *Journal of Wind Engineering and Industrial Aerodynamics,* vol. 124, pp. 20-28, 2014, doi: 10.1016/j.jweia.2013.10.003.

[47]   J. C. Stroman, "AERODYNAMIC DRAG COEFFICIENTS OF A VARIETY OF ELECTRICAL CONDUCTORS," Graduate Faculty of Texas Tech University, 1997.

[48]   G. Piskoty, L. Wullschleger, R. Loser, A. Herwig, M. Tuchschmid, and G. Terrasi, "Failure analysis of a collapsed flat gymnasium roof," *Engineering Failure Analysis,* vol. 35, pp. 104-113, 2013, doi: 10.1016/j.engfailanal.2012.12.006.

[49]   S. D. Eslamlou and B. Asgarian, "Determining critical areas of transmission towers due to sudden removal of members," *Case Studies in Engineering Failure Analysis,* vol. 9, pp. 138-147, 2017/10/01/ 2017, doi: https://doi.org/10.1016/j.csefa.2015.09.005.

[50]   M. Jian, G. Zhang, D. Zhang, G. Liu, and Z. Fan, "Analysis of Uneven Settlement and Restoration Measures for One 220kV Transmission Tower,"

in *2015 2nd International Forum on Electrical Engineering and Automation (IFEEA 2015)*, 2016: Atlantis Press, pp. 249-252.

[51]   H. Keyhan, G. McClure, and W. G. Habashi, "Dynamic analysis of an overhead transmission line subject to gusty wind loading predicted by wind–conductor interaction," *Computers & Structures*, vol. 122, pp. 135-144, 2013, doi: 10.1016/j.compstruc.2012.12.022.

[52]   Q. Li, Y. Junjian, and L. Wei, "Random Wind-induced Response Analysis of Transmission Tower-line System," *Energy Procedia*, vol. 16, pp. 1813-1821, 2012, doi: 10.1016/j.egypro.2012.01.279.

[53]   A. Dua, M. Clobes, and T. Höbbel, "Dynamic analysis of overhead transmission line under turbulent wind loading," (in English), *Electron. J. Struct. Eng.*, Article vol. 15, no. 1, pp. 46-54, 2015.

[54]   L. Tian, X. Zhang, and X. Fu, "Collapse Simulations of Communication Tower Subjected to Wind Loads Using Dynamic Explicit Method," *Journal of Performance of Constructed Facilities*, vol. 34, no. 3, 2020, doi: 10.1061/(asce)cf.1943-5509.0001434.

List of Figures

List if Tables

List of symbols

Variable	Description	SI unit
v	vertical displacement	mm
δ	lateral deflection	mm
F	force	N
F_{cr}	critical buckling force	N
$F_{cr,eul}$	*Euler buckling* critical force	N
λ	slenderness ratio	-
L	member length	Mm
E	Young's elastic modulus	GPa
A	section area	mm²
I	section moment of inertia	mm⁴
K	boundary condition dependent variable	-
$C1, C2, C3$	deformed shape equation constants	mm
c	distance to section neutral axis	mm
M	bending moment	Nm
M_0	bending moment at member-end	Nm
R	lateral force at member-end	N
$x\text{-}x, y\text{-}y$	axis in X, Y direction	-
$u\text{-}u$	primary/strongest axis	-
$v\text{-}v$	secondary/weakest axis	-
λ_n	normalized slenderness ratio	-
λ_{eff}	effective normalized slenderness ratio	-
$X, X1, \Phi$	*Eurocode 1993-1.1* buckling parameters	-
α_λ	imperfection factor, *Eurocode 1993-1.1*	-
$[K]$	system stiffness matrix	N/m
$\bar{u}$	displacement vector	m
Δt	time-increment length	s
$l_{element}$	element size	m
s	speed of sound	m/s
ρ	material density	Kg/m³
S_y	material yield strength	MPa
υ	Poisson's ratio	-

e, e_{imp}, e_0	imperfection magnitude	mm
R_m, UTS	ultimate strength	MPa
A_s	nominal bolt area	mm^2
γ_{M7}	bolt pre-tensioning factor, *Eurocode 1993-1.8*	-
$N_{Pretensioning}$	bolt pre-tensioning force	N
f	static friction coefficient	-
K_0	bending stiffness at member ends	kNm/rad
A_p	projected section area	`m^2
z	height from the ground	m
q_b	base wind pressure	Pa
α	shielding factor	-
q_p	dynamic pressure	Pa
c_h	wind profile coefficient, *SIA 261/1*	-
α_r	roughness coefficient, *SIA 261/1*	-
z_0	roughness height, *SIA 261/1*	m
c_{red}	slenderness factor, *SIA 261/1*	-
c_{f1}	global force coefficient, *SIA 261/1*	-
$c_{f,cond}$	wire global force coefficient, *SIA 261/1*	-
v_b	base wind velocity, *Eurocode 1991-1.4*	m/s
v_{b0}	10-min mean wind velocity, *Eurocode 1991-1.4*	m/s
$c_{direction}$	direction coefficient, *Eurocode 1991-1.4*	-
c_{season}	season coefficient, *Eurocode 1991-1.4*	-
$c_{probability}$	probability coefficient, *Eurocode 1991-1.4*	-
v_m	mean wind velocity, *Eurocode 1991-1.4*	m/s
c_r	roughness coefficient, *Eurocode 1991-1.4*	-
k_r, k_0	roughness formula coefficients, *Eurocode 1991-1.4*	-
c_0	orography coefficient, *Eurocode 1991-1.4*	-
σ_v	wind velocity std deviation, *Eurocode 1991-1.4*	-
I_v	turbulence intensity factor, *Eurocode 1991-1.4*	-
c_e	wind profile coefficient, *Eurocode 1991-1.4*	-
$c_s \cdot c_d$	structural factor, *Eurocode 1991-1.4*	-
c_f	force coefficient, *Eurocode 1991-1.4*	-
c_{f0}	force coefficient without end-flow, *Eurocode 1991-1.4*	-
φ_λ	end-flow factor, *Eurocode 1991-1.4*	-
Re	Reynold's number, *Eurocode 1991-1.4*	-
ν	kinematic viscosity, *Eurocode 1991-1.4*	m^2/s
φ	section solidity, *Eurocode 1991-1.4*	-
λ_{str}	structure section slenderness, *Eurocode 1991-1.4*	-

λ_{cond}	wire section slenderness, *Eurocode 1991-1.4*	-
$K_{\theta}, K_{\theta+90}, K_1, K_2$	wind incidence factors, *Eurocode 1993-3.1*	-
c_{f1}, c_{f2}	force coefficients, *Eurocode 1993-3.1*	-
ϑ	wind incidence angle, *Eurocode 1993-3.1*	rad
η_1, η_2	shielding factors, *Eurocode 1993-3.1*	-
Q_{wc}	wind force on wires, *EN50341*	N
c_c	wire drag factor, *EN50341*	-
G_c	wire structural factor, *EN50341*	-
C_D	L-section drag coefficient	-
F_D	L-section drag force	N
C_L	L-section lift coefficient	-
F_L	L-section lift force	N
A_{nom}	L-section nominal area	mm^2
T_H	horizontal wire tension component	N
T_V	vertical wire tension component	N
α_m	imperfection parameter, *Eurocode 1993-3.1*	-
m	number of members in the bracing system	-

Acknowledgments

Throughout the entirety of my university career, I received great support and assistance from my friends and family. I rarely tell them how much I love them and respect them.

Great appreciation for the professors and colleagues at Politecnico di Torino, Politecnico di Milano, and Technische Universität Hamburg, as well as my supervisors at Empa – Swiss Federal Laboratories: they helped me to focalize my efforts, to always raise the bar of what I am capable of doing.

I am extremely grateful to who had faith in me, and to who had not, inspiring me to grow and become a better person in spite of the difficulties and limitations encountered in my journey.

The path ahead is full of opportunities!

Giacomo Vettoretto

Zürich, Switzerland, April 2022